

# **Characterization and model identification for the simulation of the forming behavior of ferritic steels**

Der Fakultät Maschinenbau  
der Technischen Universität Dortmund  
zur Erlangung des Grades eines  
Doktor-Ingenieurs  
(Dr.-Ing.)  
genehmigte Dissertation

von

**Muhammad Noman**

Dortmund 2011



# Contents

|   |             |
|---|-------------|
| <b>Summary</b>  | <b>xiii</b> |
| <b>1 Introduction</b>   | <b>1</b>    |
| <b>2 Experimental characterization and modeling of the hardening behavior of the sheet steel LH800</b>                                    | <b>5</b>    |
| 2.1 Introduction . . . . .  | 5           |
| 2.2 Model formulation . . . . .   | 8           |
| 2.3 Material testing . . . . .  | 10          |
| 2.4 Model identification . . . . .  | 16          |
| 2.5 Yield surface evolution . . . . .   | 20          |
| 2.6 Inelastic state evolution . . . . .   | 25          |
| 2.7 Summary and conclusions . . . . .   | 28          |
| <b>3 Simplification and identification of a model for directional hardening</b>   | <b>31</b>   |
| 3.1 Introduction . . . . .  | 31          |
| 3.2 Model formulation . . . . .   | 32          |
| 3.3 Material testing . . . . .  | 35          |
| 3.4 Identification of material models . . . . .   | 38          |
| 3.5 Evolution of internal state variables . . . . .   | 43          |
| 3.6 Summary and conclusions . . . . .   | 45          |
| <b>4 Comparison of the hardening behavior of the sheet steel LH800 for tests with strain path changes and its influence on springback</b> | <b>47</b>   |
| 4.1 Introduction . . . . .  | 47          |
| 4.2 Material Model . . . . .  | 49          |
| 4.3 Material testing . . . . .  | 51          |
| 4.4 Model identification . . . . .  | 59          |
| 4.5 Comparison of responses of tests with the responses of simulations . . . . .  | 67          |
| 4.6 Application to springback prediction (during draw-bending test) . . . . .   | 69          |
| 4.7 Summary and Conclusions . . . . .   | 72          |
| <b>5 Numerical and physical factors affecting the springback simulation for sheet metal forming</b>                                       | <b>75</b>   |

|          |   |            |
|----------|---|------------|
| 5.1      | Introduction . . . . .  | 75         |
| 5.2      | Material Model . . . . .  | 76         |
| 5.3      | Draw-Bending Test . . . . .   | 78         |
| 5.4      | Element formulations . . . . .  | 80         |
| 5.5      | Contact and friction modeling . . . . .                                     | 81         |
| 5.6      | Convergence behavior and numerical integration . . . . .                    | 85         |
| 5.7      | Structural and process conditions . . . . .                                 | 90         |
| 5.8      | Conclusions . . . . .   | 94         |
| <b>A</b> | <b>Experimental characterization and model identification of steel DC06</b> | <b>97</b>  |
| A.1      | Material Testing . . . . .  | 97         |
| A.2      | Parameter Identification . . . . .  | 98         |
|          | <b>References</b>   | <b>105</b> |
|          | <b>Acknowledgements</b>   | <b>111</b> |
|          | <b>Curriculum Vitae</b>   | <b>113</b> |

# List of Figures

|      |  |    |
|------|--|----|
| 2.1  | Biaxial test setup. Geometry of the tension-shear specimen and the measurement region of height $b$ and width $c$ . The checkered region indicates the actual specimen and the black area marks the actual deformation zone. The tension direction is direction 2 and the shear direction is direction 1. . . . .                  | 11 |
| 2.2  | Scanning electron micrograph showing microstructure of LH800 (Experiment IW Hannover). . . . .   | 12 |
| 2.3  | Tension test results for LH800 at strain rates of $10^{-1} \text{ s}^{-1}$ (upper curve), $10^{-2} \text{ s}^{-1}$ (middle curve), $10^{-3} \text{ s}^{-1}$ (lowest curve). $K_{22}$ represents the relevant component of the Kirchhoff stress and $F_{22}$ represents the relevant component of the deformation gradient. . . . . | 13 |
| 2.4  | Reverse shear test results for LH800 for two different levels (i.e., 0.1 and 0.65) of pre-shear. All stress results are shown in absolute value form. . . . .  | 13 |
| 2.5  | Experimental strain paths in LH800 resulting from continuous change of loading direction from tension to shear. . . . .  | 14 |
| 2.6  | Stress response of LH800 for monotonic forward simple shear (curve starting at $F_{22} + F_{12} = 1$ ) and for the 5 different orthogonal tension-shear paths shown in Figure 2.5. . . . .   | 14 |
| 2.7  | Discontinuous and continuous orthogonal loading-path changes from tension to shear in LH800. Normal stress component $K_{22}$ (symbols) and shear stress component $K_{12}$ (lines) as a function of $F_{22} + F_{12}[-]$ . The vertical dashed line indicates deformation states of equal $F_{22} + F_{12}$ . . . . .             | 15 |
| 2.8  | Experimental paths in $(K_{22}, K_{12})$ stress space corresponding to selected paths shown in Figure 2.5 and 2.7. Points A, B and C mark the state of deformation corresponding to the intersection of the vertical dashed line in Figure 2.7 with the respective stress curves. . . . .  | 15 |
| 2.9  | Comparison of the experimental monotonic simple-shear data with the corresponding identified model prediction. $K_{12}$ represents the relevant shear component of the Kirchhoff stress. . . . .   | 17 |
| 2.10 | Comparison of the experimental cyclic simple-shear data with the corresponding identified combined isotropic-kinematic model prediction. . . . .   | 18 |
| 2.11 | Comparison of the predictions of the identified standard combined (i.e., isotropic-kinematic) hardening model for forward simple shear and orthogonal tension-shear with corresponding experimental results from path 1 in Figure 2.5. . . . .   | 18 |

|      |  |    |
|------|--|----|
| 2.12 | Comparison of identified isotropic-kinematic-cross hardening model behavior with experimental data for monotonic simple-shear and orthogonal tension-shear test data corresponding to strain path 1 in Figure 2.5. . . . .   | 19 |
| 2.13 | Comparison of the experimental results for strain paths 5 and 4 in Figure 2.5 with corresponding simulation results as based on the identified model for isotropic-kinematic-cross hardening. Right: path 4. Left: path 5. . . . .   | 20 |
| 2.14 | Comparison of the experimental results for strain paths 3 and 2 in Figure 2.5 with corresponding simulation results as based on the identified model for isotropic-kinematic-cross hardening. Right: path 2. Left: path 3. . . . .   | 20 |
| 2.15 | Yield surface evolution for LH800 during uniaxial tension (top) and simple shear (bottom). Shown here are the initial surface (Ini), an intermediate tension state (Ten1), the final tension state at $F_{22} = 1.2$ (Ten2), the final forward shear state at $F_{12} = 0.4$ (She1), and the final reverse shear state at $F_{12} = 0.0$ (She2). . . . .   | 21 |
| 2.16 | Predicted yield surface evolution for LH800 during orthogonal loading from plane-strain tension to simple-shear depicted in normalized stress space ( $\bar{K}_{12}$ , $\bar{K}_{22}$ ) for the discontinuous transition. Ini represents the initial yield surface. TenFin is the final tensile state. TenShe1 to TenShe3 represent subsequent yield surfaces during subsequent loading for the loading path also shown in Figure 2.5 and 2.7. The point C indicates the stress state obtained during the experiment and is the same point C as shown in Figure 2.8. . . . . | 22 |
| 2.17 | Predicted yield surface evolution for LH800 during orthogonal loading from plane-strain tension to simple-shear depicted in normalized stress space ( $\bar{K}_{12}$ , $\bar{K}_{22}$ ) for the continuous path 5. Ini represents the initial yield surface. TenFin is the final tensile state. TenShe1 to TenShe3 represent subsequent yield surfaces during subsequent loading for the loading path also shown in Figure 2.5. The point A indicates the stress state obtained during the experiment and is the same point A as shown in Figure 2.8. . . . .                | 22 |
| 2.18 | Yield surfaces development for LH800 during monotonic uniaxial tension (top) and simple shear (bottom) for pure cross hardening. Ini represents the initial yield surface. Ten1 is an intermediate tension stage. Ten2 represents the final tension stage for $F_{22} = 1.2$ . She1 is an intermediate shear stage. She2 indicates the yield surface for $F_{12} = 0.4$ . . . . .  | 23 |
| 2.19 | Yield surfaces after tension (top) and torsion (bottom) obtained by Ishikawa (1997) for SUS304. Ini represents the initial isotropic yield surface, Ten1 is the yield surface translated to the origin after tension, Ten2 is the yield surface after tension, She1 and She2 represent the translated and measured yield surfaces, respectively, after torsion. Cen marks the computed center of the subsequent yield surfaces. $\tau$ and $\sigma$ represent the relevant Cauchy shear and normal stresses, respectively. . . . .   | 24 |
| 2.20 | Evolution of $a_d$ on paths 1, 3 and 5 in Figure 2.5. Note that $ \mathcal{A}_d  =  a_d $ . . . . .  | 26 |
| 2.21 | Development of $ \mathcal{A} $ on paths 1, 3 and 5 in Figure 2.5. . . . .  | 26 |

|      |  |    |
|------|--|----|
| 2.22 | Evolution of $ \mathbf{X} $ along paths 1, 3 and 5 in Figure 2.5. . . . .  | 27 |
| 2.23 | Development of $X_{22}$ along paths 1, 3 and 5 in Figure 2.5. . . . .  | 27 |
| 2.24 | Evolution of $X_{12}$ along paths 1, 3 and 5 in Figure 2.5. . . . .  | 28 |
| 3.1  | Biaxial test setup. Geometry of the tension-shear specimen and the measurement region of height 3.0mm and width 45.0 mm. The checkered region indicates the actual specimen and the black area marks the actual deformation zone. The tension direction is direction 2 and the shear direction is direction 1. . . . . | 36 |
| 3.2  | Reverse shear test results for LH800 for two different levels (i.e., 0.1 and 0.65) of pre-shear. All stress results are shown in absolute value form. . . . .  | 37 |
| 3.3  | Experimental strain paths in LH800 resulting from continuous change of loading direction from tension to shear. . . . .  | 37 |
| 3.4  | Stress response of LH800 for monotonic forward simple shear (curve starting at $F_{22} + F_{12} = 1$ ) and for the 5 different orthogonal tension-shear paths shown in Figure 3.3. . . . .   | 38 |
| 3.5  | Comparison of the experimental cyclic simple-shear data with the corresponding identified full yield stress model prediction. . . . .  | 40 |
| 3.6  | Comparison of the experimental tension-shear data for strain path 1 in Figure 3.3 with the corresponding identified full yield stress model prediction. . . . .  | 40 |
| 3.7  | Comparison of the experimental results for strain paths 5 and 4 in Figure 3.3 with corresponding simulation results as based on the identified full yield stress model for isotropic-kinematic-cross hardening. Right: path 4. Left: path 5. . . . .   | 41 |
| 3.8  | Comparison of the experimental results for strain paths 3 and 2 in Figure 3.3 with corresponding simulation results as based on the identified full yield stress model for isotropic-kinematic-cross hardening. Right: path 2. Left: path 3. . . . .   | 41 |
| 3.9  | Comparison of the experimental cyclic simple-shear data with the corresponding identified (simplified) yield stress model prediction. . . . .  | 42 |
| 3.10 | Comparison of the experimental tension-shear data for strain path 1 in Figure 3.3 with the corresponding identified (simplified) yield stress model prediction. . . . .  | 43 |
| 3.11 | Comparison of the experimental results for strain paths 5 and 4 in Figure 3.3 with corresponding simulation results as based on the identified (simplified) yield stress model for isotropic-kinematic-cross hardening. Right: path 4. Left: path 5. . . . .   | 43 |
| 3.12 | Comparison of the experimental results for strain paths 3 and 2 in Figure 3.3 with corresponding simulation results as based on the identified (simplified) yield stress model for isotropic-kinematic-cross hardening. Right: path 2. Left: path 3. . . . .   | 44 |
| 3.13 | Evolution of internal state variable $s_x$ and shear stress $K_{12}$ for reverse shear shear experiment predicted by yield stress model. $\alpha_P$ represents accumulated plastic strain. . . . .   | 44 |

|      |  |    |
|------|--|----|
| 3.14 | Evolution of internal state variable $s_x$ and shear stress $K_{12}$ for reverse shear shear experiment predicted by simplified yield stress model. $\alpha_P$ represents accumulated plastic strain. . . . .  | 45 |
| 3.15 | Evolution of internal state variables for tension-shear experiment path1 in Figure 3.3 predicted by yield stress model. . . . .  | 46 |
| 3.16 | Evolution of internal state variables for tension-shear experiment path1 in Figure 3.3 predicted by simplified yield stress model. . . . .   | 46 |
| 4.1  | Scanning electron micro graph showing microstructure of LH800 in the as received condition (Experiment IW Hannover). . . . .   | 52 |
| 4.2  | Biaxial test setup. Geometry of the tension-shear specimen and the measurement region of height 3.0mm and width 45.0 mm. The checkered region indicates the actual specimen and the black area marks the actual deformation zone. The tension direction is direction 2 and the shear direction is direction 1. . . . . | 53 |
| 4.3  | Reverse shear test results for LH800 for two different levels of pre-shear. All stress results are shown in absolute value form. $K_{12}$ represents the relevant component of the Kirchhoff stress and $F_{12}$ represents the relevant component of the deformation gradient. . . . .                                | 54 |
| 4.4  | Experimental strain paths in LH800 resulting from continuous change of loading direction from tension to shear. . . . .  | 54 |
| 4.5  | Stress response of LH800 for monotonic forward simple shear (curve starting at $F_{22} + F_{12} = 1$ ) and for the 5 different orthogonal tension-shear paths shown in Figure 4.4. . . . .   | 55 |
| 4.6  | Tensile test results conducted at $0^\circ$ , $45^\circ$ and $90^\circ$ with respect to the rolling direction. $K_{22}$ represents relevant components of Kirchhoff stress and $\ln U_{11}$ represents relevant component of logarithmic strain . . . . .  | 56 |
| 4.7  | Tension-compression test result for LH800. . . . .   | 56 |
| 4.8  | Pure bending device with air suspended clamps (Boers et al. (2010)) . . . . .  | 57 |
| 4.9  | Schematic representation of pure bending experiment. (Boers et al. (2010)) . . . . .   | 58 |
| 4.10 | Pure bending test results. Left: Pure bending test results for 3 cycles of bending . Right: Bauschinger and Orthogonal test Results of prestrained sample. . . . .   | 59 |
| 4.11 | Comparison of the experimental monotonic simple-shear data with the corresponding identified model prediction. $K_{12}$ represents the relevant shear component of the Kirchhoff stress and $F_{12}$ represents the relevant component of the deformation gradient. . . . .  | 60 |
| 4.12 | Comparison of the experimental reverse simple-shear data with the corresponding identified model prediction. . . . .   | 61 |
| 4.13 | Comparison of the predictions of the identified standard combined (i.e., isotropic-kinematic) hardening model for forward simple shear and orthogonal tension-shear with corresponding experimental results from path 1 in Figure 4.4. . . . .   | 61 |



|      |   |    |
|------|---|----|
| 4.14 | Comparison of identified isotropic-kinematic-cross hardening model behavior with experimental data for monotonic simple-shear and orthogonal tension-shear test data corresponding to strain path 1 in Figure 4.4. . . . .  | 62 |
| 4.15 | Comparison of the experimental uniaxial tension data with the corresponding identified model prediction. . . . .  | 64 |
| 4.16 | Comparison of the experimental uniaxial tension compression data with the corresponding identified model prediction. . . . .  | 64 |
| 4.17 | Result of mesh convergence analysis for thickness direction. Left: for one cycle of bending test. Right: bending moment at the end of first cycle. . . . .  | 65 |
| 4.18 | Comparison of the experimental bending test data with the isotropic hardening model prediction. . . . .   | 65 |
| 4.19 | Comparison of the experimental bending test data with the isotropic-kinematic hardening model prediction. . . . .   | 66 |
| 4.20 | Comparison of the predictions of the identified standard combined (i.e., isotropic-kinematic) hardening model. Left: for reverse bending test. Right: for orthogonal bending test. . . . .  | 67 |
| 4.21 | Comparison of the experimental and simulation stress-strain response. The experiment is uniaxial tension-compression and simulations are performed using the parameters identified from the reverse shear test and the pure bending test respectively. . . . .                                | 68 |
| 4.22 | Comparison of the experimental and simulation stress-strain response. The experiment is the reverse shear test and simulations are performed using the parameters identified from the uniaxial tension-compression test and the pure bending test respectively. . . . .                       | 68 |
| 4.23 | Comparison of the experimental and simulation bending moment versus bending angle response. The experiment is the pure bending test and simulations are performed using the parameters identified from the uniaxial tension-compression test and the reverse shear test respectively. . . . . | 69 |
| 4.24 | Finite element model for draw-bending test . . . . .  | 70 |
| 4.25 | Comparison of experimental and simulation results for roller radius 10 mm. . .  | 71 |
| 4.26 | Comparison of experimental and simulation results for roller radius 15 mm. . .  | 71 |
| 4.27 | Comparison of experimental and simulation results using the combined and the distortional hardening model for roller radius 10 mm. . . . .  | 72 |
| 5.1  | Draw-bending test machine and experimental setup, from Kleiner et al. (2005). . .   | 79 |
| 5.2  | Rigid boundary surface geometry (ABAQUS 6.9.1 Theory Manual 5.1.3). . . .   | 83 |
| 5.3  | ”Softened” pressure-overclosure relationship defined with the exponential relation (ABAQUS 6.9.1 Analysis’s User’s Manual ). . . . .  | 83 |
| 5.4  | 3D FEM model for the draw-bending test and position of Reference Point. . .   | 86 |

|      |  |     |
|------|--|-----|
| 5.5  | Influence of the number of shell elements (S4R) using ABAQUS. Left: On the von Mises stress generated at the end of forming stage. Right: On the springback predicted. . . . .   | 86  |
| 5.6  | Influence of the number of shell elements using LS-DYNA. Left: On the von Mises stress generated at the end of forming stage. Right: On the springback predicted. . . . .  | 87  |
| 5.7  | Influence of the number of through thickness integration points using ABAQUS. Left: On the von Mises stress generated at the end of forming stage. Right: On the springback predicted. . . . .   | 87  |
| 5.8  | Influence of the number of through thickness integration points using LS-DYNA. Left: On the von Mises stress generated at the end of forming stage. Right: On the springback predicted. . . . .  | 88  |
| 5.9  | Influence of the number of through thickness solid elements using ABAQUS. Left: On the von Mises stress generated at the end of forming stage. Right: On the springback predicted. . . . .   | 89  |
| 5.10 | Influence of the number of through thickness solid elements using LS-DYNA. Left: On the von Mises stress generated at the end of forming stage. Right: On the springback predicted. . . . .  | 89  |
| 5.11 | Influence of the element formulation over the predicted springback. Left: Using ABAQUS. Right: Using LS-DYNA. . . . .  | 90  |
| 5.12 | Influence of the back force. Left: On the von Mises stress generated at the end of forming stage. Right: On the springback predicted. . . . .  | 91  |
| 5.13 | Influence of the roller radius. Left: On the von Mises stress generated at the end of forming stage. Right: On the springback predicted. . . . .   | 92  |
| 5.14 | Influence of the friction. Left: On the von Mises stress generated at the end of forming stage. Right: On the springback predicted. . . . .  | 92  |
| 5.15 | Influence of the material model used. . . . .  | 93  |
| 5.16 | Influence of the elastic unloading scheme on the springback prediction results of draw-bending. . . . .  | 94  |
| A.1  | Reverse simple shear tests for the steel DC06 for different levels of preshear. $K_{12}$ represents the relevant component of the Kirchhoff stress and $F_{12}$ represents the relevant component of the deformation gradient. . . . . | 98  |
| A.2  | Experimental strain paths in DC06 resulting from change of loading direction from tension to shear. . . . .  | 98  |
| A.3  | Shear stress response monotonic forward simple shear and for the three different strain-paths of orthogonal tension-shear test shown in Figure A.2. . . . .  | 99  |
| A.4  | Discontinuous and continuous orthogonal loading-path changes from tension to shear in DC06. . . . .  | 99  |
| A.5  | Comparison of the experimental cyclic simple-shear data with the corresponding identified combined isotropic-kinematic model prediction. . . . .   | 100 |

|      |  |     |
|------|--|-----|
| A.6  | Comparison of identified isotropic-kinematic-cross hardening model behavior with experimental data for monotonic simple-shear and orthogonal tension-shear test data corresponding to strain path 1 in Figure A.2. . . . . | 101 |
| A.7  | Comparison of the experimental cyclic simple-shear data with the corresponding identified full yield stress model prediction. . . . .  | 102 |
| A.8  | Comparison of the experimental tension-shear data for strain path 1 in Figure A.2 with the corresponding identified full yield stress model prediction. . . . .  | 103 |
| A.9  | Comparison of the experimental cyclic simple-shear data with the corresponding identified (simplified) yield stress model prediction. . . . .  | 104 |
| A.10 | Comparison of the experimental tension-shear data for strain path 1 in Figure A.2 with the corresponding identified (simplified) yield stress model prediction. . . . .  | 104 |

# List of Tables

|     |  |    |
|-----|--|----|
| 2.1 | Identified hardening model parameter values for LH800. Left: isotropic hardening parameter values determined from monotonic simple-shear test data alone. Right: isotropic-kinematic hardening parameters determined from monotonic and cyclic simple-shear test data alone. . . . .     | 17 |
| 2.2 | Identified hardening model parameter values for LH800 for isotropic-kinematic-cross hardening model parameter values determined from monotonic shear, cyclic shear, and orthogonal tension-shear, test data. . . . .   | 19 |
| 3.1 | Material parameter values for LH 800 using only cyclic shear data. . . . .   | 39 |
| 3.2 | Identified parameters of the full yield stress model for LH 800. . . . .   | 39 |
| 3.3 | Material parameter values for LH 800 using only cyclic shear data. . . . .   | 41 |
| 3.4 | Identified parameters of the simplified yield stress model for LH 800. . . . .   | 42 |
| 4.1 | Chemical composition of steel LH800. All values are given as weight percentage.  | 52 |
| 4.2 | Identified hardening model parameter values for LH800. Left: isotropic hardening parameter values determined from monotonic simple-shear test data alone. Right: isotropic-kinematic hardening parameters determined from monotonic and reverse simple-shear test data. . . . .          | 60 |
| 4.3 | Identified hardening model parameter values for LH800 for isotropic-kinematic-cross hardening model parameter values determined from monotonic shear, cyclic shear, and orthogonal tension-shear, test data. . . . .   | 62 |
| 4.4 | Identified hardening model parameter values for LH800. Left: isotropic hardening parameter values determined from uniaxial tension test data alone. Right: isotropic-kinematic hardening parameters determined from uniaxial tension and uniaxial tension compression test data. . . . . | 63 |
| 4.5 | Identified hardening model parameter values for LH800 determined from pure bending test data. Left: isotropic hardening parameter values determined . Right: isotropic-kinematic hardening parameters. . . . .   | 65 |
| 5.1 | Material model parameter values for LH 800. . . . .  | 85 |
| 5.2 | Identified hardening model parameter values for LH800. Left: isotropic hardening model parameter. Middle: kinematic hardening model parameter. Right: combined isotropic-kinematic hardening model parameters. . . . .   | 93 |

|     |   |     |
|-----|---|-----|
| A.1 | Identified yield surface model parameter values for DC06 for isotropic-kinematic-cross hardening model parameter values determined from monotonic shear, cyclic shear, and orthogonal tension-shear, test data. . . . . | 100 |
| A.2 | Identified parameters of the full yield stress model for DC06. . . . .  | 102 |
| A.3 | Identified parameters of the simplified yield stress model for DC06. . . . .  | 103 |



# Summary

The experimental and theoretical characterization of sheet metal forming continues to present a number of challenges for theorists and experimentalists alike. Among the foremost issues in this regard is a realistic model for the material behavior. The material model should be able to account for the effects of the microstructural development and the development of different types of hardening that evolve due to complex loading path histories involved in sheet metal forming processes. The characterization / identification of the material model needs to be performed for the specific material using the available experiments that produce strain-stress responses for different loading paths. The other issues involved in the characterization of sheet metal forming are the numerical and physical (structural) factors. The current work falls within this context and deals with the formulation of the material model, its characterization and application of this material model to the simulation of sheet metal forming processes. The factors effecting the simulation of metal forming and springback are then discussed.

In complex forming processes, sheet metal undergoes large plastic deformations involving significant induced flow anisotropy resulting from the development of persistent oriented (planar) dislocation structures. The first part of this thesis deals with the formulation and identification of a phenomenological model which accounts for the effect of the evolution of this oriented dislocation microstructure on the anisotropic hardening behavior. The model accounts for changes in the size, center, and shape of the yield surface associated with isotropic, kinematic and cross hardening, respectively. Identification of the model for the ferritic sheet metal steel LH800 is carried out with the help of shear, reverse shear, and tension-shear tests. The identified model has been validated by using it to predict the stress-strain behavior of the material along different tension-shear loading paths and comparison with analogous experimental results. The results and, in particular, the comparison of theoretical predictions with experimental results clearly demonstrate the need of including cross hardening effects in the modeling of sheet metals like LH800.

Metal forming processes generally involve large strains and severe strain path changes. Large plastic strains in many metals lead to the development of persistent dislocation structures resulting in strong flow anisotropy. Perhaps the most well-known micromechanically-based phenomenological model for anisotropic hardening on (non-proportional) loading paths characterized by directional changes is that of Teodosiu and Hu (1995, 1998). The objective of the third Chapter is to propose a simplified formulation of the modified Teodosiu model presented by Wang et al. (2008). The simplified model and full model are then identified using the available experimental tests for ferritic steel LH800 and IF steel DC06. Finally, the model behavior for the full and simplified models is compared and discussed.

The fourth Chapter of the thesis is concerned with the identification of the material model for the steel LH800 using the different sets of tests. The effect of loading path changes during the metal forming processes is modeled by the material model presented in the first Chapter. Now,

there is a need for experiments that resemble most of the proportional and non-proportional loading path changes which occur during the real sheet metal forming processes. In the current work we used three types of test data, i.e. cyclic bending test data, tension-compression test data and reverse shear test data along with orthogonal tension shear data to identify the three different sets of material parameters of the presented material model. All three aforementioned tests involve different amounts of inelastic deformation and have different states of stress. Hence, it is instructive to compare the influence of the test data used for identification on the material model parameters. The identified sets of material parameters are then used to simulate a draw-bending test and predict the amount of springback. The predicted springback is then compared with the actual experimentally observed springback for each set of material parameters.

Accurate simulation of forming and springback in sheet metal forming processes requires taking a number of factors / parameters into account. The factors affecting the simulation of forming and springback fall in two categories: physical and numerical. In the fifth Chapter of this thesis, the attention is focused on the roles played by type, order and scheme of the finite element model and level of mesh refinement, which falls in the category of numerical parameters. For the physical parameters affecting the simulation of forming and springback, the effect of tool radius, friction coefficient, back force (sheet tension) and material model used are investigated. The goal here is an optimal choice of element type, mesh refinement, contact and friction modeling, as well as other numerical and physical parameters in such a way that an efficient, robust and converged solution is achieved in the context of the simulation of sheet metal forming and predicting the springback.



# Zusammenfassung

Die experimentelle und theoretische Untersuchung der Umformung von Blechen ist nach wie vor eine Herausforderung sowohl in der theoretischen Beschreibung als auch auf experimenteller Seite. Eine wesentliche Aufgabe kommt dabei der Verwendung eines realistischen Materialmodells zu. Das Modell sollte in der Lage sein, die Entwicklung der Mikrostruktur sowie die verschiedenen Formen der Verfestigung, die bei den komplexen Lastpfaden in der Blechumformung auftreten, zu berücksichtigen. Die Charakterisierung / Identifikation des Materialmodells muss für das jeweilige Material, basierend auf den vorliegenden experimentellen Spannung-Dehnung-Ergebnissen für unterschiedliche Beanspruchungsarten durchgeführt werden. Außerdem sind numerische und physikalische (strukturbezogene) Faktoren im Zusammenhang mit der Blechumformung zu betrachten. Diese Arbeit gehört in diesen Zusammenhang und befasst sich mit der Formulierung des Materialmodells, sowie seiner Anwendung bei der Berechnung von Blechumformprozessen. Verschiedene Faktoren, die die Umformsimulation und die Rückfederung beeinflussen, werden untersucht.

Bei komplexen Umformprozessen treten große plastische Verformungen und damit verbundene Fließanisotropie auf, die von der Entwicklung bleibender Versetzungsstrukturen verursacht wird. Der erste Teil dieser Arbeit befasst sich mit der Formulierung und Identifizierung eines phänomenologischen Modells, das den Einfluss der orientierten Versetzungsmikrostrukturen auf das anisotrope Verfestigungsverhalten berücksichtigt. Das Modell berücksichtigt die Änderungen der Größe, des Zentrums und der Form der Fließfläche, die mit isotroper-, kinematischer- und Querverfestigung in Verbindung stehen. Die Identifikation des ferritischen Stahls LH800 wird anhand von Scher-, Scher-Rückscher- und Zug-Scher-Tests durchgeführt. Das identifizierte Modell wurde durch Nachrechnen des Spannung-Dehnung-Zusammenhangs für verschiedene Zug-Scher-Lastpfade, zu denen experimentelle Ergebnisse vorlagen, validiert. Die Ergebnisse bzw. der Vergleich der theoretischen Vorhersagen mit den Experimentalergebnissen zeigen, dass Querverfestigungseffekte bei Stählen wie LH800 berücksichtigt werden müssen.

Umformungen bei Metall gehen mit großen Dehnungen und ausgeprägten Belastungspfadwechseln einher. Große plastische Dehnungen führen in vielen Metallen zu der Entwicklung von bleibenden Versetzungsstrukturen, was zu starker Fließanisotropie führt. Das vielleicht bekannteste mikromechanisch basierte phänomenologische Modell für anisotrope Verfestigung bei nicht-proportionalen Lastpfaden, die durch Richtungswechsel charakterisiert werden, ist das von Teodosiu und Hu (1995, 1998). Im dritten Kapitel wird eine vereinfachte Formulierung eines modifizierten Teodosiu Modells vorgeschlagen. Das vereinfachte Modell und das nicht vereinfachte Modell werden dann anhand der verfügbaren Versuchsergebnisse für den ferritischen Stahl LH800 und den IF-Stahl DC06 identifiziert. Schließlich werden die Modellverhalten des Vollmodells und des vereinfachten Modells miteinander verglichen.

Das vierte Kapitel der Arbeit befasst sich mit der Identifizierung des Materialmodells für den Stahl LH800 basierend auf verschiedenen Testdaten. Der Einfluss der Belastungspfad-

wechsel während des Umformens wird mit dem im ersten Kapitel präsentierten Materialmodell modelliert. Hierfür sind Experimente erforderlich, die den meisten proportionalen und nicht-proportionalen Lastpfadwechseln, wie sie in realen Blechumformprozessen auftreten, ähneln. In der vorliegenden Arbeit wurden drei Testarten verwendet, nämlich zyklische Biegeversuche, Zug-Druck-Versuche und Scher-Rückscher-Versuche im Zusammenhang mit orthogonalen Zug-Scher-Versuchen, um drei Parametersätze für das vorgestellte Modell zu bestimmen. Die erwähnten Tests beinhalten unterschiedlich hohe inelastische Deformationen und verschiedene Spannungszustände. Daher ist es sinnvoll, den Einfluss der zugrunde liegenden Versuche auf die Materialparameter zu untersuchen. Die identifizierten Datensätze werden dann für die Simulation eines Streifenzugbiegeversuchs verwendet. Dies beinhaltet auch die rechnerische Vorhersage der Rückfederung. Die berechnete Rückfederung wird für alle Datensätze mit der experimentell ermittelten Rückfederung verglichen.

Eine akkurate Berechnung des Tiefziehens und der Rückfederung gelingt nur, wenn man eine Reihe an Faktoren / Parametern berücksichtigt. Diese Einflussfaktoren lassen sich in die Kategorien physikalisch und numerisch einteilen. Das fünfte Kapitel dieser Arbeit befasst sich mit dem Einfluss des Typs, der Ordnung und des Integrationsschemas des verwendeten finiten Elements sowie mit dem Einfluss der Diskretisierung. Dies gehört zu der Kategorie der numerischen Parameter. Im Bereich der physikalischen Parameter, die das Berechnungsergebnis beeinflussen, werden der Radius des Tiefziehwerkzeugs, der Reibkoeffizient, die Haltekraft (Zugkraft im Blech) und das Materialmodell untersucht. Das Ziel dabei ist die optimale Wahl des Elementtyps, des Netzes, der Kontakt- und Reibungsmodellierung und anderer Parameter, sodass eine effiziente, robuste und konvergente Lösung für die Simulation der Blechumformung und der damit verbundenen Rückfederung gefunden werden kann.

# Chapter 1

## Introduction

The simulation of sheet metal forming continues to present a number of challenges for researchers. Among the foremost issues in this regard is a realistic model for the material behavior. The material model should be able to account for the effects of the microstructural development and the development of different types of hardening that evolve due to complex loading path histories involved in sheet metal forming processes. The initial anisotropy is represented by the grain microstructure in sheet metals and is determined almost solely by the rolling process. Forming processes like cup drawing are expected to result in little or no change in this microstructure. Consequently, during forming processes, anisotropic hardening behavior is generally expected to be due almost solely to an evolving dislocation microstructure at the grain- or grain-cluster level.

In Chapter two of the current work, a phenomenological model is presented which accounts for the effect of the evolution of this oriented dislocation microstructure on the anisotropic hardening behavior. The model accounts for changes in the size, center, and shape of the yield surface associated with isotropic, kinematic, and cross hardening, respectively. The presented model falls in the context of approach originally presented by Baltov and Sawczuk (1965). For the Baltov and Sawczuk (1965) type models, the yield locus is dependent on the loading path. The model is based on an evolution relation for the fourth order tensor accounting for the effects of an evolving dislocation microstructure on the hardening behavior. The initial value of this fourth order tensor is determined in the current model by the grain microstructure (i.e., texture). The current form of the evolution relation for this fourth order tensor is directly motivated by the evolution of the cell-wall dislocation microstructure (e.g., Nesterova et al. (2001)) during loading-path changes and its effect on hardening.

Perhaps the most well-known micromechanically-based phenomenological model for anisotropic hardening on (non-proportional) loading paths characterized by directional changes is that of Teodosiu and Hu (1995, 1998). The model proposed by Teodosiu and Hu (1995) accounts for cross-hardening, the Bauschinger effect and hardening stagnation. In their model the evolution of internal variables can be closely linked to the microstructural mechanisms inducing the transient mechanical response. The model introduces strong coupling between different contributions to anisotropic hardening. Central to the model is the introduction of a fourth-order tensor accounting for the interaction of dislocation structures during loading path changes. The effective yield stress depends on (the magnitude of) this fourth-order evolving structure tensor. Therefore, this model is called yield stress model here. The model is capable of accounting for isotropic, kinematic and directional hardening. The focus of the third Chapter is to present a simplified formulation of the (Teodosiu and Hu, 1995, 1998) model. This model has been

successfully applied to the simulation of sheet metal forming processes involving strain path changes (Oliveira et al., 2007; Wang et al., 2008, 2006). The simplification leads to a reduction of the coupling between different contributions of anisotropic hardening and a reduction in the number of parameters which have to be identified. The agreement of the mechanical responses predicted by the model with experimental test data and the full model is excellent.

After formulating the material model which is capable of describing the material behavior under most common but complex strain path changes, the next challenge lies in the identification of the material model using the available experiments. The most widely used experimental test to evaluate the strain-stress response for a monotonic strain path is the uniaxial tension test. But the identification of the afore mentioned material model can not be done only through uniaxial tensile tests, and therefore other loading paths need to be investigated for the identification of material parameters. To obtain a strain reversal in the loading path (for the Bauschinger effect), the tests which have to be investigated are tension-compression tests (Yoshida et al. (2002)), reverse shear tests (Bouvier et al. (2006); Noman et al. (2010)) and cyclic pure bending tests (Boers et al. (2010); Brunet et al. (2001); Yoshida et al. (1998)). The conventional tension-compression tests are commonly used for the identification of material parameters over the decades, but these tests are generally very difficult to perform due to the buckling of the sheet sample (Yoshida et al. (2002)). To overcome this problem, Yoshida et al. (1998) suggested a pure bending test and performed cyclic bending of thin sheets. Based on cyclic bending test data, Yoshida et al. (1998) identified the material parameters for a combined isotropic and kinematic hardening model by using an optimization technique based on the iterative approximation concept. Later, Brunet et al. (2001) used cyclic bending test data simultaneously with the tensile test data to identify the hardening parameters using an inverse approach. Carbonnière et al. (2009) recently performed a comparison of work hardening using the identified parameters from one cycle of a bending test and compared it with reverse shear test data. It should be noted that, in a bending test, the maximum strain reached in each cycle for thin sheet metal of 1 mm thickness is around 0.05 which is rather small. The simple shear tests performed by Rauch (1998); Z. Hu and Teodosiu (1992) and more recently by Bouvier et al. (2006); Flores et al. (2007); Haddadi et al. (2006); van Riel and van den Boogaard (2007) have shown that large amplitudes of strain can be achieved, which is suitable for identifying isotropic and kinematic hardening parameters at large level of strains. In order to identify the cross hardening parameters, a test involving an orthogonal or quasi orthogonal strain path has to be used in the identification. This is achieved by using the orthogonal tension-shear tests (Bouvier et al. (2006); Haddadi et al. (2006); van Riel and van den Boogaard (2007)). Recently, Bouvier et al. (2006); Flores et al. (2007); Haddadi et al. (2006); Noman et al. (2010) successfully used the orthogonal tension shear test for the identification of cross hardening parameters.

The experimental setup and detailed results of the simple reverse shear and orthogonal tension-shear tests are presented in Chapter two and Chapter three for the ferritic steel LH800, and in appendix A for the ferritic steel DC06. In Chapter four of the current work, an overview of three different experimental tests i.e. cyclic bending test, tension-compression test and simple reverse shear test along with orthogonal tension shear test are presented along with their results.

The identification of the material model needs to be performed for the specific material using

the available experiments that produce strain-stress responses for different loading paths. The material parameter is identified by using the program LS-OPT in conjunction with LS-DYNA. The optimization technique used relies on response surface methodology (RSM) (Stander et al. (2008)), a mathematical method for constructing smooth approximations of functions in a design space. The approximations are based on results calculated at numerous points in the multi-dimensional design space. In our example, the material parameters are the design variables, and the model together with the data determine the objective function of the corresponding optimization problem. In Chapter two, the identification of the model for the ferritic sheet metal steel LH800 is carried out with the help of shear, reverse shear, and tension-shear tests. The identified model has been validated by using it to predict the stress-strain behavior of the material along different tension-shear loading paths and comparison with analogous experimental results. Chapter three deals with the identification of the full yield stress and simplified yield stress models on the basis of monotonic shear, reverse shear and tension-shear tests for ferritic steel LH800. The corresponding results for the steel DC06 are presented in Appendix A. In the fourth Chapter, a study is conducted to investigate the influence of the test-data, i.e. uniaxial tension-compression, simple reverse shear and cyclic pure bending, on the material model parameters. The results obtained using different test data are then compared in order to analyze the influence of the database used.

Finally, in Chapter five, the parameters influencing the simulation of sheet metal forming processes and springback prediction are studied. In general, the numerical simulation of the metal forming process and springback prediction is influenced by two different kinds of parameters: physical and numerical. The physical group of parameters includes both material properties, such as isotropic and kinematic hardening, Bauschinger effect, distortional hardening, elastic and plastic anisotropy (Carden et al. (2002), Laurent et al. (2009), Geng and Wagoner (2002), Oliveira et al. (2007) and Li et al. (2002), Eggertsen and Mattiasson (2009, 2010), and Wang et al. (2006) ) and process characteristics sensitiveness, such as sheet thickness, friction coefficient, blank holder force, tool geometry (e.g. radius), temperature and unloading procedure (Li et al. (2002) and Wang et al. (2005)). The numerical parameters influencing springback are the type of element, order and integration scheme of the finite element, as well as, the shape, size and the finite element mesh refinement (Li et al. (2002), Xu et al. (2004), Meinders et al. (2008)).



## Chapter 2

# Experimental characterization and modeling of the hardening behavior of the sheet steel LH800

**Abstract**– In complex forming processes, sheet metal undergoes large plastic deformations involving significant induced flow anisotropy resulting from the development of persistent oriented (planar) dislocation structures. The aim of the present work is the formulation and identification of a phenomenological model which accounts for the effect of the evolution of this oriented dislocation microstructure on the anisotropic hardening behavior. The model accounts for changes in the size, center, and shape, of the yield surface associated with isotropic, kinematic, and cross hardening, respectively. Identification of the model for the ferritic sheet metal steel LH800 is carried out with the help of shear, reverse shear, and tension-shear tests. The identified model has been validated using it to predict the stress-strain behavior of the material along different tension-shear loading paths and comparison with analogous experimental results. The results and in particular the comparison of theoretical predictions with experimental results clearly demonstrate the need of including cross hardening effects in the modeling of sheet metals like LH800.

### 2.1 Introduction

The experimental and theoretical characterization of sheet metal forming continues to present a number of challenges for theorist and experimentalist alike. Among the foremost issues in this regard is a realistic model for the material behavior. Metal forming processes generally involve large strain resulting in significant microstructural development and the development of different types of hardening. The influence of a developing microstructure on the hardening behavior in sheet metals has been the subject of many investigations (e.g. Aretz, 2008; Barlat et al., 2003; Bouvier et al., 2005, 2006, 2003; Hiwataishi et al., 1997, 1998; Hoc and Forest, 2001; Li et al., 2003; Peeters et al., 2001a, 2002, 2001b; Teodosiu and Hu, 1995, 1998; Wang et al., 2008). The nature and strength of this influence is strongly dependent on the type and complexity of the loading paths under consideration. As discussed for example by Barlat et al. (2003), in the case of monotonic loading, the grain microstructure (i.e., texture) influences strongly the dependence of hardening on the loading direction. In contrast, for loading paths with changes in direction, this behavior is dominated by the dislocation microstructure. Experimentally-observed effects in this context include hardening stagnation after load reversal, and cross hardening after orthogonal loading. Experimental results exhibiting these effects exist for a number of different materials. Systematic studies of interstitial free (IF), high-strength low alloyed (HSLA), dual-phase (DP) and transformation-induced plasticity (TRIP), steels, as well

as 5000 and 6000 series aluminum alloys, conducted by Bouvier et al. (2006, 2003) found significant kinematic hardening, hardening stagnation, as well as cross-hardening, especially for IF steels. In their investigations, the blank material was subjected to monotonic shear, reverse shear, as well as orthogonal tension-shear, loading. van Riel and van den Boogaard (2007) have documented these effects in IF ferritic steels with the help of monotonic tension, reverse shear, and orthogonal tension-shear, tests, all under plane-strain conditions.

Perhaps the most well-known micromechanically-based phenomenological model for anisotropic hardening on (non-proportional) loading paths characterized by directional changes is that of Teodosiu and Hu (1995, 1998). Besides accounting for isotropic and kinematic hardening, their model accounts for cross hardening via an evolving fourth-order tensor  $\mathcal{S}$  influencing the effective yield stress in a loading-direction-dependent fashion. In the current back-rotated framework relevant to metals, the yield function for this model takes the form

$$\phi_{\text{Teo}} = \sqrt{(\mathbf{M} - \mathbf{X}) \cdot \mathcal{A}_{\text{Teo}} (\mathbf{M} - \mathbf{X})} - \sigma_{\text{Teo}}. \quad (2.1)$$

Here,  $\mathbf{M}$  represents the Mandel stress,  $\mathbf{X}$  the back stress,  $\mathcal{A}_{\text{Teo}}$  the Teodosiu flow anisotropy tensor, and  $\sigma_{\text{Teo}}$  the Teodosiu yield stress. In particular,  $\mathcal{A}_{\text{Teo}} \equiv \mathcal{A}_{\text{Hill}}$  is modeled by the constant Hill (1950) initial flow anisotropy tensor  $\mathcal{A}_{\text{Hill}}$  determined by grain microstructure (i.e., texture). Further,  $\sigma_{\text{Teo}} \equiv \sigma_{Y0} + r + f |\mathcal{S}|$  is determined by (i) the initial yield stress  $\sigma_{Y0}$ , (ii) the increase  $r$  in this stress due to standard isotropic hardening, and (iii) the increase  $f |\mathcal{S}|$  in this stress due to cross hardening.  $f$  represents the fraction of dislocation walls contributing to isotropic hardening whose strength in this sense is given by the magnitude  $|\mathcal{S}| := \sqrt{\mathcal{S} \cdot \mathcal{S}} = \sqrt{S_{ijkl} S_{ijkl}}$  of  $\mathcal{S}$ . Since  $\mathbf{M}$  and  $\mathcal{S}$  are decoupled in  $\phi_{\text{Teo}}$ , note that the evolution of  $\mathcal{S}$  does not influence the form of the yield surface as represented by the dependence of  $\phi_{\text{Teo}}$  on  $\mathbf{M}$ . For more details on this class of models as well as applications, the reader is referred to Oliveira et al. (2007); Wang et al. (2008).

An alternative class of models for cross and more generally distortional hardening can be based on the approach of Baltov and Sawczuk (1965). In the current framework, this involves in particular a yield condition of the form

$$\phi_{\text{Bal}} = \sqrt{(\mathbf{M} - \mathbf{X}) \cdot \mathcal{A}_{\text{Bal}} (\mathbf{M} - \mathbf{X})} - \sigma_{\text{Bal}}, \quad (2.2)$$

with  $\sigma_{\text{Bal}} \equiv \sigma_{Y0} + r$ . Besides the additional dependence of  $\sigma_{\text{Teo}}$  on  $\mathcal{S}$ , then, the basic difference between  $\phi_{\text{Teo}}$  and  $\phi_{\text{Bal}}$  lies in the fact that  $\mathcal{A}_{\text{Bal}}$  is not assumed constant. Its evolution is governed by a constitutive relation, and its initial value is given by  $\mathcal{A}_{\text{Hill}}$ . A number of models for this evolution have been proposed in the literature, including the current one. For example, Voyiadjis and Foroozesh (1990) proposed an evolution relation for  $\mathcal{A}_{\text{Bal}}$  based on three material parameters which mediate an assumed coupling between its principal directions and the effective stress  $\mathbf{M} - \mathbf{X}$ , resulting in asymmetric distortion of the yield surface. The model of Schick (2004), which is based on the approach of Dafalias et al. (2003), assumes multiple kinematic hardening mechanisms and a dependence of the evolution of  $\mathcal{A}_{\text{Bal}}$  on kinematic hardening in order to model yield surface development during tension-torsion loading (Ishikawa, 1997). Evolution of the yield surface has also been modeled by Yeganeh (2007) in a rigid-plastic framework as based on the Hencky logarithmic strain. More recently, the model of Feigenbaum and Dafalias



(2007) involves an evolution relation for  $\mathcal{A}_{\text{Bal}}$  coupled to the magnitude of the effective stress and the projection of the direction of the effective stress onto the back stress. This leads to an asymmetric distortion of the yield surface with increasing curvature in the direction of distortion in stress space. In Feigenbaum and Dafalias (2008), a simplified version of such a model is developed in which there is no coupling to the evolution of the back stress. Development of these types of models has been motivated by tension-torsion experiments on aluminum and steel tubes (e.g., Boucher and Cordebois, 1994; Ishikawa, 1997; Phillips et al., 1974). In Boucher and Cordebois (1994); Phillips et al. (1974), a distortion of the yield surface in the direction of applied stress was determined. This involved an increase in curvature of the yield surface in this direction and a corresponding decrease in curvature in the opposite direction.

The purpose of the current work is to introduce and validate a new model for cross hardening and hardening stagnation during orthogonal loading in the context of the approach of Baltov and Sawczuk (1965). This is based on an evolution relation for  $\mathcal{A}_{\text{Bal}}$  accounting for the effects of an evolving dislocation microstructure on the hardening behavior. Like many of the models discussed above, the initial value of  $\mathcal{A}_{\text{Bal}}$  is determined in the current model by the grain microstructure (i.e., texture). In contrast to these models, however, the current form of the evolution relation for  $\mathcal{A}_{\text{Bal}}$  is directly motivated by the evolution of the cell-wall dislocation microstructure (e.g., Nesterova et al. (2001)) during loading-path changes and its effect on hardening. An analogous form was formulated for  $\mathcal{S}$  in the model of Wang et al. (2008). On the one hand, this results in a model which is simpler than either that of Teodosiu and Hu (1998) or Wang et al. (2008) and contains fewer material parameters. On the other hand, the current model is not capable of representing hardening stagnation after reverse loading. Micromechanical support for working with a model based on (2.2) rather than on (2.1), i.e., with a model in which cross hardening is associated with a change in the shape of the yield surface, i.e., distortional hardening, comes for example from the very interesting work of Peeters et al. (2002). They worked with a polycrystal model based on fully-constraint Taylor-based homogenization which takes the evolution of the dislocation microstructure into account at the grain level in an effective fashion. Using this approach, they were able to simulate the cross effect in orthogonal tension-shear tests and a corresponding change in shape of the yield surface. In particular, the development of dislocation walls at the grain level during proportional loading corresponds to the expansion of the yield surface into directions orthogonal to the loading direction. On the other hand, the development of localization bands and the breakdown of existing dislocation structures after orthogonal change of direction leads to yield surface shrinkage in the new direction of loading. Besides the stress-strain- and loading-path-based data which will be presented in this work, that of Ishikawa (1997) for yield surface development in the stainless steel SUS304 during tension-torsion exhibits (some of) these effects and in particular a change in shape of the yield surface.

The current work begins in Section 2 with a formulation of the current model in the framework of the multiplicative decomposition of the deformation gradient and the assumption of small elastic strain relevant to metal inelasticity. In order to identify and validate the model, tension-shear and cyclic shear tests on the ferritic steel LH800 (Tekkaya et al. (2008)) have been carried out. The experimental setup and details of these tests together with the basic data are presented in Section 3. The strategy developed for the model identification together with

the results of this identification are discussed in Section 4. The model is also validated in this section with the help of additional test results for other strain paths not used in the model identification. In Section 5, the identified model is used to investigate the evolution of the yield surface and that of the inelastic state with respect to loading-path history. Finally, the work ends in Section 6 with a discussion and conclusions.

## 2.2 Model formulation

The phenomenological representation of evolving hardening behavior in terms of changes in the size, center and shape of the yield surface offers the means to characterize the behavior of the steels of interest during complex, non-proportional loading processes present in many technological processes (e.g., deep-drawing). The challenge lies in the connection of such changes in the yield surface geometry with the underlying microscopic and physical mechanisms of grain and dislocation microstructural development in polycrystalline metals. One basic expectation in this regard is that the grain microstructure in sheet metals is determined almost solely by the rolling process. Forming processes like cup drawing are expected to result in little or no change in this microstructure. Consequently, during forming processes, yield surface evolution is generally expected to be due almost solely to an evolving dislocation microstructure at the grain- or grain-cluster level. This is the focus of the current model.

The formulation of the current model is carried out in the framework of the standard inelastic multiplicative decomposition  $\mathbf{F} = \mathbf{F}_E \mathbf{F}_P$  of the deformation gradient  $\mathbf{F}$  (e.g., Simo and Hughes, 1998). Such a decomposition arises naturally, e.g., in the context of the modeling of  $\mathbf{F}_P$  as a change of local reference configuration (Svendsen, 2001). In this context, one obtains in particular the result

$$\mathbf{R}_E^T \mathbf{L}_E \mathbf{R}_E = \mathbf{R}_E^T \mathbf{L} \mathbf{R}_E - \mathbf{U}_E \mathbf{L}_P \mathbf{U}_E^{-1} = \mathbf{R}_E^T \dot{\mathbf{R}}_E + \dot{\mathbf{U}}_E \mathbf{U}_E^{-1} \quad (2.3)$$

via the right polar decomposition  $\mathbf{F}_E = \mathbf{R}_E \mathbf{U}_E$  of  $\mathbf{F}_E$  for the back-rotated form of  $\mathbf{L}_E := \dot{\mathbf{F}}_E \mathbf{F}_E^{-1}$  in terms of  $\mathbf{L} := \dot{\mathbf{F}} \mathbf{F}^{-1}$  and  $\mathbf{L}_P := \dot{\mathbf{F}}_P \mathbf{F}_P^{-1}$ . For the current case of polycrystalline metals and small elastic strain, we have

$$\begin{aligned} \mathbf{U}_E &\approx \mathbf{I} + \ln \mathbf{U}_E, \\ \dot{\mathbf{U}}_E \mathbf{U}_E^{-1} &\approx \overline{\ln \dot{\mathbf{U}}_E}. \end{aligned} \quad (2.4)$$

Substituting these into (2.3), and taking the symmetric and skew-symmetric parts of the result, one obtains the evolution relations

$$\begin{aligned} \overline{\ln \dot{\mathbf{U}}_E} &= \mathbf{R}_E^T \mathbf{D} \mathbf{R}_E - \mathbf{D}_P, \\ \dot{\mathbf{R}}_E &= \mathbf{W} \mathbf{R}_E - \mathbf{R}_E \mathbf{W}_P, \end{aligned} \quad (2.5)$$

for  $\ln \mathbf{U}_E$  and  $\mathbf{R}_E$ , respectively, in the incremental context.  $\mathbf{D} := \text{sym}(\mathbf{L})$  is the continuum rate of deformation,  $\mathbf{D}_P := \text{sym}(\mathbf{L}_P)$  its inelastic counterpart,  $\mathbf{W} := \text{skw}(\mathbf{L})$  the continuum spin, and  $\mathbf{W}_P := \text{skw}(\mathbf{L}_P)$  the plastic spin. Restricting the current formulation to the case of sheet metal forming, it is reasonable to assume that the texture in these materials achieved

during rolling remains largely unchanged during forming processes like tension, compression, simple shear, cyclic simple shear, and combinations of these. In this case,  $\mathbf{W}_P$  is negligible, and the evolution of  $\mathbf{R}_E$  depends only on  $\mathbf{W}$ , in which case it reduces to a purely kinematic quantity (i.e., the Jaumann rotation). In addition, focusing in this work on the material behavior of sheet metal during forming below the forming limit, we assume for simplicity that damage or any other processes resulting in inelastic volume changes are negligible. In this case, plastic incompressibility  $\det(\mathbf{F}_P) = 1$  pertains, implying  $\text{tr}(\mathbf{D}_P) = 0$  and  $\mathbf{D}'_P = \mathbf{D}_P$  in the incremental context.

Since the elastic range and elastic strains are small, any texture effects from rolling leading to an anisotropic elastic behavior are assumed negligible. In this case, the isotropic form

$$\mathbf{M} = \kappa \text{tr}(\mathbf{E}_E) \mathbf{I} + 2\mu \mathbf{E}'_E \quad (2.6)$$

is assumed for the Mandel stress  $\mathbf{M}$  in terms of the elastic strain  $\mathbf{E}_E := \ln \mathbf{U}_E$ , bulk modulus  $\kappa$ , shear modulus  $\mu$ , and deviatoric part  $\mathbf{E}'_E$  of  $\mathbf{E}_E$ . Lastly, again in the framework of small elastic strain,  $\mathbf{M}$  and  $\mathbf{R}_E$  determine the Kirchhoff stress  $\mathbf{K}$  via

$$\mathbf{K} = \mathbf{R}_E \mathbf{M} \mathbf{R}_E^T. \quad (2.7)$$

Consequently, in contrast to  $\mathbf{K}' = \mathbf{R}_E \mathbf{M}' \mathbf{R}_E^T$ ,  $\text{tr}(\mathbf{K}) = \text{tr}(\mathbf{M})$  of  $\mathbf{K}$  is independent of  $\mathbf{R}_E$ .

In this framework, then, the material behavior of polycrystalline sheet metal during forming processes below the forming limit is predominantly determined by a changing dislocation microstructure and attendant evolving anisotropic yield behavior. Besides a shift of the yield surface and its proportional expansion as in the case of conventional combined hardening, the current model also accounts for an evolving yield surface shape and so distortional hardening. As discussed in the introduction, this model is based in particular on a yield function of the form (2.2) from Baltov and Sawczuk (1965). In the current notation, this is written simply in the form

$$\phi = \sqrt{(\mathbf{M} - \mathbf{X}) \cdot \mathcal{A}(\mathbf{M} - \mathbf{X})} - \sigma_{Y0} - r \quad (2.8)$$

in terms of the initial yield stress  $\sigma_{Y0}$ . For the class of materials under consideration, the saturation (i.e., Voce) form

$$\dot{r} = c_r (s_r - r) \dot{\alpha}_P \quad (2.9)$$

for the evolution of  $r$  is appropriate, driven by that of the equivalent inelastic deformation  $\alpha_P$ . Here,  $c_r$  represents the rate, and  $s_r$  the value, for saturation associated with  $r$ . Since  $\sigma_{Y0}$  is the initial yield stress (i.e., for  $\alpha_P = 0$ ), the initial value  $r_0$  of  $r$  is zero. In the current rate-independent context,  $\alpha_P$  is determined as usual by the consistency condition. Analogous to isotropic hardening, kinematic hardening is modeled via the saturation (i.e., Armstrong-Frederick) form

$$\dot{\mathbf{X}} = c_x (s_x \mathbf{N}_P - \mathbf{X}) \dot{\alpha}_P \quad (2.10)$$

for the evolution of  $\mathbf{X}$  depending on corresponding (constant) saturation rate  $c_x$ , (constant) saturation magnitude  $s_x$ , as well as the (variable) direction  $\mathbf{N}_P := \mathbf{D}_P / |\mathbf{D}_P|$  of the rate of inelastic deformation

$$\mathbf{D}_P = \dot{\alpha}_P \partial_{\mathbf{M} - \mathbf{X}} \phi, \quad (2.11)$$

which is modeled here in associated form. The initial value of  $\mathcal{X}$  is assumed to be zero.

The constitutive model formulation is completed by an evolution relation for  $\mathcal{A}$  in order to represent the effect of cross hardening on the material behavior. The form of this relation introduced in what follows is based on the idea that active or “dynamic” dislocation microstructures oriented with respect to the current loading direction (idealized in the model context by  $\mathbf{N}_P$ ) persist and become inactive or “latent” after a loading-path change and strengthen existing obstacles to glide-system activation in the new loading direction. In addition, both dynamic and latent dislocation structures are assumed to saturate with increasing accumulated inelastic deformation. These assumptions are built into the constitutive relation

$$\begin{aligned} \dot{\mathcal{A}} &= c_d (s_d \mathbf{N}_P \otimes \mathbf{N}_P - \mathcal{A}_d) \dot{\alpha}_P \\ &+ c_l \{s_l (\mathcal{I}_{\text{dev}} - \mathbf{N}_P \otimes \mathbf{N}_P) - \mathcal{A}_l\} \dot{\alpha}_P \end{aligned} \quad (2.12)$$

for the evolution of  $\mathcal{A}$ . Here,  $\mathcal{I}_{\text{dev}}$  is the deviatoric part of the fourth-order identity tensor, and

$$\begin{aligned} \mathcal{A}_d &:= (\mathbf{N}_P \cdot \mathcal{A} \mathbf{N}_P) \mathbf{N}_P \otimes \mathbf{N}_P, \\ \mathcal{A}_l &:= \mathcal{A} - \mathcal{A}_d, \end{aligned} \quad (2.13)$$

represent the “dynamic” and “latent” parts of  $\mathcal{A}$ , respectively. More precisely, these are the projections of  $\mathcal{A}$  parallel and orthogonal, respectively, to the current (instantaneous) inelastic flow direction  $\mathbf{N}_P$ . The first term in (2.12) is of the saturation type with respect to  $\mathcal{A}_d$ , with  $c_d$  the rate of saturation, and  $s_d \mathbf{N}_P \otimes \mathbf{N}_P$  the saturation value, respectively, of  $\mathcal{A}_d$ . Likewise,  $c_l$  is the saturation rate, and  $s_l (\mathcal{I}_{\text{dev}} - \mathbf{N}_P \otimes \mathbf{N}_P)$  the saturation value, of  $\mathcal{A}_l$ . The initial value  $\mathcal{A}_0$  of  $\mathcal{A}$  is determined by any Hill initial flow orthotropy due to any texture from rolling. In contrast to some of the models discussed in the introduction, e.g., Teodosiu and Hu (1998), Wang et al. (2008), or Dafalias et al. (2003); Feigenbaum and Dafalias (2007), note that there is no direct coupling between kinematic and distortional hardening in the current model. This is also the case in the recent model of Feigenbaum and Dafalias (2008), which focuses on the asymmetric development of the yield surface rather than on the effect of cross hardening as is done in the current work.

The current material model was implemented in the commercial FE codes ABAQUS and LS-DYNA via the user material interfaces provided. Besides the two elasticity parameters  $\kappa$ ,  $\mu$  and the 6 parameters (e.g., in the sense of Hill:  $F$ ,  $G$ ,  $H$ ,  $L$ ,  $M$ ,  $N$ ) for the initial flow orthotropy, this model contains 8 hardening parameters  $c_r$ ,  $s_r$ ,  $c_x$ ,  $s_x$ ,  $c_d$ ,  $s_d$ ,  $c_l$ ,  $s_l$  which have to be identified using the tests described next.

## 2.3 Material testing

The experimental work has been carried out on a biaxial testing device capable of loading a sheet metal specimen in both simple shear and in plane-strain tension. Using this device, one can carry out single- or multi-stage loading programs consisting of monotonic (e.g., forward simple-shear), reverse (e.g., forward-reverse simple-shear), and / or orthogonal (e.g., tension-shear) changes of loading direction. In particular, the latter can be carried out with or without unloading of the specimen upon change of loading direction.

## 2.3.1 Test setup

The biaxial testing equipment had been developed at the University of Twente. It consists of a regular uniaxial testing device which via an actuator is used to achieve plane-strain tension in the sample. A subframe mounted between the cross bars accommodates the actuator for simple shear deformation. The deformation is applied to the sample as indicated in Figure 2.1. The

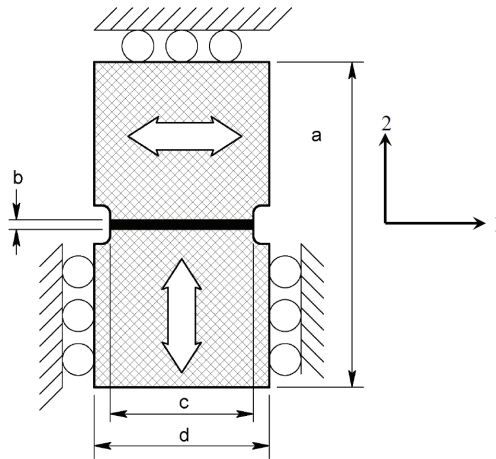


Figure 2.1: Biaxial test setup. Geometry of the tension-shear specimen and the measurement region of height  $b$  and width  $c$ . The checkered region indicates the actual specimen and the black area marks the actual deformation zone. The tension direction is direction 2 and the shear direction is direction 1.

ratio of the height ( $b$ ) of the measurement region to the sample thickness is chosen in order to minimize the chance of buckling during simple shear. In addition, to achieve homogeneous deformation in the measurement area  $c/b$  is large as shown in Figure 2.1. The deformation is measured in an area within the deformation zone. The notched boundary then constrains the specimen in the transverse direction during tension or shear, resulting in plane-strain conditions.

The deformation field is determined by optical measurement (in a procedure comparable to the commercially available ARAMIS system). To this end, the motion of an array of sixteen black silicon dots painted on the surface of the measurement area is tracked and recorded with a camera. The relative motion of these dots is used to calculate the deformation gradient via a least-squares method. During a test, two sensors on the actuators record the force achieved in shear and in tension. Using the known geometry of the specimen, these force measurements are used to calculate the Cauchy tensile and shear stress,  $T_{22}$  and  $T_{12}$ , respectively. The plane-strain tension and simple shear tests represent the boundaries of the range of stress states achievable in the specimen with the help of the biaxial testing device (Figure 2.1). By applying different combinations of simple shear and plane-strain tension, different stress states on the yield surface are achieved. The exact position of the yield state in principal stress space, however, is unknown since the transverse stress cannot be measured. Further details of the experimental setup can be found in van Riel and van den Boogaard (2007).

### 2.3.2 Test results

For the current work, tests performed on specimens of the ferritic steel LH800 include (i) monotonic plane-strain tension at different strain-rates, (ii) reverse simple-shear for different amounts of forward pre-shear, and (iii) orthogonal tension-shear with and without unloading. This sheet steel is characterized by an initial texture consisting of fine-grained ferrite, grain size of approximately  $8\ \mu\text{m}$  in diameter, see Figure 2.2 (Tekkaya et al. (2008)). The thickness of the sheet metal specimens used in all the tests was 0.7 mm. Experimental characterization of the steel DC06 can be found in Appendix A. All tests were performed with the tension direction oriented in the rolling direction. Consider first the monotonic plane-strain tension tests. As stated

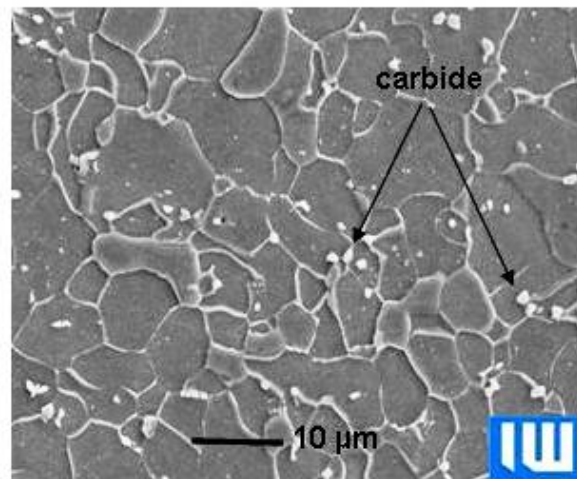


Figure 2.2: Scanning electron micrograph showing microstructure of LH800 (Experiment IW Hannover).

above, these have been performed at different strain rates. Figure 2.3 displays the corresponding results. As observed in many metals, the flow stress in LH800 increases as a function of increasing strain-rate. The remaining tests have been performed under quasi-static conditions (i.e.,  $10^{-3}\ \text{s}^{-1}$ ). Figure 2.4 shows the results of two reverse simple-shear tests. The elastic-inelastic transition for this material upon load reversal is very diffuse. The Bauschinger effect is clearly present. It would appear that the amount of pre-shear does not influence the magnitude of the Bauschinger effect significantly. On the other hand, the test with the larger pre-shear is clearly closer to the hardening saturation level. Hardening stagnation after load reversal is clearly visible in both cases, but less pronounced at lower pre-shear.

Lastly, consider the results from the orthogonal tests. As stated above, these consist of plane-strain tension followed by simple shear loading. The transition from tension to simple shear is either discontinuous via intermediate unloading, or continuous without unloading. The data so obtained include the 5 different continuous loading paths (numbered 1 to 5) shown in Figures 2.5 and 2.6.

Consistent with existing interpretations of such data in the literature, the presence or absence of cross hardening in such orthogonal tests is judged solely by comparison with the monotonic simple shear results. In particular, any overshoot of the yield stress above the monotonic level upon transition from tension to shear is an indicator of such hardening. Using this “definition,”

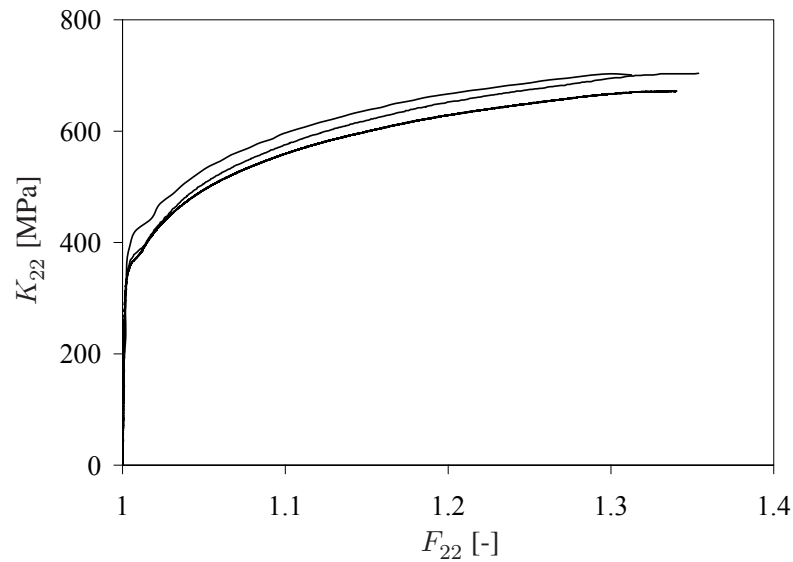


Figure 2.3: Tension test results for LH800 at strain rates of  $10^{-1} \text{ s}^{-1}$  (upper curve),  $10^{-2} \text{ s}^{-1}$  (middle curve),  $10^{-3} \text{ s}^{-1}$  (lowest curve).  $K_{22}$  represents the relevant component of the Kirchhoff stress and  $F_{22}$  represents the relevant component of the deformation gradient.

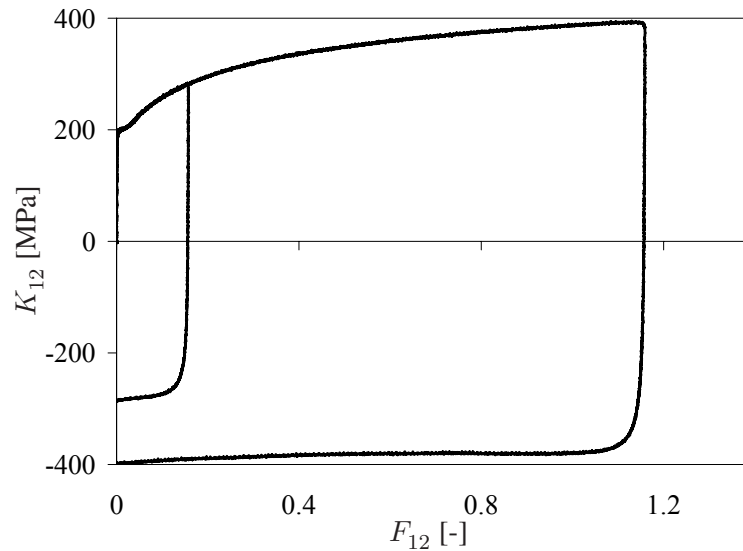


Figure 2.4: Reverse shear test results for LH800 for two different levels (i.e., 0.1 and 0.65) of pre-shear. All stress results are shown in absolute value form.

curves 1, 2 and 3 in Figure 2.5 clearly exhibit cross hardening as can be seen in Figure 2.6, curve 4 might exhibit a little, and curve 5 clearly none at all. In the one extreme (path 1), the orthogonal change is realized via an “abrupt” reduction in tension and coincident increase in shear at yield. This is closest to the case of a discontinuous orthogonal loading-path change as shown in Figure 2.7. In the other extreme (path 5), the level of tension is maintained (and further tensile deformation occurs) as shear loading increases. As indicated, the other three

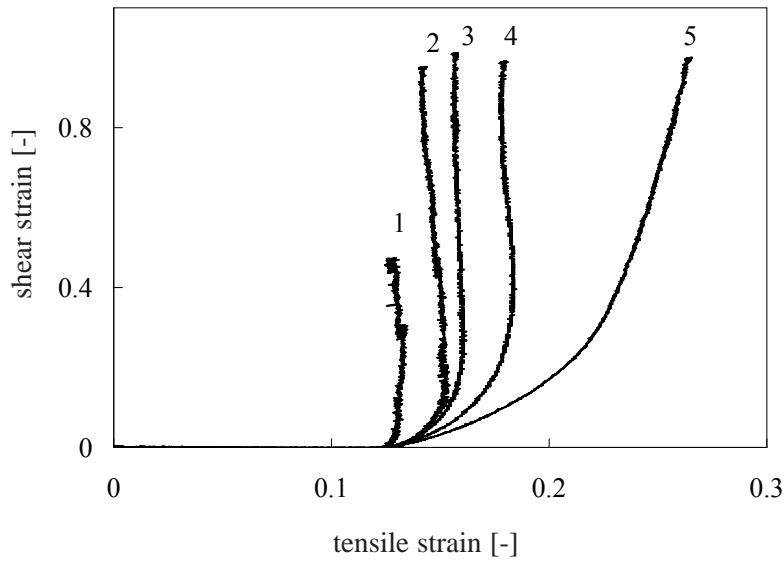


Figure 2.5: Experimental strain paths in LH800 resulting from continuous change of loading direction from tension to shear.

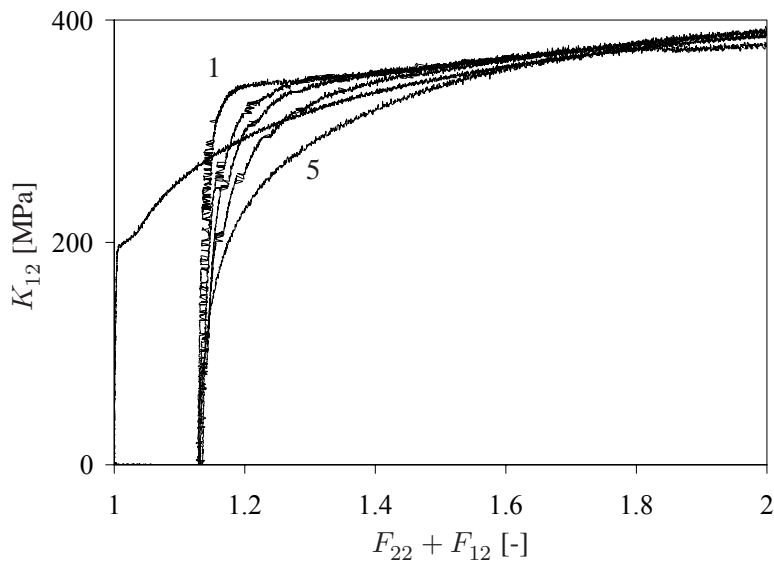


Figure 2.6: Stress response of LH800 for monotonic forward simple shear (curve starting at  $F_{22} + F_{12} = 1$ ) and for the 5 different orthogonal tension-shear paths shown in Figure 2.5.

paths (2, 3, and 4) in Figure 2.5 represent intermediate cases between these extremes.

In Figure 2.8, the paths in the  $(K_{12}, K_{22})$  stress plane are shown which correspond to (i) discontinuous orthogonal loading (curve “dis” in Figure 2.7) as well as, from Figure 2.5, (ii) continuous orthogonal loading path 3 and (iii) continuous orthogonal loading path 5.

The stress states A, B and C correspond to deformation states of equal  $F_{22} + F_{12}$  which intersect continuous path 5, continuous path 3 and the discontinuous path, respectively. The intersections of the vertical dashed line in Figure 2.7 with the stress curves mark the same



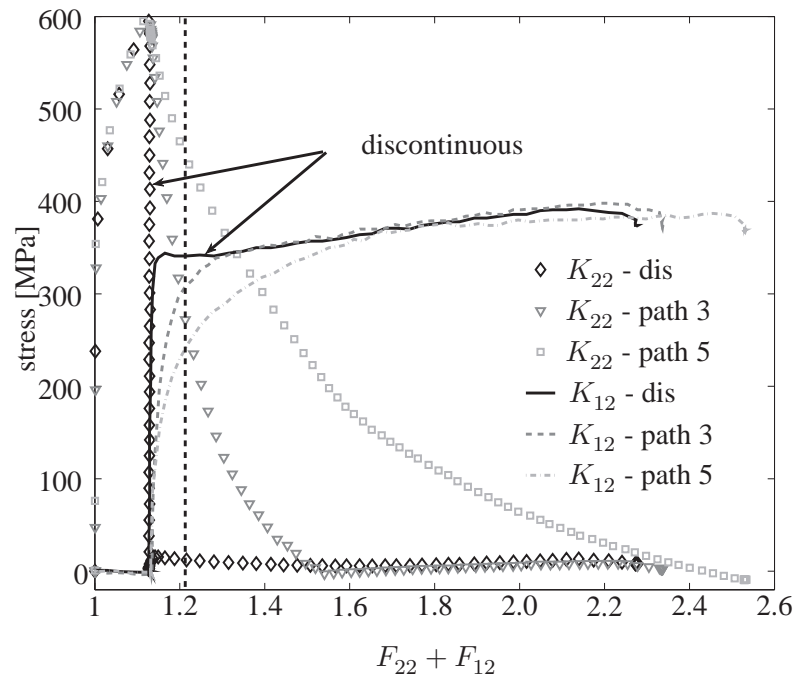


Figure 2.7: Discontinuous and continuous orthogonal loading-path changes from tension to shear in LH800. Normal stress component  $K_{22}$  (symbols) and shear stress component  $K_{12}$  (lines) as a function of  $F_{22} + F_{12}$ [-]. The vertical dashed line indicates deformation states of equal  $F_{22} + F_{12}$ .

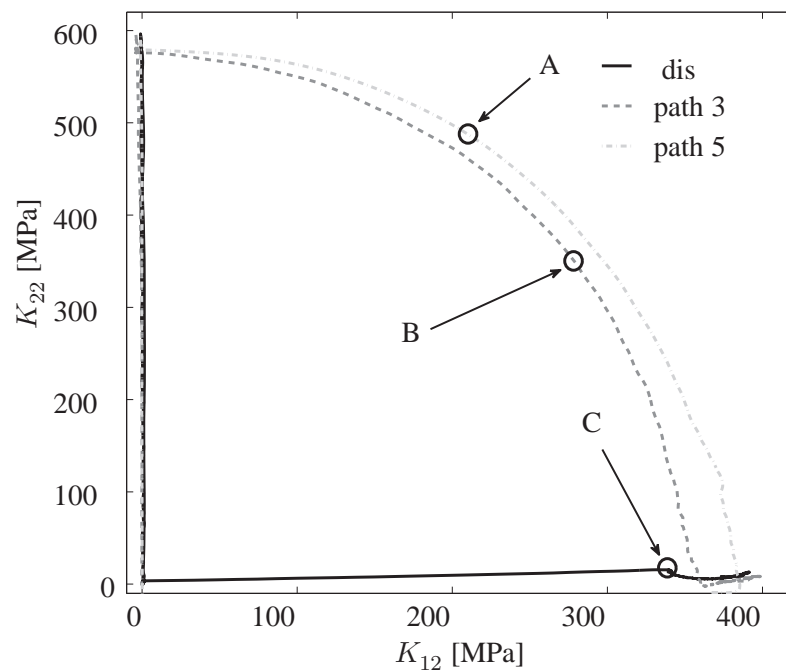


Figure 2.8: Experimental paths in  $(K_{22}, K_{12})$  stress space corresponding to selected paths shown in Figure 2.5 and 2.7. Points A, B and C mark the state of deformation corresponding to the intersection of the vertical dashed line in Figure 2.7 with the respective stress curves.

points, but in stress-deformation space. As implied by these results, the nature of the transition from tension to shear is crucial in determining whether or not cross hardening occurs, e.g., the increase in the yield stress above the monotonic shear level after an orthogonal change in loading path from tension to shear. Beyond being associated with stress states on the yield surface which are not influenced by cross hardening, cases 4 and 5 exhibit basically no cross hardening and are characterized by the fact that significant further tension loading takes place after the start of the shear loading phase. Assuming that the dislocation microstructure developed during the common pre-tension phase was the same in each case, these results imply that continued tension loading during simultaneous shear loading at yield facilitates a breakdown of tension-based dislocation microstructure which would otherwise result in cross hardening upon transition to shear. Besides this, note that the paths with continued tension loading do not return to the monotonic simple-shear reference curve, i.e., at least not within the range of the experimental data. These and other aspects will be examined in more detail after we carry out the model identification, to which we now turn.

## 2.4 Model identification

To demonstrate the capability of the presented model to describe the complex hardening behavior of LH800 during non-proportional loading just discussed, we now turn to its identification. As shown by the experimental data in the last section, this behavior involves in particular isotropic, kinematic, and cross hardening. The material parameter determination is carried out using the program LS-OPT in conjunction with LS-DYNA. Given the homogeneous nature of the tests, one-element calculations suffice. The optimization technique used relies on the response surface methodology (RSM) (Stander et al. (2008)). Other methods have been used by previous workers (e.g., Flores et al. (2007); Haddadi et al. (2006)) to identify related models like the Teodosiu model.

All fits to follow are based on the fixed values  $\kappa = 167.05$  GPa and  $\mu = 77.09$  GPa for the elastic properties, as well as  $\sigma_{Y0} = 330.79$  MPa for the initial yield stress, of LH800, all at room temperature. Tensile tests performed on LH800 at  $0^\circ$ ,  $45^\circ$ ,  $90^\circ$  with respect to the rolling direction yielded no distinct initial orthotropy and so Hill parameter values of  $F = G = H = 0.5$  and  $L = M = N = 1.5$ . Strictly speaking, only  $N$ ,  $F$ ,  $G$  and  $H$  can be determined by in-plane tensile tests. Isotropy is also in essence tacitly assumed for the case of through-thickness shear. The fit procedure for the hardening model begins by using monotonic simple-shear test data to identify the Voce isotropic hardening model alone, i.e., assuming no kinematic or cross hardening. The results of this fit are shown in Table 2.1 (left).

The quality of the fit can be judged via the comparison of the fitted model with the data in Figure 2.9. The isotropic hardening parameters so determined are then used as starting values to identify the isotropic-kinematic hardening model parameters using both monotonic and cyclic simple-shear test data. The results of this are shown in Table 2.1 (right). The quality of the model identification can be judged via comparison with the fit data as shown for the current combined (isotropic-kinematic) case in Figure 2.10. As can be seen in Figures 2.9, we use the experimentally-determined components of the deformation gradient  $\mathbf{F}$  to parameterize the experimental data for the model identification procedure. This is in contrast to the standard

|       | Value  | Units |
|-------|--------|-------|
| $s_r$ | 341.50 | MPa   |
| $c_r$ | 5.82   |       |

|       | Value   | Units |
|-------|---------|-------|
| $s_r$ | 245.684 | MPa   |
| $c_r$ | 4.295   |       |
| $s_x$ | 97.464  | MPa   |
| $c_x$ | 33.642  |       |

Table 2.1: Identified hardening model parameter values for LH800. Left: isotropic hardening parameter values determined from monotonic simple-shear test data alone. Right: isotropic-kinematic hardening parameters determined from monotonic and cyclic simple-shear test data alone.

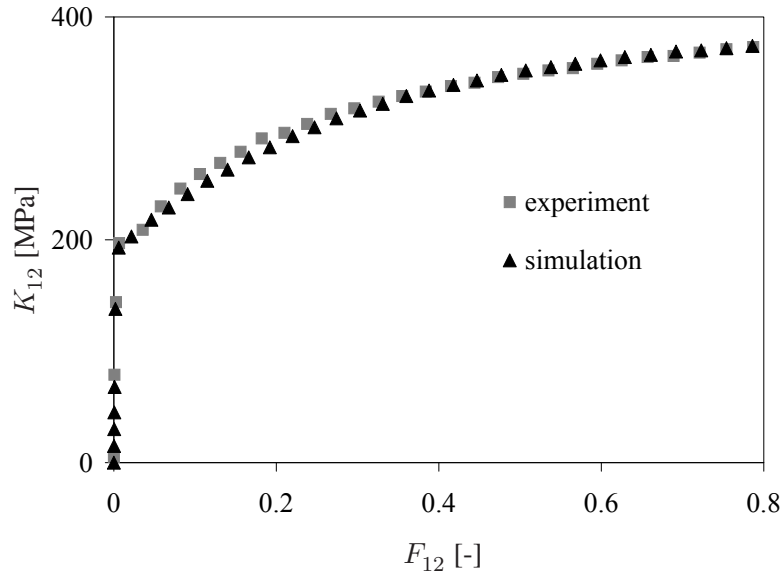


Figure 2.9: Comparison of the experimental monotonic simple-shear data with the corresponding identified model prediction.  $K_{12}$  represents the relevant shear component of the Kirchhoff stress.

practice of using the accumulated equivalent inelastic deformation  $\alpha_P$  for this purpose, which is a model quantity and therefore not experimentally-determined. Note that these parameterizations are not equivalent. This can also be seen from the fact that one obtains different model parameter values than those in Table 2.1 when using  $\alpha_P$  in this way. For example, in the combined isotropic-kinematic hardening case, one obtains  $c_r = 2.96$ ,  $s_r = 219.37$ ,  $c_x = 15.19$ ,  $s_x = 139.63$  instead of the values shown in Table 2.1 (right), as well as a poorer fit.

Before we proceed to the identification of the complete hardening model, it is instructive to compare the predictions of the identified standard combined (i.e., isotropic-kinematic) hardening model for orthogonal tension-shear loading with the corresponding test data as represented by path 1 in Figure 2.5. This is done in Figure 2.11. Not surprisingly, the model predicts no cross hardening. Optically, one might be tempted to identify the prediction of the identified combined isotropic-kinematic model with case 4 or 5 in Figure 2.5. Since these represent different paths in either strain or stress space, however, they are not directly comparable.

Consider lastly the identification of the isotropic-kinematic-cross (i.e., complete) hardening model. Again, this is done with the help of the identified parameter values for the isotropic-

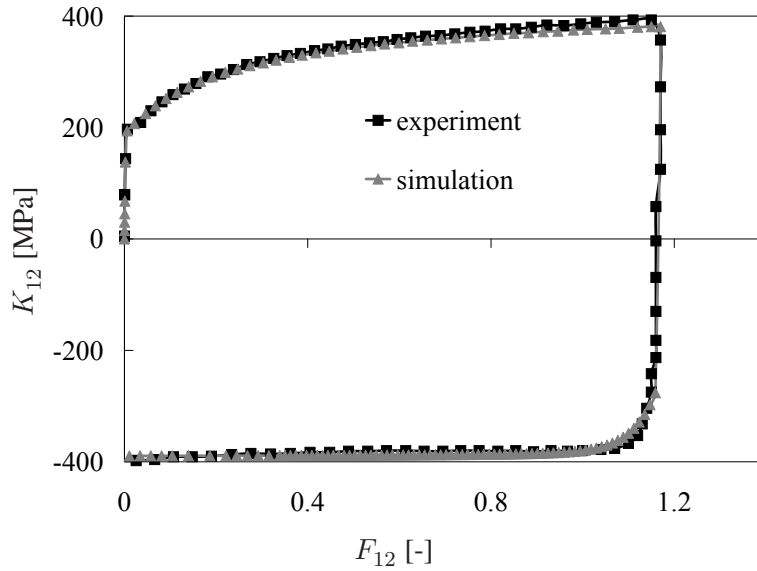


Figure 2.10: Comparison of the experimental cyclic simple-shear data with the corresponding identified combined isotropic-kinematic model prediction.

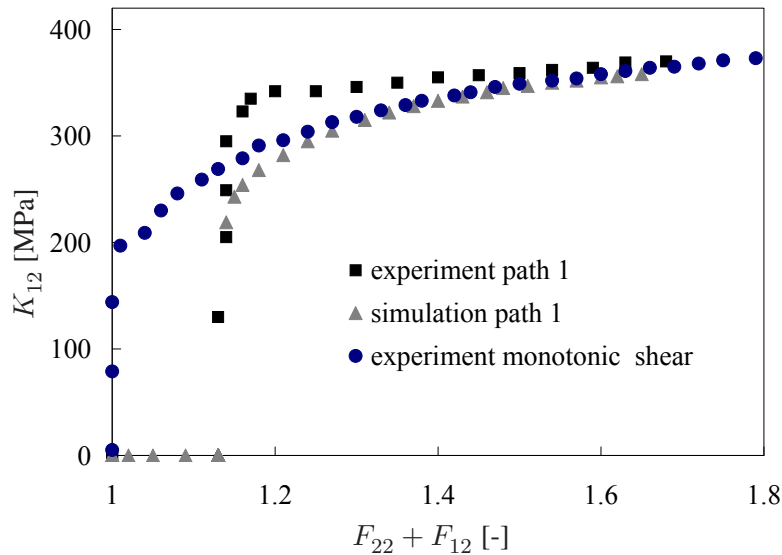


Figure 2.11: Comparison of the predictions of the identified standard combined (i.e., isotropic-kinematic) hardening model for forward simple shear and orthogonal tension-shear with corresponding experimental results from path 1 in Figure 2.5.

kinematic case as starting values. In this way, the complete model is fit to monotonic shear, cyclic shear and orthogonal tension-shear test data. In particular, the test data of path 1 in Figure 2.5 is added to the previous monotonic shear and cyclic shear data sets. As with  $c_r$  and  $c_x$ , the saturation rates  $c_d$  and  $c_l$  associated with cross hardening are constrained to be greater than zero in the fit. On the other hand, as with  $s_r$  and  $s_x$ ,  $s_d$  and  $s_l$  may be positive or negative. Since the values for  $s_d$  determined in this way were on the order of  $10^{-3}$ , this parameter was set to

|       | Value   | Units |
|-------|---------|-------|
| $s_r$ | 254.519 | MPa   |
| $c_r$ | 4.481   |       |
| $s_x$ | 90.896  | MPa   |
| $c_x$ | 32.695  |       |
| $s_d$ | 0.0     |       |
| $c_d$ | 19.712  |       |
| $s_l$ | -0.863  |       |
| $c_l$ | 5.0     |       |

Table 2.2: Identified hardening model parameter values for LH800 for isotropic-kinematic-cross hardening model parameter values determined from monotonic shear, cyclic shear, and orthogonal tension-shear, test data.

zero in the final fits, resulting in the parameter values for the complete model shown in Table 2.2. A comparison of the corresponding experimental data and model fit is shown in Figure 2.12. Parameters identification of current model for the steel DC06 can be found in Appendix A. As a first validation of the identified hardening model, this is used to simulate the behavior

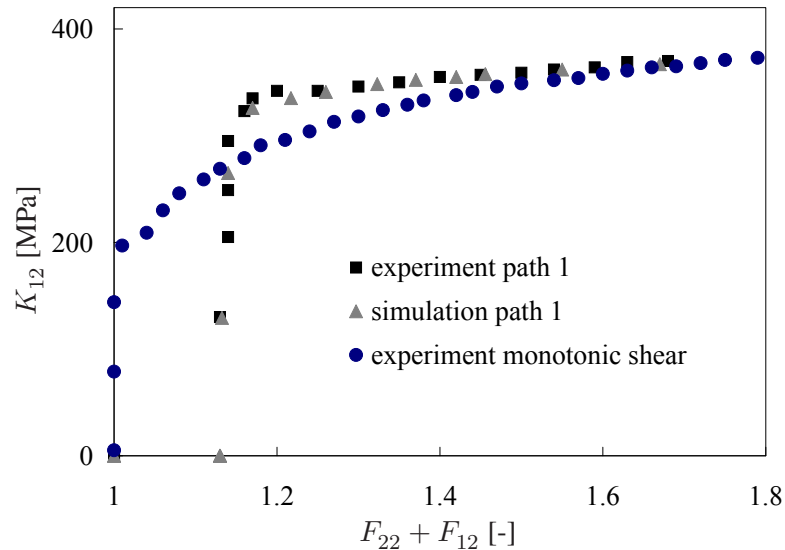


Figure 2.12: Comparison of identified isotropic-kinematic-cross hardening model behavior with experimental data for monotonic simple-shear and orthogonal tension-shear test data corresponding to strain path 1 in Figure 2.5.

of LH800 along the experimental strain paths 2 to 5 in Figure 2.5 not used in the identification procedure. The results of this are shown in Figure 2.13 and 2.14. Clearly, the agreement between experimental and simulation results is good. Beyond a realistic representation of complete isotropic-kinematic-cross hardening behavior, then, the current model is also capable of accounting for the dependence of cross hardening on the nature and details of the orthogonal transition from tension to shear. To investigate this further, we turn next to examine the implications of the model for yield surface and internal state development during monotonic shear,

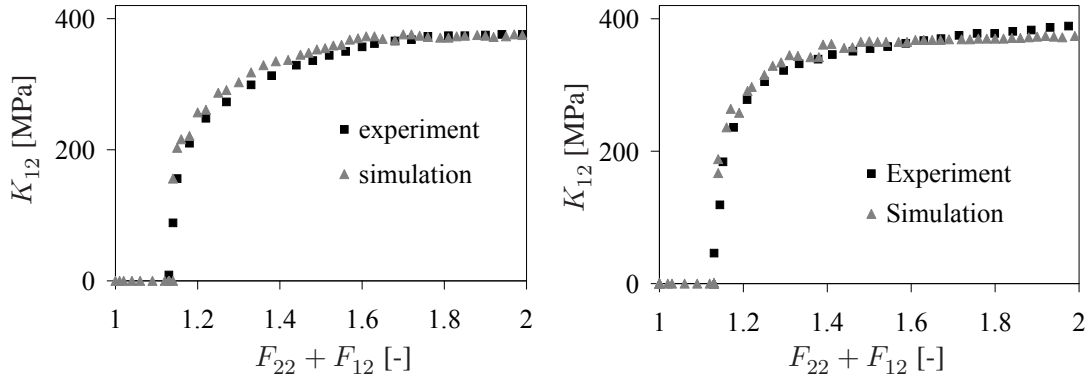


Figure 2.13: Comparison of the experimental results for strain paths 5 and 4 in Figure 2.5 with corresponding simulation results as based on the identified model for isotropic-kinematic-cross hardening. Right: path 4. Left: path 5.

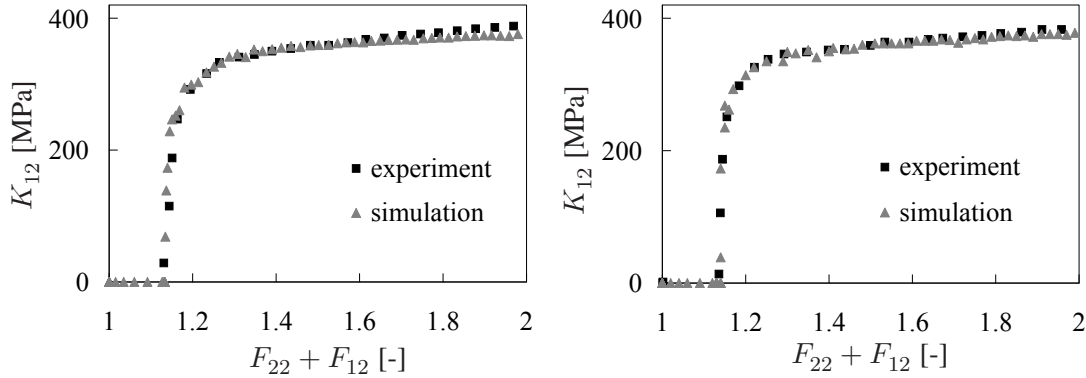


Figure 2.14: Comparison of the experimental results for strain paths 3 and 2 in Figure 2.5 with corresponding simulation results as based on the identified model for isotropic-kinematic-cross hardening. Right: path 2. Left: path 3.

cyclic shear and orthogonal tension-shear loading processes.

## 2.5 Yield surface evolution

Having established the ability of the current model to represent the development of combined isotropic-kinematic-cross hardening in LH800 during non-proportional loading, we now turn to a discussion of the evolution of the yield surface. To begin, consider the yield surface evolution for LH800 predicted by the identified model from the previous section. To this end, we look at the cases of (i) uniaxial tension, (ii) simple shear, (iii) plane-strain tension followed by simple shear and (iv) a continuous transition from plane-strain tension to simple shear. For representation purposes, we work with the normalized shear  $\bar{K}_{12} := \sqrt{3} K_{12} / \sigma_{Y0}$  and normal  $\bar{K}_{22} := K_{22} / \sigma_{Y0}$  stress components. For example, an isotropic yield surface in  $(\bar{K}_{12}, \bar{K}_{22})$ -space takes the form of the unit circle. The resulting yield surface evolution is shown in Figure 2.15. In addition to an increase in its size and a translation of its center, the current model clearly predicts a symmetric distortion of the yield surface. In particular, this latter takes the

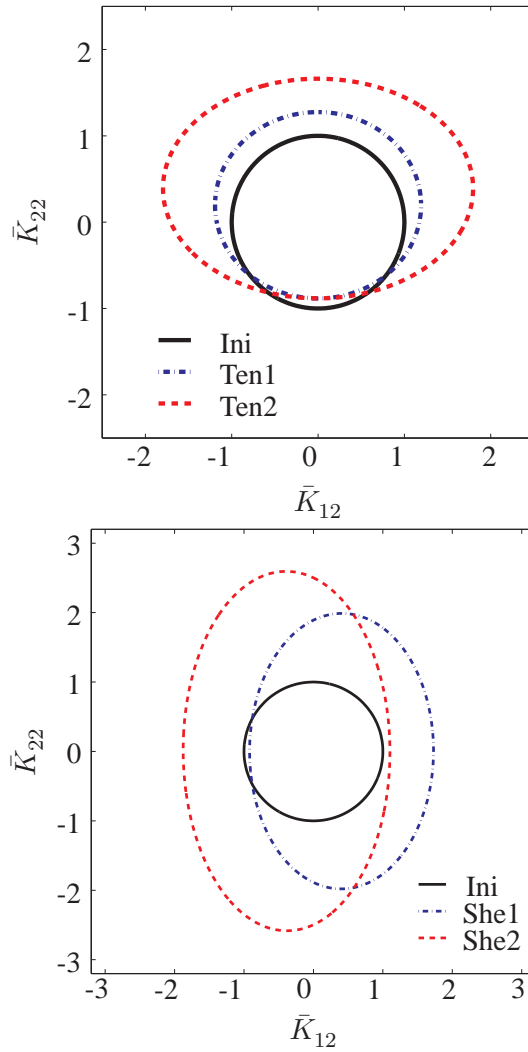


Figure 2.15: Yield surface evolution for LH800 during uniaxial tension (top) and simple shear (bottom). Shown here are the initial surface (Ini), an intermediate tension state (Ten1), the final tension state at  $F_{22} = 1.2$  (Ten2), the final forward shear state at  $F_{12} = 0.4$  (She1), and the final reverse shear state at  $F_{12} = 0.0$  (She2).

form of an elongation in the direction perpendicular to the current loading direction.

Consider next the case of an orthogonal loading path change from plane-strain tension to simple shear via intermediate unloading corresponding to the discontinuous path shown in Figure 2.7. The corresponding evolution of the yield surface is shown in Figure 2.16. During the tension phase (curve TenFin), the yield surface cross hardens as expected in the shear direction. After the shift from tension to shear, the yield surface shrinks continuously in the shear direction (curves TenShe1 to TenShe3) and elongates in the tension direction. This corresponds to cross hardening in the tension direction. Note that the shape of the yield surface at the end of the shear phase approaches that one attained in the monotonic shear test. This is in agreement with the observed experimental behavior for the discontinuous test. The stress state C attained in this case represents the point of maximum possible cross hardening, also in agreement with the experimental discontinuous and path 1 continuous (Figure 2.5 and 2.7) cases. On the other hand, the yield surface development for the continuous loading path 5 predicted by the current model

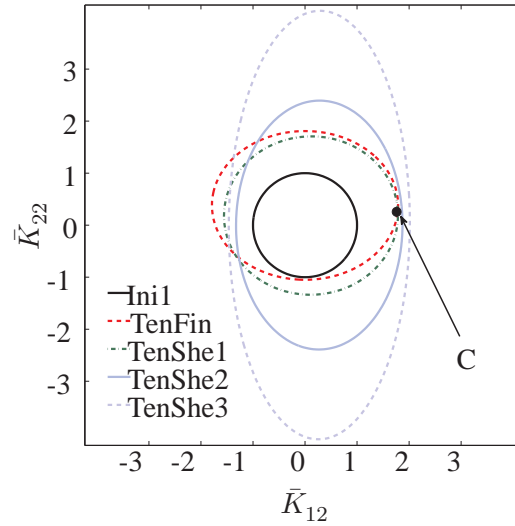


Figure 2.16: Predicted yield surface evolution for LH800 during orthogonal loading from plane-strain tension to simple-shear depicted in normalized stress space ( $\bar{K}_{12}$ ,  $\bar{K}_{22}$ ) for the discontinuous transition. Ini represents the initial yield surface. TenFin is the final tensile state. TenShe1 to TenShe3 represent subsequent yield surfaces during subsequent loading for the loading path also shown in Figure 2.5 and 2.7. The point C indicates the stress state obtained during the experiment and is the same point C as shown in Figure 2.8.

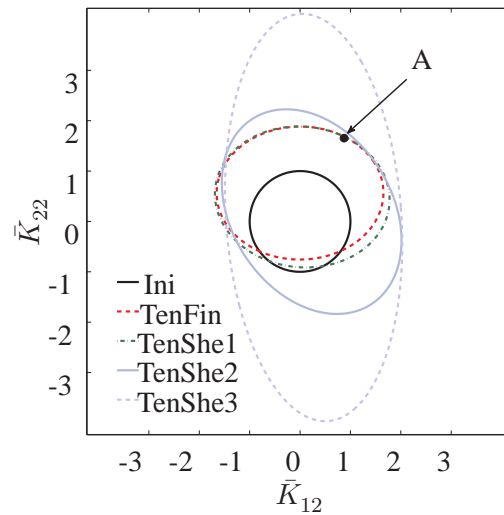


Figure 2.17: Predicted yield surface evolution for LH800 during orthogonal loading from plane-strain tension to simple-shear depicted in normalized stress space ( $\bar{K}_{12}$ ,  $\bar{K}_{22}$ ) for the continuous path 5. Ini represents the initial yield surface. TenFin is the final tensile state. TenShe1 to TenShe3 represent subsequent yield surfaces during subsequent loading for the loading path also shown in Figure 2.5. The point A indicates the stress state obtained during the experiment and is the same point A as shown in Figure 2.8.

(Figure 2.17) shows that the state A reached on this path results in little or no cross hardening. In both cases, the curves TenShe1 represent the yield surfaces predicted by the current model for equal  $F_{22} + F_{12}$ . Note also the nearly isotropic shape of the yield surface (curve TenShe2) obtained during the transition from shear to tension. Since a change in shape of the yield surface



is clearly associated with cross hardening here, it is reasonable to regard cross hardening as a special type of distortional hardening, at least in the context of the current model.

Having now examined the model yield surface evolution for LH800, we can take a closer look at the meaning of the values obtained for the saturation magnitudes  $s_d$  and  $s_l$  from Section 2.4 associated with cross hardening. Since isotropic, kinematic and cross hardening are decoupled in the current model, the special case of pure distortional hardening can be obtained by simply setting  $s_r$  and  $s_x$  to zero in the identified model. The resulting yield surface development for uniaxial tension to  $F_{22} = 1.2$  and for simple shear to  $F_{12} = 0.4$  in the case of pure distortional hardening are shown in Figure 2.18. These are the same deformation paths as in

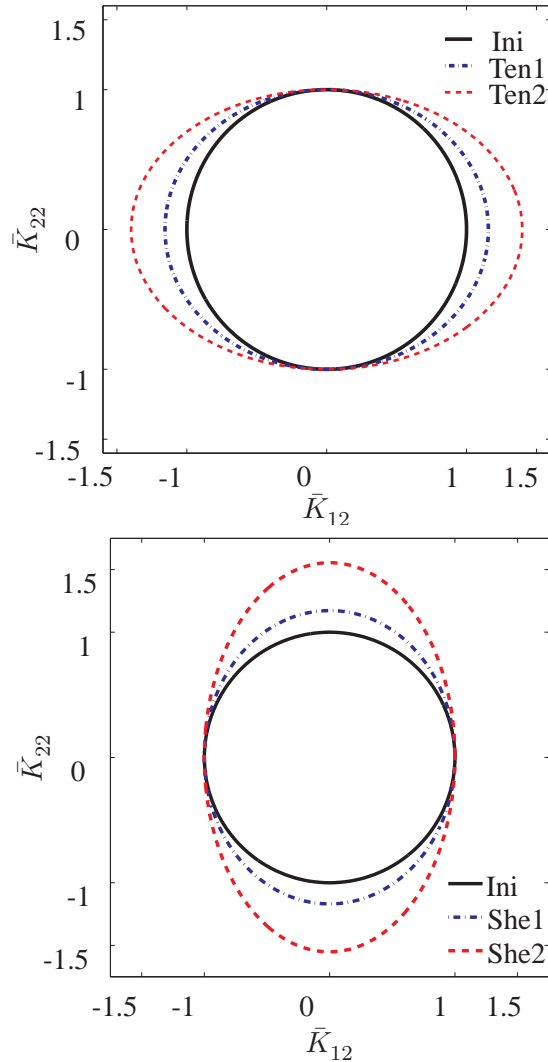


Figure 2.18: Yield surfaces development for LH800 during monotonic uniaxial tension (top) and simple shear (bottom) for pure cross hardening. Ini represents the initial yield surface. Ten1 is an intermediate tension stage. Ten2 represents the final tension stage for  $F_{22} = 1.2$ . She1 is an intermediate shear stage. She2 indicates the yield surface for  $F_{12} = 0.4$ .

Figure 2.15. As expected, pure distortional hardening leads to a pure shape change in the yield surface. This is due in particular to the fact  $s_d = 0$  in the fit. In addition, an increase in the yield level in directions orthogonal to the current direction follows for  $s_l < 0$ . These observations can be used in general with the current model as reasonable constraints on the model identification

in order to make this more efficient.

For comparison, consider the yield surfaces obtained by Ishikawa (1997) for the steel SUS304 subject to tension and torsion loading as depicted in Figure 2.19. For his tests, he used tubes

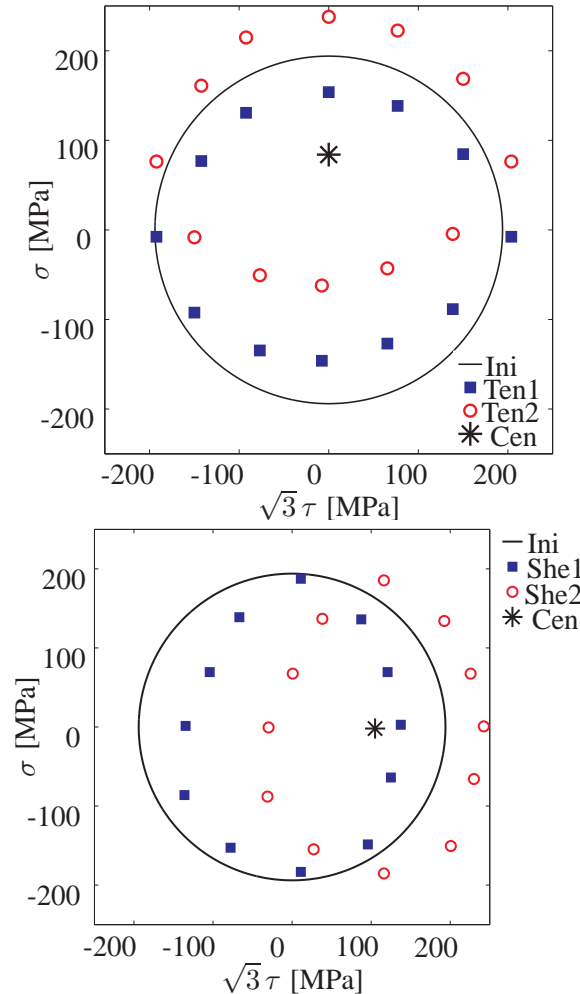


Figure 2.19: Yield surfaces after tension (top) and torsion (bottom) obtained by Ishikawa (1997) for SUS304. Ini represents the initial isotropic yield surface, Ten1 is the yield surface translated to the origin after tension, Ten2 is the yield surface after tension, She1 and She2 represent the translated and measured yield surfaces, respectively, after torsion. Cen marks the computed center of the subsequent yield surfaces.  $\tau$  and  $\sigma$  represent the relevant Cauchy shear and normal stresses, respectively.

milled from bulk SUS304. After milling, the tubes were annealed, and an average initial yield stress of 194 MPa was obtained using a  $50 \mu\text{m}/\text{m}$  definition. The initial yield surface depicted in Figure 2.19 was determined with the help of a least-square fit for 12 experimentally determined points on the yield surface. Subsequent yield surfaces were determined by applying a pre-stress. For the tension case depicted in Figure 2.19, the experimentally-determined Cauchy normal stress  $\sigma$  is 253 MPa, and the corresponding normalized shear stress  $\tau_{\text{Nor}} = \sqrt{3}\tau$  is -4 MPa. With the help of a model described in earlier work, Ishikawa (1997) then determined the centers of subsequent yield surfaces. In the case of torsion to an accumulated inelastic deformation of approximately  $10^{-3}$ , for example, values of 1 MPa for  $\sigma$  and of 284 MPa for  $\tau_{\text{Nor}}$  at the center of the yield surface were obtained in this way. Starting from these, he determined sub-

sequent yield surfaces via radial probing in stress space. As shown in Figure 2.19, subsequent yield surfaces determined in this fashion for SUS304 subject to tension and torsion loading are symmetrically distorted. For SUS304, this takes the form of a flattening of the yield surface in the direction of the applied stress. Note that there is neither noticeable isotropic hardening nor cross hardening in the sense of an increase in the yield stress in the orthogonal direction for SUS304 at the very small level of pre-strain involved ( $10^{-3}$ ). This is understandable from the point of view that, at this level of pre-strain, oriented dislocation microstructures responsible for cross hardening have not yet developed. In the case of the IF steel DC06, for example, noticeable cross-hardening occurs only after pre-straining up to approximately  $10^{-2}$ . As the experimental data presented in Section 2.3 and the above results shows, this is similar for the currently investigated steel LH800.

## 2.6 Inelastic state evolution

The previous section 2.5 focused on the predictions of the model for stress-strain behavior and yield surface evolution. In this section, attention is directed to the evolution of the internal variables. In contrast to stress-strain relations and the yield surface, internal variables cannot be measured experimentally. The interpretation of the evolution of these in the model context, however, is of interest here.

To begin, consider the development of  $\mathcal{A}$ . Again, recall that this quantity embodies the effect of oriented dislocation microstructure development on the effective flow anisotropy and yield surface form. Now, as discussed above, along the experimental paths in Figure 2.5, the material is subject to first tension in the 2 direction followed by shear in the 1 direction. Since  $s_d$  is constrained to be zero, the dominant evolution of  $\mathcal{A}$  is in the orthogonal (i.e., shear) direction during the tension phase. Indeed, with  $s_d = 0$ , (2.12) can be rewritten in the reduced form

$$\begin{aligned} \dot{\mathcal{A}} &= c_l s_l (\mathcal{I}_{\text{dev}} - \mathbf{N}_P \otimes \mathbf{N}_P) \dot{\alpha}_P \\ &- \{c_l \mathcal{A} + (c_d - c_l) (\mathbf{N}_P \cdot \mathcal{A} \mathbf{N}_P) \mathbf{N}_P \otimes \mathbf{N}_P\} \dot{\alpha}_P \end{aligned} \quad (2.14)$$

in which growth is in the direction  $\mathcal{I}_{\text{dev}} - \mathbf{N}_P \otimes \mathbf{N}_P$  “perpendicular” to  $\mathbf{N}_P \otimes \mathbf{N}_P$ . As such,  $a_d = \mathbf{N}_P \cdot \mathcal{A} \mathbf{N}_P$  remains zero during the tension phase, as shown in Figure 2.20. Consequently,  $\mathcal{A}_d$  does not influence the yield behavior of the material in the tension phase, but rather only after the orthogonal loading direction change into the shear phase. Indeed, as shown in Figure 2.20, upon change of loading direction from tension to shear, the projection of  $\mathcal{A}$  in the current (i.e., shear) loading direction, i.e.,  $a_d$ , is now non-zero and negative. Since  $s_l < 0$ , its magnitude decreases to zero with further loading in the shear direction (Figure 2.20). In turn, this results in a contraction of the yield surface in the shear direction. On the other hand, as shown in Figure 2.21,  $\mathcal{A}$ , and so  $\mathcal{A}_l$ , continue to evolve, resulting in an expansion of the yield surface in the tension direction during the shear loading phase. The amount of cross hardening is inversely correlated with the saturation level for  $|\mathcal{A}|$ . This correlation can also be established with respect to the development of kinematic hardening. Recall that the form  $\sqrt{(\mathbf{M} - \mathbf{X}) \cdot \mathcal{A} (\mathbf{M} - \mathbf{X})}$  of the equivalent stress measure appearing in the yield condition (2.8) depends on both  $\mathcal{A}$  and  $\mathbf{X}$ . In this sense, these quantities are related to each other, since they both influence the equivalent stress.

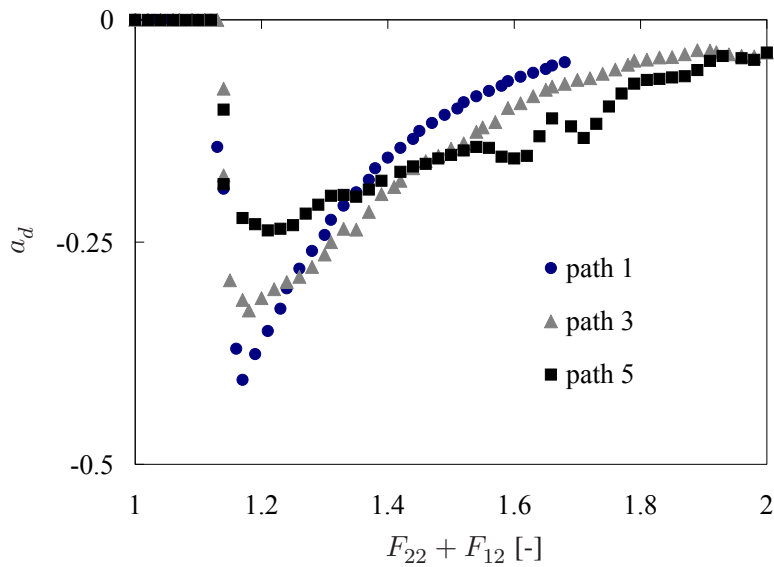


Figure 2.20: Evolution of  $a_d$  on paths 1, 3 and 5 in Figure 2.5. Note that  $|\mathcal{A}_d| = |a_d|$ .

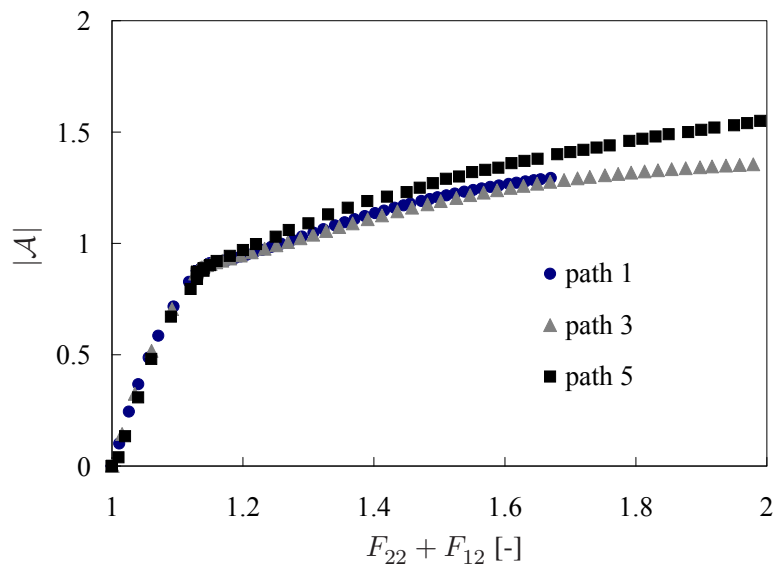


Figure 2.21: Development of  $|\mathcal{A}|$  on paths 1, 3 and 5 in Figure 2.5.

Consider next the evolution of the back stress along the paths 1, 3 and 5 in Figure 2.5 as displayed in Figure 2.22. As can be seen,  $|\mathbf{X}|$  increases during the tension stage, decreases at the start of shear stage, and then saturates. Note the nearly perfect correlation of the amount of decrease in  $|\mathbf{X}|$  with loading path upon change from tension to shear. In particular, the largest decrease occurs along strain path 1, representing the path with the least amount of tension loading. Analogously, the smallest decrease occurs along path 5 having the greatest amount of tension loading. To examine this result in more detail, consider the evolution of the relevant components of  $\mathbf{X}$ . For the tension phase, this is the  $X_{22}$ -component, and for the shear phase, the  $X_{12}$  component, of  $\mathbf{X}$ . The evolution of the former is shown in Figure 2.23. During the

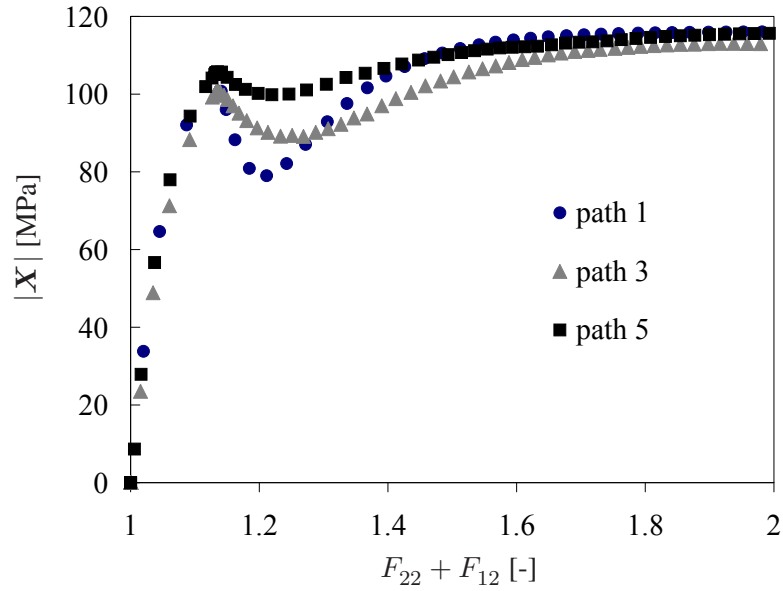


Figure 2.22: Evolution of  $|X|$  along paths 1, 3 and 5 in Figure 2.5.

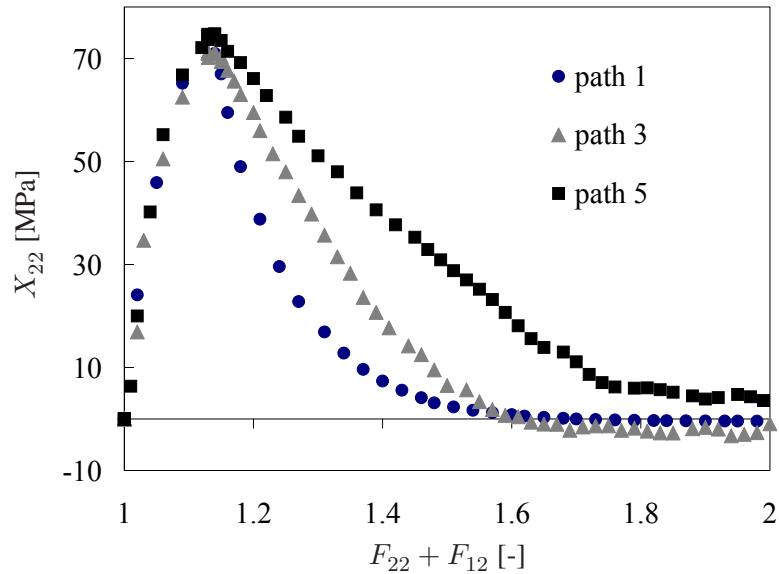


Figure 2.23: Development of  $X_{22}$  along paths 1, 3 and 5 in Figure 2.5.

common part of the tension stage,  $X_{22}$  develops in basically the same way for all experiments as expected. As exhibited by the results, this changes at the start of the transition from tension to shear. In all cases,  $X_{22}$  decreases. The largest decrease occurs in the case of path 1, for which the amount of tension is the smallest. On the other hand, the smallest decrease occurs for path 5 having the largest amount of tension. In all cases,  $X_{22}$  decreases basically to zero since the effective saturation value for this component of  $X$  goes to zero as  $N_{P_{22}}$  does. As shown by the results in Figure 2.24, during the shear phase, the development of  $X_{12}$  is the same for all paths, saturating in each case in essence to the monotonic value. From the point of view of the effective stress and so of the yield surface, then, we see that the decrease of  $X_{22}$  during the

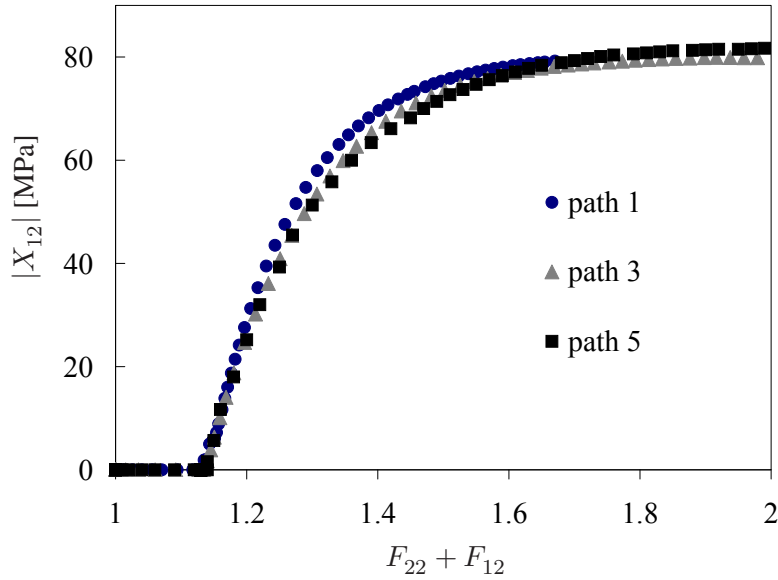


Figure 2.24: Evolution of  $X_{12}$  along paths 1, 3 and 5 in Figure 2.5.

transition from tension to shear in combination with the development of  $\mathcal{A}$  determines to what extent (if at all) a change in form of the yield surface occurs resulting in cross hardening, as shown in Figures 2.16, 2.17 and 2.18. In the case of the sharpest drop, i.e., path 1, having the “shortest” tension phase, this change is the largest. On the other hand, for the strain paths 4 and 5, having the longest tension phase, this change is the smallest. As already discussed above in the context of Figure 2.11, the superposition of the contributions of  $r$ ,  $\mathbf{X}$  and  $\mathcal{A}$  is decisive for the modeling of the anisotropic behavior.

## 2.7 Summary and conclusions

Motivated by experimental results, a material model for isotropic, kinematic and cross hardening has been formulated, identified and validated for the ferritic steel LH800. The novel aspect of the current approach is the form of the evolution relation for cross hardening, which represents a special type of distortional hardening. This process is modeled with the help of an evolution relation for the fourth-order anisotropic flow tensor  $\mathcal{A}$  of the saturation type. As such, this model is a special case of the class of models tacitly introduced by Baltov and Sawczuk (1965). Differences between the current and previous models (e.g., Dafalias et al. (2003); Feigenbaum and Dafalias (2007); Schick (2004)) for the evolution of this tensor include (i) no coupling between kinematic and distortional hardening, and (ii) the form of the evolution relation. As in the current case, the approach of Feigenbaum and Dafalias (2008) involves no coupling of the evolution of the back stress and  $\mathcal{A}_{\text{Bal}}$ . The focus in their case is on the asymmetric development of the yield surface rather than on the effect of cross hardening as in the current work. In contrast to all previous models, the form of the evolution relation for  $\mathcal{A}$  is determined by the split of  $\mathcal{A}$  into parts parallel  $\mathcal{A}_d$  and perpendicular  $\mathcal{A}_l$  to the current loading direction in stress space. This split is physically-motivated with the help of TEM investigations of the development of oriented dislocation microstructures (e.g., Nesterova et al. (2001)) directly related to

the history of the loading path direction and its changes. The form of the evolution relation for  $\mathcal{A}$  is formally analogous to that introduced by Wang et al. (2008) as based on the earlier work of Teodosiu and Hu (1998) for the fourth-order hardening tensor  $\mathcal{S}$  whose evolution accounts for the effect of cross hardening on the flow behavior. In contrast to the class of models based on the approach of Baltov and Sawczuk (1965), this tensor affects the current yield stress level rather than the effective stress level. As such, there is no change of shape of the yield surface associated with cross hardening in the class of models based on Teodosiu and Hu (1998); Wang et al. (2008). Unlike the Teodosiu and Hu (1998) model, the current model does not account for additional effects like hardening stagnation after load reversal. In work in progress, a more detailed comparison of the two classes of models is being carried out. In addition, a thermodynamically consistent framework for the current model analogous to that of Feigenbaum and Dafalias (2007); Schick (2004) represents on-going research and will be reported on in future work.





## Chapter 3

# Simplification and identification of a model for directional hardening

**Abstract**– In general, metal forming processes involve large strains and severe strain path changes. Large plastic strains in many metals lead to the development of persistent dislocation structures resulting in strong flow anisotropy. Teodosiu and Hu (1995, 1998) proposed a micro-mechanically motivated model which accounts for the effect of evolving persistent dislocation microstructures during loading-path changes on the hardening behavior via an evolving fourth-order structure tensor. The objective of this work is to propose a simplified formulation of the (Teodosiu and Hu, 1995, 1998) model. The full and simplified models are then characterized with the help of shear, reverse shear and tension-shear tests. The identified models have been validated by using them to predict the stress-strain behavior of the material along different tension-shear loading paths and by comparison with analogous experimental results.

### 3.1 Introduction

The focus of this work is to present a simplified formulation of the (Teodosiu and Hu, 1995, 1998) model. This model has been successfully applied to the simulation of sheet metal forming processes involving strain path changes (Oliveira et al., 2007; Wang et al., 2008, 2006). The simplification leads to a reduction of the coupling between different contributions of anisotropic hardening and a reduction in the number of parameters which have to be identified. The agreement of the mechanical responses predicted by the model with experimental test data and the full model is excellent.

Sheet metals, especially ferritic interstitial free steels, show transient behavior after changes in strain path. This behavior was investigated by a number of authors. Ghosh and Backofen (1973) were among the first to report transients in stress-strain relations for interstitial free steels for sequences of plane strain tension to uniaxial tension. They observed a distinct increase in stress after such a change in strain-path. Rauch and Schmitt (1989), Rauch and Thuillier (1993) and Thuillier and Rauch (1994) used pre-strained specimen in combination with simple shear tests to determine the effect of load reversal on the mechanical response and the evolution of the dislocation microstructure. Besides the distinct increase in stress after a change in strain-path they observed a strong Bauschinger effect. The Bauschinger effect describes the fact that, the magnitude of the yield stress after load reversal is lower compared to the yield stress at the same amount of equivalent deformation in a monotonic test. In the works of Nesterova et al. (2001); Rauch and Schmitt (1989); Rauch and Thuillier (1993); Thuillier and Rauch (1994), the macroscopically observable phenomena were related to the interactions in the dislocation

microstructure. The increase in yield stress after a strain path change referred to as cross-hardening was attributed to the interaction of dislocations associated with the first and second loading direction in two stage tests. Ferritic steels tend to form planar dislocation structures. The spatial arrangement of these planar structures can be correlated with macroscopic axes of straining. Transmission-electron-microscopic analyses show that these structures are aligned with the glide directions of highly active glide systems. After a change in strain path different sets of glide systems are activated and the previously formed dislocation arrangements act as obstacles to dislocation glide. On the macroscopic scale this is observed as cross-hardening. After a substantial amount of straining in the new direction has occurred, the dislocation structures associated with the new loading direction become dominant. On the macroscopic scale this leads to the fact that with progressing straining after the change in strain path, the stress-strain curves of the monotonic and non-monotonic tests become coincident.

Teodosiu and Hu (1995) proposed a micro-mechanically motivated model which accounts for cross-hardening, the Bauschinger effect and hardening stagnation. In their model the evolution of internal variables can be closely linked to the microstructural mechanisms inducing the transient mechanical response. The model introduces strong coupling between different contributions to anisotropic hardening. Central to the model is the introduction of a fourth-order tensor accounting for the interaction of dislocation structures during loading path changes. The effective yield stress depends on (the magnitude of) this fourth-order evolving structure tensor, therefore, we called here this model as yield stress model. The model is capable of accounting for isotropic, kinematic and directional hardening. For the full model, 22 parameters governing the plastic behavior need to be identified. In general, this is done by inverse analysis with the aim to fit simulated material responses to experimentally determined stress strain curves. This can become a complex task by itself as is demonstrated by Haddadi et al. (2006) and also reviewed in this work. The reduction of the level of coupling between the different hardening contributions and the reduction of parameters are desirable for different reasons.

Strong coupling implies the use of more elaborate integration algorithms or small time steps in order to secure stability of the material algorithm. In addition, the time required for parameter identification increases with the number of parameters. This work presents a simplified version of the modified Teodosiu model (Wang et al., 2008) which captures the characteristic transient effects observed in experiments to a large extent. The modified Teodosiu model proposed by Wang et al. (2008) is reviewed. The simplifications reducing the number of parameters to 17 and decoupling isotropic, kinematic and directional hardening are presented. The full yield stress and simplified yield stress models are identified on the basis of monotonic shear, reverse shear and tension-shear tests for ferritic steel LH800. Finally, the model behavior for the full and simplified models is compared and discussed.

## 3.2 Model formulation

### 3.2.1 Framework

The formulation of the current models is carried out in the framework of the standard inelastic multiplicative decomposition  $\mathbf{F} = \mathbf{F}_E \mathbf{F}_P$  of the deformation gradient  $\mathbf{F}$  (e.g., Lee, 1969). Such a decomposition arises naturally, e.g., in the context of the modeling of  $\mathbf{F}_P$  as a change of local

reference configuration (Svendsen, 2001). In this context, one obtains in particular the result

$$\mathbf{R}_E^T \mathbf{L}_E \mathbf{R}_E = \mathbf{R}_E^T \mathbf{L} \mathbf{R}_E - \mathbf{U}_E \mathbf{L}_P \mathbf{U}_E^{-1} = \mathbf{R}_E^T \dot{\mathbf{R}}_E + \dot{\mathbf{U}}_E \mathbf{U}_E^{-1} \quad (3.1)$$

via the right polar decomposition  $\mathbf{F}_E = \mathbf{R}_E \mathbf{U}_E$  of  $\mathbf{F}_E$  for the back-rotated form of  $\mathbf{L}_E := \dot{\mathbf{F}}_E \mathbf{F}_E^{-1}$  in terms of  $\mathbf{L} := \dot{\mathbf{F}} \mathbf{F}^{-1}$  and  $\mathbf{L}_P := \dot{\mathbf{F}}_P \mathbf{F}_P^{-1}$ . For the current case of polycrystalline metals and small elastic strain, the approximations

$$\begin{aligned} \mathbf{U}_E &\approx \mathbf{I} + \ln \mathbf{U}_E, \\ \dot{\mathbf{U}}_E \mathbf{U}_E^{-1} &\approx \overline{\ln \dot{\mathbf{U}}_E}, \end{aligned} \quad (3.2)$$

hold. Substituting these into (3.1), and taking the symmetric and skew-symmetric parts of the result, the evolution relations

$$\begin{aligned} \overline{\ln \dot{\mathbf{U}}_E} &= \mathbf{R}_E^T \mathbf{D} \mathbf{R}_E - \mathbf{D}_P, \\ \dot{\mathbf{R}}_E &= \mathbf{W} \mathbf{R}_E - \mathbf{R}_E \mathbf{W}_P, \end{aligned} \quad (3.3)$$

are obtained for  $\ln \mathbf{U}_E$  and  $\mathbf{R}_E$ , respectively, in the incremental context. Here,  $\mathbf{D} = \text{sym}(\mathbf{L})$  is the continuum rate of deformation,  $\mathbf{D}_P = \text{sym}(\mathbf{L}_P)$  its inelastic counterpart,  $\mathbf{W} = \text{skw}(\mathbf{L})$  the continuum spin, and  $\mathbf{W}_P = \text{skw}(\mathbf{L}_P)$  the plastic spin. Restricting the current formulation to the case of sheet metal forming, it is reasonable to assume that the texture in these materials achieved during rolling remains largely unchanged during forming processes like tension, compression, simple shear, cyclic simple shear, and combinations of these. In this case, the plastic spin  $\mathbf{W}_P$  is negligible, and the evolution of  $\mathbf{R}_E$  depends only on the spin  $\mathbf{W}$ . In this case it reduces to a purely kinematic quantity (i.e., the Jaumann rotation). In addition, focusing in this work on the material behavior of sheet metal during forming below the forming limit, we assume for simplicity that damage or any other process resulting in inelastic volume changes is negligible. In this case, plastic incompressibility  $\det(\mathbf{F}_P) = 1$  pertains, implying  $\text{tr}(\mathbf{D}_P) = 0$  in the incremental context. In this case,  $\mathbf{D}_P$  is equal to its deviatoric part  $\mathbf{D}'_P$ .

Since the elastic range and elastic strain are small, any elastic anisotropy arising from rolling is assumed negligible here. In this case, the isotropic form

$$\mathbf{M} = \kappa \text{tr}(\mathbf{E}_E) \mathbf{I} + 2 \mu \mathbf{E}'_E \quad (3.4)$$

is assumed for the Mandel stress  $\mathbf{M}$  in terms of the elastic strain  $\mathbf{E}_E = \ln \mathbf{U}_E$ , bulk modulus  $\kappa$ , shear modulus  $\mu$ , and deviatoric part  $\mathbf{E}'_E$  of  $\mathbf{E}_E$ . Lastly, again in the framework of small elastic strain,  $\mathbf{M}$  and  $\mathbf{R}_E$  determine the Kirchhoff  $\mathbf{K}$ , and so the Cauchy  $\mathbf{T} = \mathbf{K} / \det(\mathbf{F})$ , stress via

$$\mathbf{K} = \mathbf{R}_E \mathbf{M} \mathbf{R}_E^T. \quad (3.5)$$

Consequently, in contrast to  $\mathbf{K}' = \mathbf{R}_E \mathbf{M}' \mathbf{R}_E^T$ ,  $\text{tr}(\mathbf{K}) = \text{tr}(\mathbf{M})$  of  $\mathbf{K}$  is independent of  $\mathbf{R}_E$ .

Consider next the modeling of isotropic and kinematic hardening. Let  $r$  represent the contribution of isotropic hardening to the effective yield stress of the model, and  $\mathbf{X}$  the back stress as usual. For the class of materials under consideration, the standard saturation-based forms

$$\begin{aligned} \dot{r} &= c_r (s_r - r) \dot{\alpha}_P, \\ \dot{\mathbf{X}} &= c_x (s_x \mathbf{N}_P - \mathbf{X}) \dot{\alpha}_P, \end{aligned} \quad (3.6)$$

for the evolution of these quantities are relevant. Both are driven by the evolution of the equivalent inelastic deformation  $\alpha_P$ . Here,  $c_r$  and  $c_x$  represent the rates, and  $s_r$  and  $s_x$  the saturation values, associated with  $r$  and  $\mathbf{X}$ , with  $\mathbf{N}_P = \mathbf{D}_P/|\mathbf{D}_P|$  the direction of the rate of inelastic deformation. In what follows, we also work with the fourth-order tensor  $\mathcal{N}_P = \mathbf{N}_P \otimes \mathbf{N}_P$  determined by  $\mathbf{N}_P$ . As usual,  $\mathbf{D}_P$  is given by the associated flow rule

$$\mathbf{D}_P = \dot{\alpha}_P \partial_{\mathbf{M}-\mathbf{X}} \phi. \quad (3.7)$$

Finally, in the current rate-independent context,  $\alpha_P$  is determined as usual by the ‘‘consistency’’ condition  $\dot{\phi} = 0$ .

### 3.2.2 Yield stress model

As discussed in the introduction, the yield stress model accounts for the effect of evolving oriented dislocation microstructures during loading-path changes on the hardening behavior via an evolving fourth-order structure tensor  $\mathcal{S}$ . In particular, the magnitude of this tensor determines the effective yield stress of the material via the form

$$\phi(\mathbf{M}, r, \mathbf{X}, \mathcal{S}) = \sqrt{(\mathbf{M} - \mathbf{X}) \cdot \mathcal{A}_0 (\mathbf{M} - \mathbf{X})} - \sigma_{Y0} - r - f |\mathcal{S}| \quad (3.8)$$

of the yield function due to Teodosiu and Hu (1995, 1998).  $\mathcal{A}_0$  represents the fourth-order symmetric traceless constant flow anisotropy tensor,  $\sigma_{Y0}$  is the initial yield stress, and  $f$  is a material constant determining the fraction of the dislocation walls strength contributing to isotropic hardening.

In contrast to the approach of Teodosiu and Hu (1998), the current form (a slight generalization of that of Wang et al., 2008) is based on the modeling of  $\mathcal{S}$  as a standard internal variable with constitutive relation

$$\begin{aligned} \dot{\mathcal{S}} &= c_d (h_p + h_x) \left\{ \frac{h_p}{h_p + h_x} s_s \mathcal{N}_P - \mathcal{S}_d \right\} \dot{\alpha}_P \\ &+ c_l |\mathcal{S}_l/s_s|^{n_l} \{s_l (\mathcal{I}_{\text{dev}} - \mathcal{N}_P) - \mathcal{S}_l\} \dot{\alpha}_P \end{aligned} \quad (3.9)$$

in the back-rotated frame. Here,  $\mathcal{I}_{\text{dev}} = \mathcal{I} - \frac{1}{3} \mathbf{I} \otimes \mathbf{I}$  is the fourth-order deviatoric identity,  $\mathcal{S}_d$  represents the strength of the dislocation structures associated with the currently active slip systems, and  $\mathcal{S}_l = \mathcal{S} - \mathcal{S}_d$  is that of the dislocation structures associated with the latent slip systems. The material function  $c_d (h_p + h_x)$  determines the effective saturation rate, and that  $h_p s_s / (h_p + h_x)$  the effective saturation magnitude, associated with  $\mathcal{S}_d$ . By analogy,  $c_l |\mathcal{S}_l/s_s|^{n_l}$  is the effective saturation rate, and  $s_l$  represents the corresponding saturation magnitude, associated with  $\mathcal{S}_l$ . These quantities contain the material constants  $c_d$ ,  $c_l$ ,  $s_s$ ,  $s_l$  and  $n_l$ . Setting  $s_l = 0$  reduces (3.9) to the form in (Wang et al., 2008).  $h_p$  represents a further material function depending on  $\mathcal{S}_d$ ,  $\mathbf{N}_P$ , a further material constant  $n_p$ , and the symmetric traceless second-order tensor-valued internal variable  $\mathbf{P}$  with evolution constitutive relation

$$\dot{\mathbf{P}} = c_p (\mathbf{N}_P - \mathbf{P}) \dot{\alpha}_P \quad (3.10)$$

which accounts for the effect of dislocation polarization on cross hardening (see, e.g., Teodosiu and Hu, 1998; Wang et al., 2008).  $c_p$  is the corresponding saturation rate. The effect of hardening stagnation after load reversal is accounted for via material function  $h_x$  depending on  $\mathbf{N}_P$ ,

$\mathbf{X}$ , and

$$\mathbf{A} = (\mathbf{M} - \mathbf{X}) / \sqrt{(\mathbf{M} - \mathbf{X}) \cdot \mathcal{A}_0 (\mathbf{M} - \mathbf{X})} \quad (3.11)$$

(again, see, e.g., Teodosiu and Hu, 1998; Wang et al., 2008). Lastly, the saturation magnitude  $s_x$  of  $\mathbf{X}$  is given by the constitutive relation

$$s_x = x_0 + (1 - f) \sqrt{|\mathcal{S}_d|^2 + m |\mathcal{S}_l|^2} \quad (3.12)$$

depending on the directional strength of the dislocation microstructure. Here,  $x_0$  represents the initial value of  $s_x$ . The parameter  $m$  determines the influence of latent as opposed to current dislocation structures on the saturation magnitude  $s_x$  of  $\mathbf{X}$ .

### 3.2.3 Simplified yield stress model

As discussed in the last sub-section, in addition to isotropic, kinematic, and cross hardening, the (full) yield stress model accounts for additional processes like dislocation polarization or hardening stagnation after load reversal. The (full) yield stress model can be reduced (i) by decoupling kinematic and directional hardening and (ii) reducing the number of internal variables. This implies that hardening stagnation can not be captured accurately by the simplified model. Hardening stagnation refers to a regime of very low work-hardening after a change in strain path. Hardening stagnation can be observed after orthogonal strain path changes or load reversal. Especially dual phase steels show distinct hardening stagnation after load reversals (Bouvier et al., 2006; Haddadi et al., 2006). In ferritic steels LH800 the effect is rather small for moderate amount of straining. Thus the omission of this contribution is justified. To eliminate the effect of dislocation polarization, for example, set  $c_p = 0$ , This yields  $\mathbf{P} \equiv \mathbf{0}$  and so  $h_p = 1$  independent of the value of  $n_p$ , which is then superfluous. Further, set  $h_x \equiv 0$  and  $n_l = 0$ . Then

$$\dot{\mathcal{S}} = c_d (s_s \mathcal{N}_P - \mathcal{S}_d) \dot{\alpha}_P + c_l \{s_l (\mathcal{I}_{\text{dev}} - \mathcal{N}_P) - \mathcal{S}_l\} \dot{\alpha}_P \quad (3.13)$$

follows from (3.9). Assume further  $f = 1$ . This decouples  $\mathbf{X}$  and  $\mathcal{S}$ , i.e.,  $s_x = x_0$  follows from (3.12) independent of the value of  $m$ , which then is superfluous. In addition,

$$\phi(\mathbf{M}, r, \mathbf{X}, \mathcal{S}) = \sqrt{(\mathbf{M} - \mathbf{X}) \cdot \mathcal{A}_0 (\mathbf{M} - \mathbf{X})} - \sigma_{Y0} - r - |\mathcal{S}| \quad (3.14)$$

follows from (3.14) for the yield function.

The full yield stress model discussed above contains 22 material parameters. These include the elastic bulk  $\kappa$  and shear  $\mu$  moduli, the initial yield stress  $\sigma_{Y0}$ , the six parameters  $F$ ,  $G$ ,  $H$ ,  $L$ ,  $M$ , and  $N$  determining the initial flow anisotropy tensor  $\mathcal{A}_0$ , the five saturation rates  $c_r$ ,  $c_x$ ,  $c_d$ ,  $c_l$  and  $c_p$ , the three saturation values  $s_r$ ,  $x_0$ ,  $s_s$  and  $s_l$ , the two exponents  $n_l$  and  $n_p$ , as well as  $f$  and  $m$ . Since  $c_p$ ,  $n_p$ ,  $n_l$ ,  $f$ , and  $m$  are either specified or eliminated in deriving the reduced yield stress model as based on (3.13) and (3.14), this depends on only 17 of the 22 material parameters of the full model:  $\kappa$ ,  $\mu$ ,  $\sigma_{Y0}$ ,  $F$ ,  $G$ ,  $H$ ,  $L$ ,  $M$ ,  $N$ ,  $c_r$ ,  $c_x$ ,  $c_d$ ,  $c_l$ ,  $s_r$ ,  $x_0$ ,  $s_s$ , and  $s_l$ .

## 3.3 Material testing

For the experimental work a biaxial testing equipment developed at the University of Twente, the Netherlands, was used to subject specimen shown in Figure 3.1. The equipment is capable

of loading a sheet metal specimen in both simple shear and in plane-strain tension. Using this device, one can carry out single- or multi-stage loading programs consisting of monotonic (e.g., forward simple-shear), reverse (e.g., forward-reverse simple-shear), and / or orthogonal (e.g., tension-shear) changes of loading direction. In particular, the latter can be carried out with or without unloading of the specimen upon change of loading direction.

### 3.3.1 Test setup

The biaxial testing equipment consists of a regular uniaxial testing device which via an actuator is used to achieve plane-strain tension in the sample. A subframe mounted between the cross bars accommodates the actuator for simple shear deformation. The deformation is applied to the sample as indicated in Figure 3.1. Further details concerning the experimental setup and procedure can be found in Noman et al. (2010).

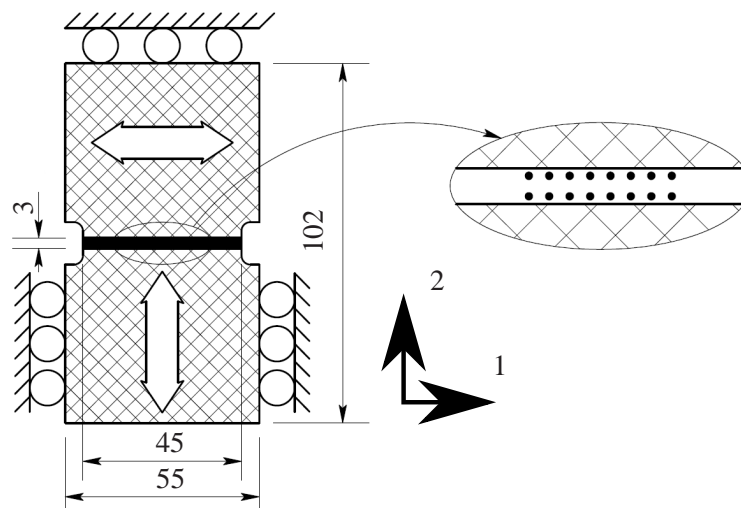


Figure 3.1: Biaxial test setup. Geometry of the tension-shear specimen and the measurement region of height 3.0mm and width 45.0 mm. The checkered region indicates the actual specimen and the black area marks the actual deformation zone. The tension direction is direction 2 and the shear direction is direction 1.

### 3.3.2 Test results

For the current work, tests performed on specimens of the ferritic steel LH800 include (i) monotonic plane-strain tension at different strain-rates, (ii) reverse simple-shear for different amounts of forward pre-shear, and (iii) orthogonal tension-shear with and without unloading. All tests were performed with the tension direction oriented in the rolling direction. Figure 3.2 shows the results of 2 reverse simple-shear tests. The material exhibits early re-yielding after load reversal, followed by a period of work hardening stagnation as can be seen in Figure 3.2. Lastly, consider the results from the orthogonal tests. As stated above, these consist of plane-strain tension followed by simple shear loading. The transition from tension to simple shear is either discontinuous via intermediate unloading, or continuous without unloading. The data so obtained include the 5 different continuous loading paths (numbered 1 to 5) shown in Figures 3.3 and 3.4.

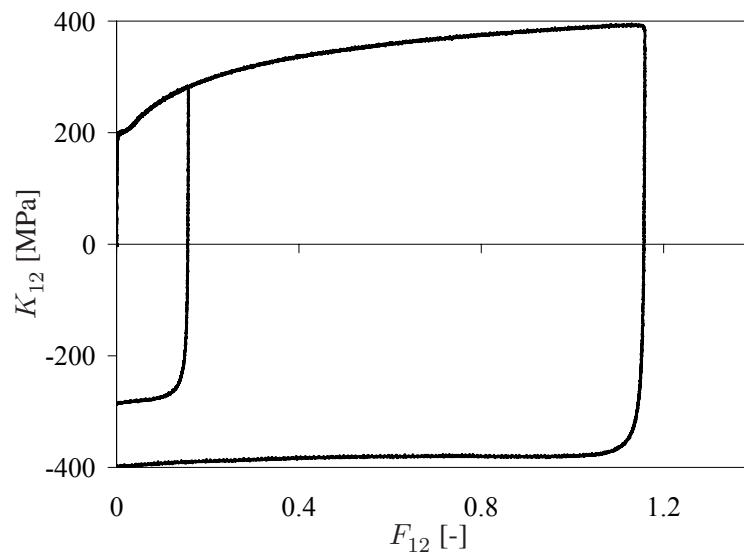


Figure 3.2: Reverse shear test results for LH800 for two different levels (i.e., 0.1 and 0.65) of pre-shear. All stress results are shown in absolute value form.

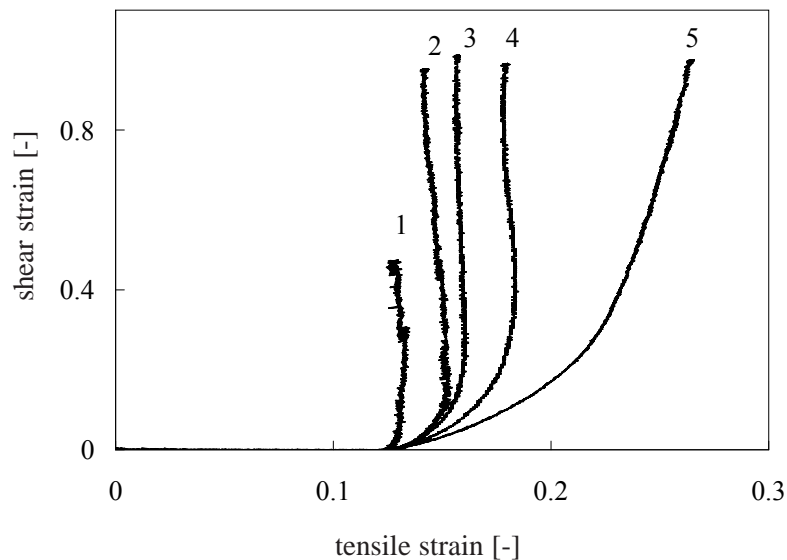


Figure 3.3: Experimental strain paths in LH800 resulting from continuous change of loading direction from tension to shear.

Consistent with existing interpretations of such data in the literature, the presence or absence of cross hardening in such orthogonal tests is judged solely by comparison with the monotonic simple shear results. In particular, any overshoot of the yield stress above the monotonic level upon transition from tension to shear is an indicator of such hardening. Using this “definition,” curves 1, 2 and 3 in Figure 3.3 clearly exhibit cross hardening as can be seen in Figure 3.4, curve 4 might exhibit a little, and curve 5 clearly none at all. For the detailed discussion of the results the reader is referred to Noman et al. (2010).

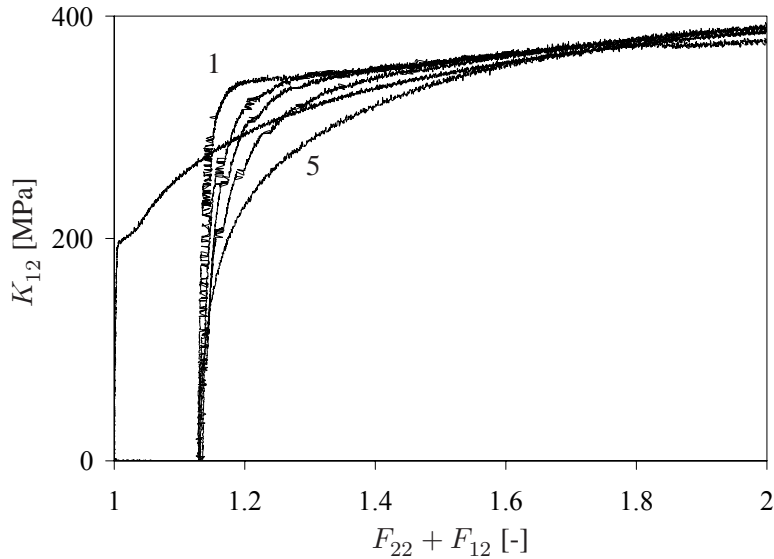


Figure 3.4: Stress response of LH800 for monotonic forward simple shear (curve starting at  $F_{22} + F_{12} = 1$ ) and for the 5 different orthogonal tension-shear paths shown in Figure 3.3.

### 3.4 Identification of material models

The material parameter determination is carried out using the program LS-OPT in conjunction with LS-DYNA. Given the homogeneous nature of the tests, one-element calculations suffice. The optimization technique used relies on response surface methodology (RSM) (Stander et al. (2008)). Other methods have been used by previous workers (e.g., Flores et al. (2007); Haddadi et al. (2006)) to identify related models like the Teodosiu model. All fits to follow are based on the fixed values  $\kappa = 167.05$  GPa and  $\mu = 77.09$  GPa for the elastic properties, as well as  $\sigma_{Y0} = 330.79$  MPa for the initial yield stress, of LH800, all at room temperature. Tensile tests performed on LH800 at  $0^\circ$ ,  $45^\circ$ ,  $90^\circ$  with respect to the rolling direction yielded no distinct initial orthotropy and so Hill parameter values of  $F = G = H = 0.5$  and  $L = M = N = 1.5$ .

#### 3.4.1 Identification of the full yield stress model

Since the internal variables  $r$ ,  $\mathbf{X}$ ,  $\mathbf{P}$ ,  $\mathcal{S}$  are coupled in the full yield stress model and there exist 22 material parameters in the yield stress based model, the identification procedure is tedious and more complicated than for the material model presented in Noman et al. (2010). The strategy here is also to identify successively different subsets of the complete set of material parameters with specific test data. In a final global run, all parameters can be varied in order to minimize a global cost function containing experimental data from all considered tests. Haddadi et al. (2006) presented a detailed analysis of the identification procedure using the software SiDoLo for various materials for the Teodosiu model. Differing from the procedure suggested in Haddadi et al. (2006) no special weight is given to specific regions of the stress-strain curves in order to improve the quality of the fit. Even though the author acknowledges that the effects of the variation in certain parameters are localized, in the current work the only weights introduced to the cost function account for the fact that different tests represent different levels



of deformation. Here the constant weight of a single test is dependent of  $F_{\text{Tot}} = \int_0^T |\dot{\mathbf{F}}| dt$ . Also differing from Haddadi et al. (2006) only stress vs. deformation curves as can be seen from Figures 3.2 - 3.4 were used. As already mentioned in Noman et al. (2010) the use of components of the deformation gradient instead of the accumulated plastic strain  $\alpha_P$  leads to an improvement of the fit for both models especially in the elbow area in the cyclic tests. The parameters  $s_r$ ,  $c_r$ ,  $s_s$ ,  $c_d$ ,  $n_p$ ,  $c_p$ ,  $f$ ,  $x_0$  and  $c_x$  are determined from monotonic and cyclic shear tests. The identified set of parameters is presented in Table 3.1.

| Parameter        | value   | units |
|------------------|---------|-------|
| $x_0$            | 70.785  | MPa   |
| $s_r$            | 155.21  | MPa   |
| $s_{\text{sat}}$ | 107.984 | MPa   |

| Parameter | value  |
|-----------|--------|
| $c_p$     | 44.9   |
| $c_x$     | 44.561 |
| $c_d$     | 9.865  |
| $c_r$     | 5.097  |
| $f$       | 0.452  |
| $n_p$     | 196.09 |

Table 3.1: Material parameter values for LH 800 using only cyclic shear data.

Keeping these identified parameters constant, the parameters  $c_l$ ,  $n_l$ ,  $s_l$  and  $m$  are then determined from the tension-shear test data of strain path 1 presented in Figure 3.3. This procedure yields the values of these parameters as  $c_l = 49$ ,  $n_l = 0.968$ ,  $s_l = 0.0$  and  $m = 42.453$ . In the final run, using the monotonic and cyclic shear test and tension-shear test data of strain path 1 presented in Figure 3.3 with a variation of all parameters the identification is performed. In this way the complete yield stress based model is identified and the parameters for the complete model can be seen in Table 3.2. A comparison of the corresponding experimental cyclic shear data and tension-shear data of strain path 1 presented in Figure 3.3 with numerical fit is shown in Figure 3.5 and Figure 3.6. Parameter identification of full yield stress model for the steel DC06 can be found in Appendix A.

| Parameter     | value  | units |
|---------------|--------|-------|
| $\kappa$      | 167050 | MPa   |
| $\mu$         | 77097  | MPa   |
| $\sigma_{Y0}$ | 330.79 | MPa   |
| $x_0$         | 13.89  | MPa   |
| $s_r$         | 74.43  | MPa   |
| $s_s$         | 243.76 | MPa   |
| $s_l$         | 0.0    | MPa   |

| Parameter | value   |
|-----------|---------|
| $c_p$     | 18.8956 |
| $c_x$     | 138.376 |
| $c_d$     | 11.08   |
| $c_l$     | 2.752   |
| $c_r$     | 1.459   |

| Parameter | value  |
|-----------|--------|
| $m$       | 1.973  |
| $f$       | 0.105  |
| $n_l$     | 0.0    |
| $n_p$     | 199.96 |

Table 3.2: Identified parameters of the full yield stress model for LH 800.

As a first validation of the identified hardening model, this is used to simulate the behavior of LH800 along the experimental strain paths 2 to 5 in Figure 3.3 not used in the identification procedure. The results of this are shown in Figure 3.7 and 3.8. The good agreement between the numerical prediction of yield stress based model and the experiments emphasize the fact that, besides capturing of cross hardening, this model is also capable of accounting for the de-

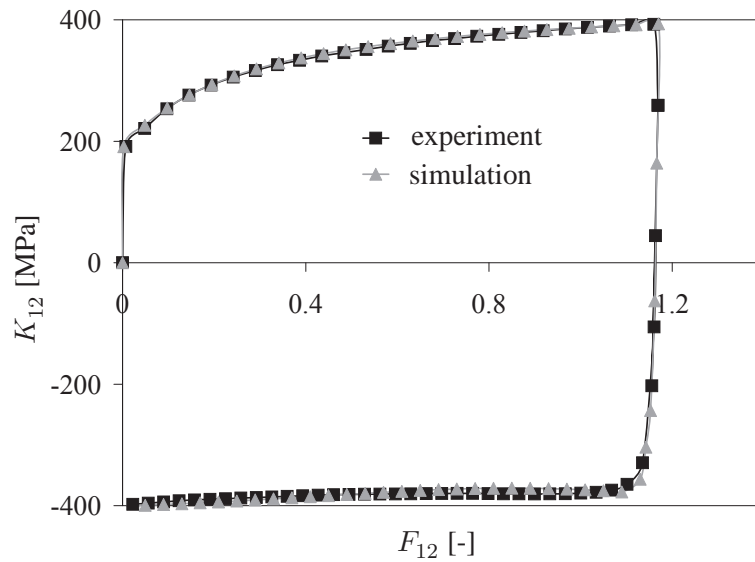


Figure 3.5: Comparison of the experimental cyclic simple-shear data with the corresponding identified full yield stress model prediction.

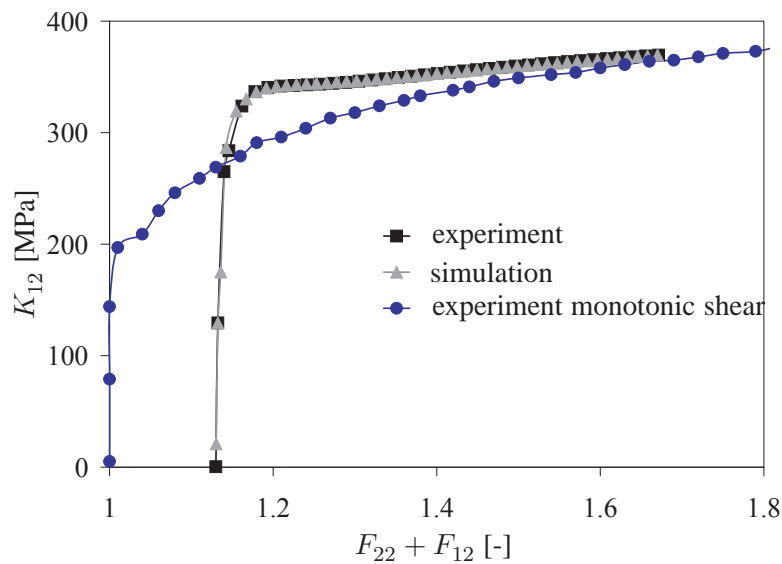


Figure 3.6: Comparison of the experimental tension-shear data for strain path 1 in Figure 3.3 with the corresponding identified full yield stress model prediction.

pendence of cross hardening on the nature and details of the orthogonal transition from tension to shear.

### 3.4.2 Identification of the simplified yield stress model

The simplified yield stress model decouples the kinematic hardening and directional hardening, this simplification reduces the number of parameters to be determined to 17. The values of parameters describing the elastic state and initial yield surface are  $\kappa = 167.05$  GPa,  $\mu = 77.09$

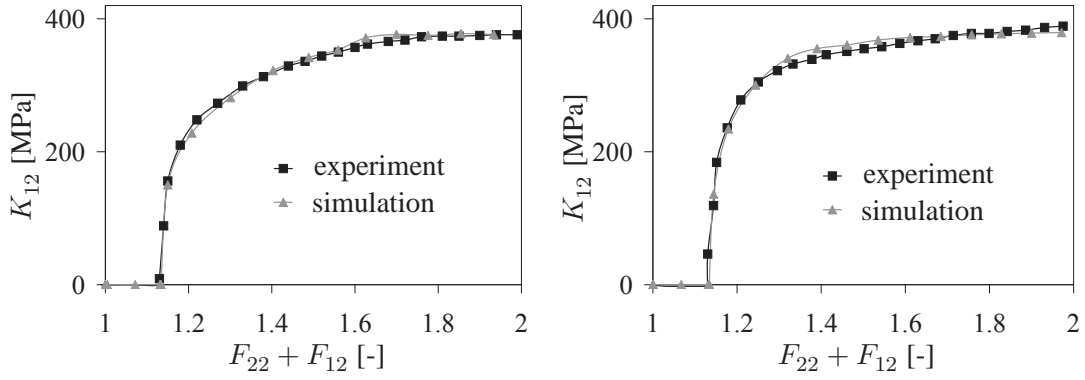


Figure 3.7: Comparison of the experimental results for strain paths 5 and 4 in Figure 3.3 with corresponding simulation results as based on the identified full yield stress model for isotropic-kinematic-cross hardening. Right: path 4. Left: path 5.

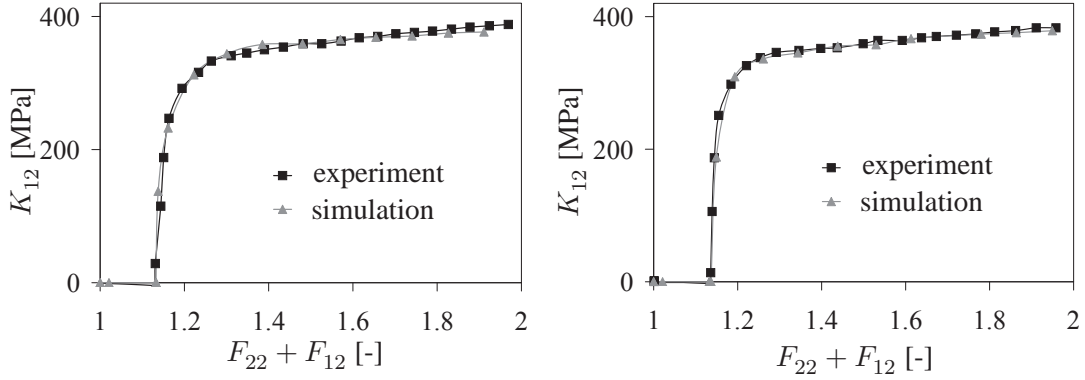


Figure 3.8: Comparison of the experimental results for strain paths 3 and 2 in Figure 3.3 with corresponding simulation results as based on the identified full yield stress model for isotropic-kinematic-cross hardening. Right: path 2. Left: path 3.

GPa,  $F = G = H = 0.5$  and  $L = M = N = 1.5$ . Adopting a similar procedure, as presented in the last section, successively different subsets of the complete set of material parameters are identified with specific test data. The parameters  $s_r$ ,  $c_r$ ,  $x_0$  and  $c_x$  are determined from monotonic and cyclic shear tests. The identified set of parameters is presented in Table 3.3.

| Parameter | value  | units |
|-----------|--------|-------|
| $x_0$     | 93.58  | MPa   |
| $s_r$     | 139.56 | MPa   |
| $s_s$     | 343.14 | MPa   |

| Parameter | value |
|-----------|-------|
| $c_x$     | 35.86 |
| $c_r$     | 3.87  |

Table 3.3: Material parameter values for LH 800 using only cyclic shear data.

Keeping these identified parameters constant, the parameters  $c_l$ ,  $s_s$ ,  $s_l$  and  $c_d$  are then determined from the tension-shear test data of strain path 1 presented in Figure 3.3. This procedure yields the values of these parameters as  $c_l = 49$ ,  $s_s = 343.193$ ,  $s_l = 0.0$  MPa and  $c_d = 5.314$ . In the final global run using the monotonic and cyclic shear test as well as the tension-shear

test data of strain path 1 presented in Figure 3.3 a variation of all parameters is performed. The identified set parameters for the complete simplified yield stress model can be seen in Table 3.4. A comparison of numerical fit with the corresponding experimental cyclic shear data and tension-shear data of strain path 1 presented in Figure 3.3 is presented in Figure 3.9 and Figure 3.10. Parameter identification of simplified yield stress model for the steel DC06 can be found in Appendix A.

| Parameter     | value   | units |
|---------------|---------|-------|
| $\kappa$      | 167050  | MPa   |
| $\mu$         | 77097   | MPa   |
| $\sigma_{Y0}$ | 330.79  | MPa   |
| $x_0$         | 101.32  | MPa   |
| $s_r$         | 193.447 | MPa   |
| $s_s$         | 45.1    | MPa   |
| $s_l$         | 0.0     | MPa   |

| Parameter | value   |
|-----------|---------|
| $c_x$     | 92.81   |
| $c_d$     | 828.273 |
| $c_l$     | 5.1     |
| $c_r$     | 3.7818  |

Table 3.4: Identified parameters of the simplified yield stress model for LH 800.

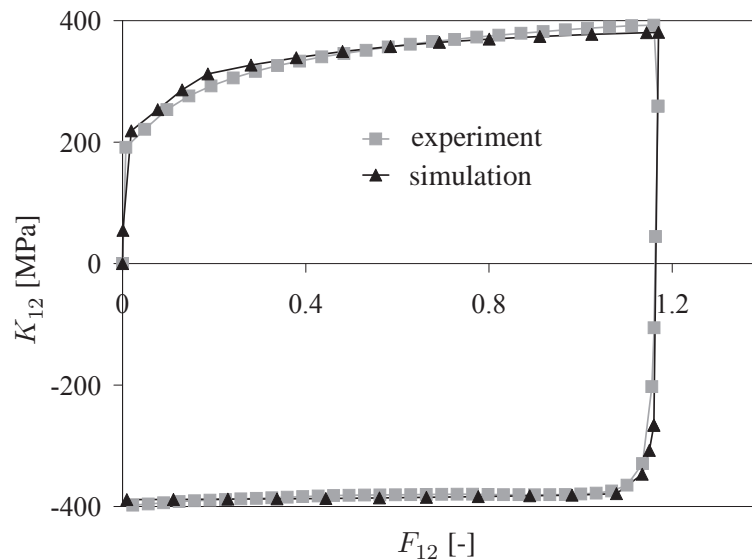


Figure 3.9: Comparison of the experimental cyclic simple-shear data with the corresponding identified (simplified) yield stress model prediction.

For the validation of the identified hardening model, the simplified yield stress model is used to simulate the behavior of LH800 along the experimental strain paths 2 to 5 shown in Figure 3.3. These were not used in the identification procedure. The results of this are shown in Figure 3.11 and 3.12. The good agreement between the numerical prediction of the simplified yield stress model and the experiments can be visualized.

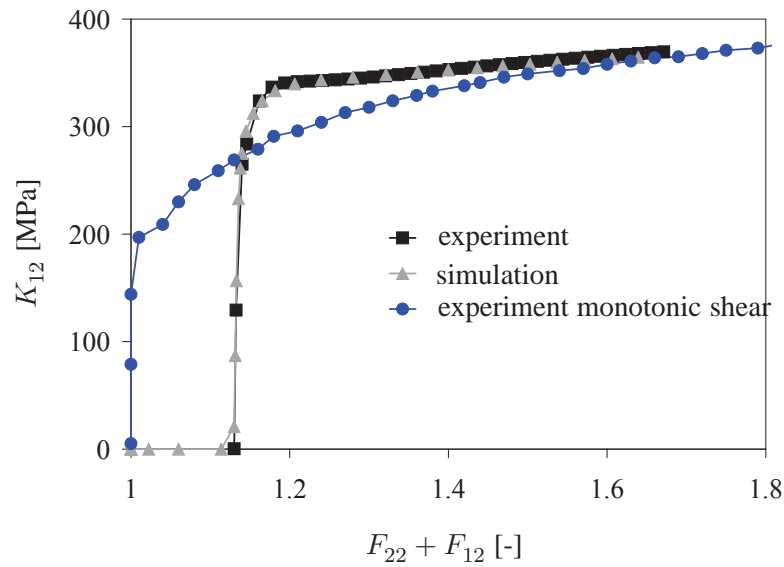


Figure 3.10: Comparison of the experimental tension-shear data for strain path 1 in Figure 3.3 with the corresponding identified (simplified) yield stress model prediction.

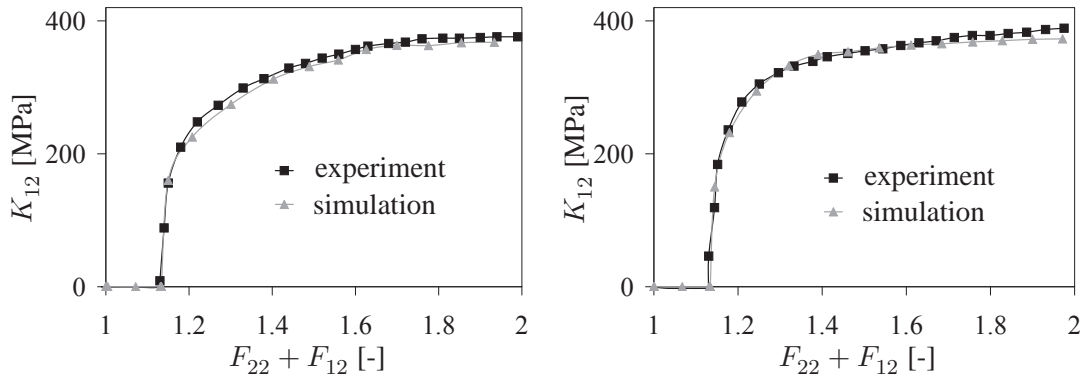


Figure 3.11: Comparison of the experimental results for strain paths 5 and 4 in Figure 3.3 with corresponding simulation results as based on the identified (simplified) yield stress model for isotropic-kinematic-cross hardening. Right: path 4. Left: path 5.

### 3.5 Evolution of internal state variables

In this section we consider the evolution of internal state variables to understand the behavior of the yield stress model and simplified yield stress model. For this, we consider a simple reverse shear test and an orthogonal tension-shear strain path 1 as shown in Figure 3.3 for the full yield stress model. Figure 3.13 shows the evolution of the saturation value of the back stress  $s_x$  and the magnitude of shear stress over the accumulated plastic strain for the full yield stress model. The shear stress ( $K_{12}$ ) curve clearly exhibits the hardening stagnation followed by the pronounced Bauschinger effect after load reversal. The  $s_x$  curve representing the evolution of  $s_x$  shows an increase during the forward shear stage, a slight decrease immediately after load reversal, becomes approximately constant for a very short time and then begins to increase

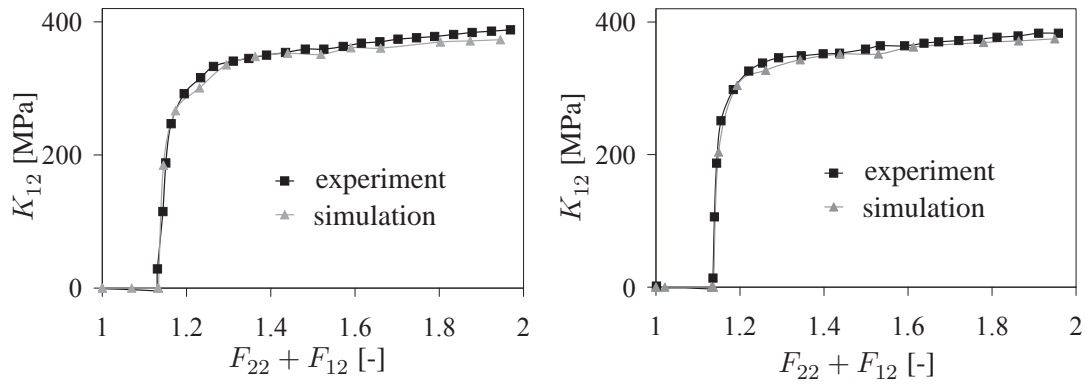


Figure 3.12: Comparison of the experimental results for strain paths 3 and 2 in Figure 3.3 with corresponding simulation results as based on the identified (simplified) yield stress model for isotropic-kinematic-cross hardening. Right: path 2. Left: path 3.

again in the course of further loading. Here, the evolution of  $s_x$  is responsible for the hardening stagnation via Equation 3.12.

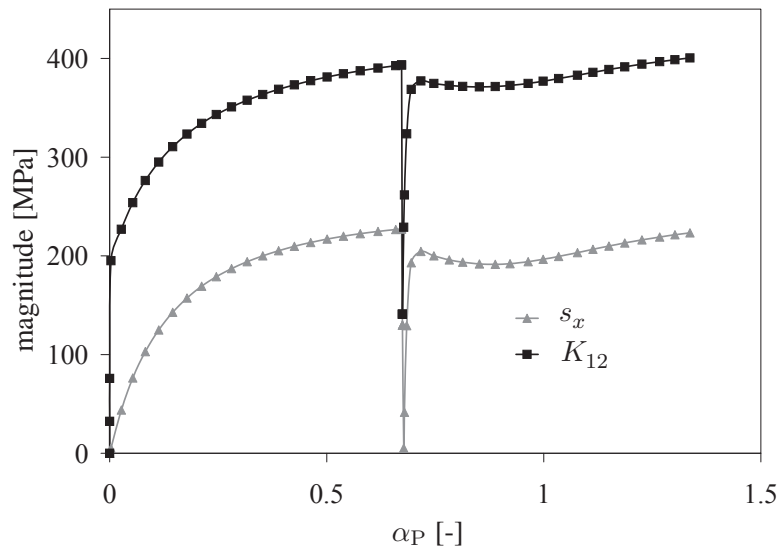


Figure 3.13: Evolution of internal state variable  $s_x$  and shear stress  $K_{12}$  for reverse shear experiment predicted by yield stress model.  $\alpha_P$  represents accumulated plastic strain.

Figure 3.14 shows the evolution of the saturation value of the back stress  $s_x$  and the magnitude of shear stress over the accumulated plastic strain for the simplified yield stress model. The shear stress ( $K_{12}$ ) curve clearly does not exhibit the hardening stagnation after load reversal. This behavior is due to the fact of decoupling the kinematic hardening from the directional hardening tensor  $\mathcal{S}$ . The shear stress ( $K_{12}$ ) curve shows the pronounced Bauschinger effect after load reversal. The  $s_x$  curve representing the evolution of  $s_x$ , shows the same behavior as shown by the shear stress ( $K_{12}$ ) curve. The hardening stagnation after load reversal can not be captured in the case of simplified yield stress model.

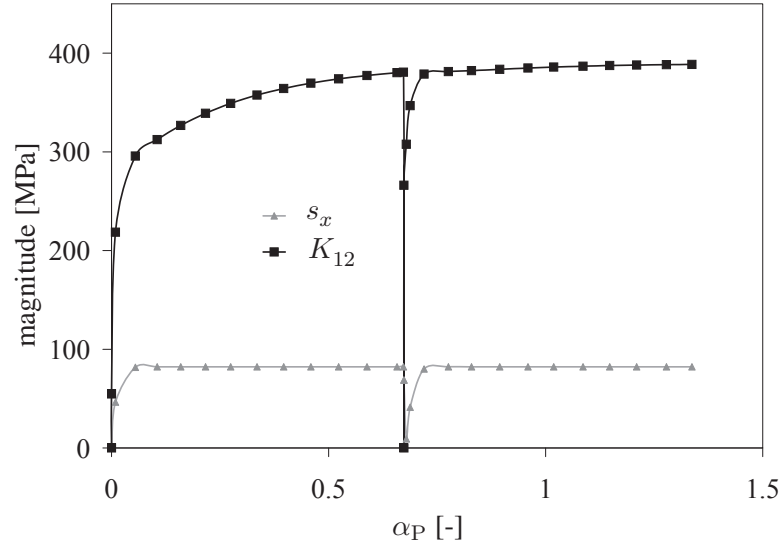


Figure 3.14: Evolution of internal state variable  $s_x$  and shear stress  $K_{12}$  for reverse shear experiment predicted by simplified yield stress model.  $\alpha_P$  represents accumulated plastic strain.

Now consider the case of orthogonal tension-shear test. As shown in Figure 3.15, during the tensile deformation the evolution of  $\mathcal{S}$  is dominated by the evolution of  $s_d$  which increased monotonically during the first stage and then dropped to zero at the beginning of the subsequent (shear) stage. In contrast, the value of  $|\mathcal{S}_l|$  remains zero during the first stage and then jumps to the value of  $s_d$  after the strain path change. Such behavior of  $s_d$  and  $|\mathcal{S}_l|$  immediately after the orthogonal strain path change leads to the cross hardening. At the beginning of second stage,  $|\mathcal{S}_l|$  decreases more rapidly than the  $s_d$  increases. This result in short softening stage followed by cross hardening.

For the simplified yield stress model, Figure 3.16 shows the evolution of  $|\mathcal{S}|$ ,  $|\mathcal{S}_d|$  and  $|\mathcal{S}_l|$  for the orthogonal tension-shear test. Since the directional hardening tensor  $|\mathcal{S}|$  decouples with the kinematic hardening in the simplified yield stress model, all the contribution of  $|\mathcal{S}|$  now goes to the isotropic hardening during the first stage. The latent part  $|\mathcal{S}_l|$  of the directional hardening tensor  $|\mathcal{S}|$  remains negligibly small during the first stage and just after the load reversal shoots to a finite value to capture the cross-hardening effect. It is evident that,  $|\mathcal{S}_l|$  decreases more rapidly than the  $s_d$  increases. This result in short softening stage followed by cross hardening.

### 3.6 Summary and conclusions

In this work, a simplified formulation of the model originally proposed by Teodosiu and Hu (1995, 1998) and later modified by Wang et al. (2008) is presented. The original model accounts for the effect of evolving oriented dislocation microstructures during loading-path changes on the hardening behavior via an evolving fourth-order structure tensor  $\mathcal{S}$ . In particular, the magnitude of this tensor determines the effective yield stress of the material, therefore this model is referred as yield stress model here. The (full) yield stress model is reduced by decoupling kinematic and directional hardening this results in reducing the number of internal variables. This

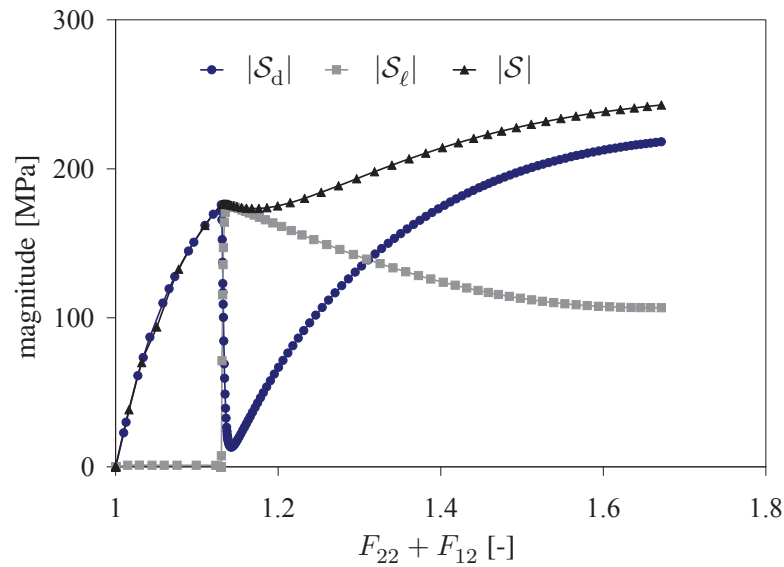


Figure 3.15: Evolution of internal state variables for tension-shear experiment path1 in Figure 3.3 predicted by yield stress model.

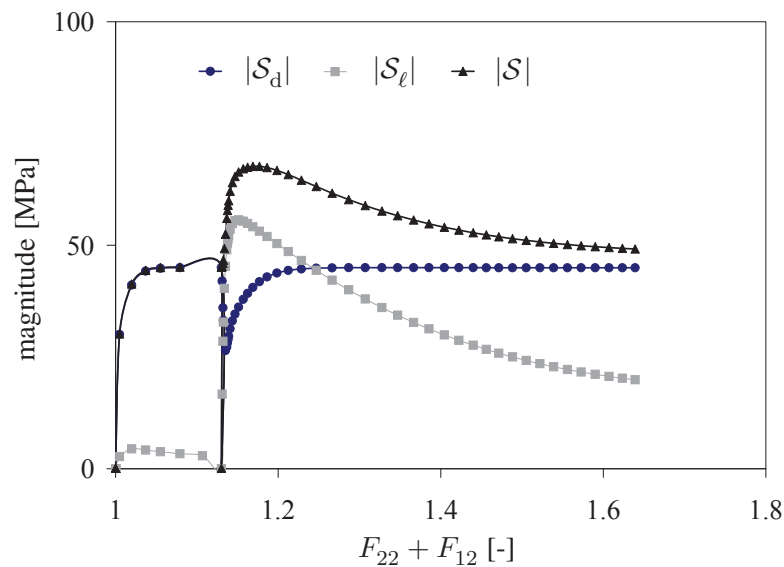


Figure 3.16: Evolution of internal state variables for tension-shear experiment path1 in Figure 3.3 predicted by simplified yield stress model.

simplification in turn results in the hardening stagnation and can not be captured accurately by the simplified model. The full yield stress model and simplified yield stress model are then identified via cyclic simple shear and orthogonal tension-shear tests. The identified models are also validated using the experimental strain paths 2 to 5 in Figure 3.3 not used in the identification procedure. In contrast to the full yield stress model, the simplified yield stress model can not capture the hardening stagnation after load reversal.



## Chapter 4

# Comparison of the hardening behavior of the sheet steel LH800 for tests with strain path changes and its influence on springback

**Abstract**– Metal forming processes generally involve large strain resulting in significant microstructural development and the development of different types of hardening. Accurate numerical simulation of such complex metal forming processes requires an appropriate material model that describes the material behavior adequately. In this work we used a material model that accounts for the changes in the size, center, and shape of the yield surface associated with isotropic, kinematic and cross hardening, respectively. The objective of the current work is to investigate the influence of the test data, i.e. uniaxial tension-compression, simple reverse shear and cyclic pure bending, on the material model parameters. The different parameter sets are applied to a draw-bending test simulation which includes springback. The simulation results are compared with experimental results.

### 4.1 Introduction

In complex metal forming processes, sheet metal undergoes severe strain path changes and large plastic deformations involving significant induced flow anisotropy resulting from the development of persistent oriented (planar) dislocation structures. A material model is required which accounts for the effect of the evolution of this oriented dislocation microstructure on the anisotropic hardening behavior and should be able to simulate the metal forming processes and be able to predict the springback effect, a phenomenon which is vital in structural component's accuracy. The common metal forming processes usually consist of two stages, loading/forming stage and releasing the final part to observe the springback. The simulation of springback appears to be the minor task, as compared to the simulation of the loading/forming stage, because of the absence of contact stresses and applied loading, the final equilibrium state can easily be achieved. But it remains a great challenge in the simulation of the metal forming processes and has been investigated over the years by researchers (e.g. (Kleiner et al., 2005), Wang et al. (2005), Oliveira et al. (2007)).

After formulating the material model which is capable of describing the material behavior under most common but complex strain path changes, the next challenge lies in the identification of the material model using the available experiments. The most widely used experimental test to evaluate the strain-stress response for a monotonic strain path is the uniaxial tension test. But the identification of the aforementioned material model can not be done using only the uniaxial tensile tests, and therefore other loading paths need to be investigated for the identification of

material parameters. To get a strain reversal in the loading path (for the Bauschinger effect) the tests which have to be investigated are tension-compression tests (Yoshida et al. (2002)), reverse shear tests (Bouvier et al. (2006); Noman et al. (2010)) and cyclic pure bending tests (Boers et al. (2010); Brunet et al. (2001); Yoshida et al. (1998)). The conventional tension-compression tests are commonly used for the identification of material parameters over the decades but these tests are generally very difficult to perform due to the buckling of the sheet sample (Yoshida et al. (2002)). To overcome this problem, Yoshida et al. (1998) suggested a pure bending test and performed cyclic bending of thin sheets. Based on cyclic bending test data, Yoshida et al. (1998) identified the material parameters for a combined isotropic and kinematic hardening model by using an optimization technique based on the iterative approximation concept. Later, Brunet et al. (2001) used cyclic bending test data simultaneously with the tensile test data to identify the hardening parameters using an inverse approach. Recently Carbonnière et al. (2009) performed a comparison of work hardening using the identified parameters from one cycle of a bending test and compared it with reverse shear test data. It should be noted that, in a bending test, the maximum strain reached in each cycle for thin sheet metal of 1 mm thickness is around 0.05 which is rather small. The simple shear tests performed by Rauch (1998); Z. Hu and Teodosiu (1992) and more recently by Bouvier et al. (2006); Flores et al. (2007); Haddadi et al. (2006); van Riel and van den Boogaard (2007) have shown that large amplitudes of strain can be achieved, which is suitable for identifying isotropic and kinematic hardening parameters at large level of strains. In order to identify the cross hardening parameters, a test involving an orthogonal or quasi orthogonal strain path has to be used in the identification. This is achieved by using the orthogonal tension-shear tests (Bouvier et al. (2006); Haddadi et al. (2006); van Riel and van den Boogaard (2007)). Bouvier et al. (2006); Flores et al. (2007); Haddadi et al. (2006); Noman et al. (2010) recently successfully used the orthogonal tension shear test for the identification of cross hardening parameters.

In Noman et al. (2010) we introduced and validated a new model which accounts for the effect of the anisotropic hardening behavior due to the evolving microstructure under complex strain paths and large deformations. The model accounts for changes in the size, center, and shape of the yield surface associated with isotropic, kinematic and cross hardening, respectively. In the current work we used three types of test data i.e. cyclic bending test data, tension-compression test data and reverse shear test data along with orthogonal tension shear data to identify the three different sets of material parameters of the presented material model. All three afore mentioned tests involve different amounts of inelastic deformation and have different states of stress. Hence, it is instructive to compare the influence of the test data used for identification on the material model parameters. This is done by identifying a different set of the material model parameters from the uniaxial tension-compression test, the simple reverse shear test and the cyclic pure bending test respectively. Then each test is simulated using the parameters based on the other two tests. The simulated responses are then compared with the experimental response. The identified sets of material parameters are also used to simulate a draw-bending test and predict the amount of springback. The predicted springback is then compared with the actual experimentally observed springback for each set of material parameters.

The current work begins with the summary of the material model implemented in the framework of the multiplicative decomposition of the deformation gradient and the assumption of

small elastic strain relevant to metal inelasticity. Afterwards the experimental setup and details of the tests are presented in Section 3 along with the results of the tests, namely tension-compression test, simple reverse shear test and cyclic pure bending test. In Section 4, the identification scheme together with the results of the identifications are discussed for each test data. The results obtained using different test data are then compared to analyze the influence of the database used. In Section 6, the identified parameters are used to simulate the draw-bending test and a comparison of the predicted and experimentally obtained amount of springback is done. The work ends in Section 7 with the summary and conclusion.

## 4.2 Material Model

The phenomenological representation of evolving hardening behavior in terms of changes in the size, center and shape of the yield surface offers the means to characterize the behavior of the steels of interest during complex, non-proportional loading processes present in many technological processes (e.g., deep-drawing). The challenge lies in the connection of such changes in the yield surface geometry with the underlying microscopic and physical mechanisms of grain and dislocation microstructural development in polycrystalline metals. One basic expectation in this regard is that the grain microstructure in sheet metals is determined almost solely by the rolling process. Forming processes like cup drawing are expected to result in little or no change in this microstructure. Consequently, during forming processes, yield surface evolution is generally expected to be due almost solely to an evolving dislocation microstructure at the grain- or grain-cluster level. This is the focus of the current model.

The formulation of the current model is carried out in the framework of the standard inelastic multiplicative decomposition  $\mathbf{F} = \mathbf{F}_E \mathbf{F}_P$  of the deformation gradient  $\mathbf{F}$  (Simo and Hughes (e.g., 1998)). Such a decomposition arises naturally, e.g. in the context of the modeling of  $\mathbf{F}_P$  as a change of local reference configuration Svendsen (2001). In this context, one obtains in particular the result

$$\mathbf{R}_E^T \mathbf{L}_E \mathbf{R}_E = \mathbf{R}_E^T \mathbf{L} \mathbf{R}_E - \mathbf{U}_E \mathbf{L}_P \mathbf{U}_E^{-1} = \mathbf{R}_E^T \dot{\mathbf{R}}_E + \dot{\mathbf{U}}_E \mathbf{U}_E^{-1} \quad (4.1)$$

via the right polar decomposition  $\mathbf{F}_E = \mathbf{R}_E \mathbf{U}_E$  of  $\mathbf{F}_E$  for the back-rotated form of  $\mathbf{L}_E := \dot{\mathbf{F}}_E \mathbf{F}_E^{-1}$  in terms of  $\mathbf{L} := \dot{\mathbf{F}} \mathbf{F}^{-1}$  and  $\mathbf{L}_P := \dot{\mathbf{F}}_P \mathbf{F}_P^{-1}$ . For the current case of polycrystalline metals and small elastic strain, we have

$$\begin{aligned} \mathbf{U}_E &\approx \mathbf{I} + \ln \mathbf{U}_E, \\ \dot{\mathbf{U}}_E \mathbf{U}_E^{-1} &\approx \overline{\dot{\ln \mathbf{U}_E}}. \end{aligned} \quad (4.2)$$

Substituting these into (4.1), and taking the symmetric and skew-symmetric parts of the result, one obtains the evolution relations

$$\begin{aligned} \overline{\dot{\ln \mathbf{U}_E}} &= \mathbf{R}_E^T \mathbf{D} \mathbf{R}_E - \mathbf{D}_P, \\ \dot{\mathbf{R}}_E &= \mathbf{W} \mathbf{R}_E - \mathbf{R}_E \mathbf{W}_P, \end{aligned} \quad (4.3)$$

for  $\ln \mathbf{U}_E$  and  $\mathbf{R}_E$ , respectively, in the incremental context.  $\mathbf{D} := \text{sym}(\mathbf{L})$  is the continuum rate of deformation,  $\mathbf{D}_P := \text{sym}(\mathbf{L}_P)$  its inelastic counterpart,  $\mathbf{W} := \text{skw}(\mathbf{L})$  the continuum

spin, and  $\mathbf{W}_P := \text{skw}(\mathbf{L}_P)$  the plastic spin. Restricting the current formulation to the case of sheet metal forming, it is reasonable to assume that the texture in these materials achieved during rolling remains largely unchanged during forming processes like tension, compression, simple shear, cyclic simple shear, and combinations of these. In this case,  $\mathbf{W}_P$  is negligible, and the evolution of  $\mathbf{R}_E$  depends only on  $\mathbf{W}$ , in which case it reduces to a purely kinematic quantity (i.e., the Jaumann rotation). In addition, focusing in this work on the material behavior of sheet metal during forming below the forming limit, we assume for simplicity that damage or any other process resulting in inelastic volume changes are negligible. In this case, plastic incompressibility  $\det(\mathbf{F}_P) = 1$  pertains, implying  $\text{tr}(\mathbf{D}_P) = 0$  and  $\mathbf{D}'_P = \mathbf{D}_P$  in the incremental context.

Since the elastic range and elastic strain are small, any texture effects from rolling leading to an anisotropic elastic behavior are assumed negligible. In this case, the isotropic form

$$\mathbf{M} = \kappa \text{tr}(\mathbf{E}_E) \mathbf{I} + 2\mu \mathbf{E}'_E \quad (4.4)$$

is assumed for the Mandel stress  $\mathbf{M}$  in terms of the elastic strain  $\mathbf{E}_E := \ln \mathbf{U}_E$ , bulk modulus  $\kappa$ , shear modulus  $\mu$ , and deviatoric part  $\mathbf{E}'_E$  of  $\mathbf{E}_E$ . Lastly, again in the framework of small elastic strain,  $\mathbf{M}$  and  $\mathbf{R}_E$  determine the Kirchhoff stress  $\mathbf{K}$  via

$$\mathbf{K} = \mathbf{R}_E \mathbf{M} \mathbf{R}_E^T. \quad (4.5)$$

Consequently, in contrast to  $\mathbf{K}' = \mathbf{R}_E \mathbf{M}' \mathbf{R}_E^T$ ,  $\text{tr}(\mathbf{K}) = \text{tr}(\mathbf{M})$  of  $\mathbf{K}$  is independent of  $\mathbf{R}_E$ .

In this framework, then, the material behavior of polycrystalline sheet metal during forming processes below the forming limit is predominantly determined by a changing dislocation microstructure and attendant evolving anisotropic yield behavior. Besides a shift of the yield surface and its proportional expansion as in the case of conventional combined hardening, the current model also accounts for an evolving yield surface shape and so distortional hardening. In the current notation, the model is written simply in the form

$$\phi = \sqrt{(\mathbf{M} - \mathbf{X}) \cdot \mathcal{A}(\mathbf{M} - \mathbf{X})} - \sigma_{Y0} - r \quad (4.6)$$

in terms of the initial yield stress  $\sigma_{Y0}$ . For the class of materials under consideration, the saturation (i.e., Voce) form

$$\dot{r} = c_r (s_r - r) \dot{\alpha}_P \quad (4.7)$$

for the evolution of  $r$  is appropriate, driven by that of the equivalent inelastic deformation  $\alpha_P$ . Here,  $c_r$  represents the rate, and  $s_r$  the value, for saturation associated with  $r$ . Since  $\sigma_{Y0}$  is the initial yield stress (i.e., for  $\alpha_P = 0$ ), the initial value  $r_0$  of  $r$  is zero. In the current rate-independent context,  $\alpha_P$  is determined as usual by the consistency condition. Analogous to isotropic hardening, kinematic hardening is modeled via the saturation (i.e., Armstrong-Frederick) form

$$\dot{\mathbf{X}} = c_x (s_x \mathbf{N}_P - \mathbf{X}) \dot{\alpha}_P \quad (4.8)$$

for the evolution of  $\mathbf{X}$  depending on corresponding (constant) saturation rate  $c_x$ , (constant) saturation magnitude  $s_x$ , as well as the (variable) direction  $\mathbf{N}_P := \mathbf{D}_P / |\mathbf{D}_P|$  of the rate of inelastic deformation

$$\mathbf{D}_P = \dot{\alpha}_P \partial_{\mathbf{M}-\mathbf{X}} \phi, \quad (4.9)$$

which is modeled here in associated form. The initial value of  $\mathbf{X}$  is assumed to be zero.

The constitutive model formulation is completed by an evolution relation for  $\mathcal{A}$  in order to represent the effect of cross hardening on the material behavior. The form of this relation introduced in what follows is based on the idea that active or “dynamic” dislocation microstructures oriented with respect to the current loading direction (idealized in the model context by  $\mathbf{N}_P$ ) persist and become inactive or “latent” after a loading-path change and strengthen existing obstacles to glide-system activation in the new loading direction. In addition, both dynamic and latent dislocation structures are assumed to saturate with increasing accumulated inelastic deformation. These assumptions are built into the constitutive relation

$$\begin{aligned} \dot{\mathcal{A}} &= c_d (s_d \mathbf{N}_P \otimes \mathbf{N}_P - \mathcal{A}_d) \dot{\alpha}_P \\ &+ c_l \{s_l (\mathcal{I}_{\text{dev}} - \mathbf{N}_P \otimes \mathbf{N}_P) - \mathcal{A}_l\} \dot{\alpha}_P \end{aligned} \quad (4.10)$$

for the evolution of  $\mathcal{A}$ . Here,  $\mathcal{I}_{\text{dev}}$  is the deviatoric part of the fourth-order identity tensor, and

$$\begin{aligned} \mathcal{A}_d &:= (\mathbf{N}_P \cdot \mathcal{A} \mathbf{N}_P) \mathbf{N}_P \otimes \mathbf{N}_P, \\ \mathcal{A}_l &:= \mathcal{A} - \mathcal{A}_d, \end{aligned} \quad (4.11)$$

represent the “dynamic” and “latent” parts of  $\mathcal{A}$ , respectively. More precisely, these are the projections of  $\mathcal{A}$  parallel and orthogonal, respectively, to the current (instantaneous) inelastic flow direction  $\mathbf{N}_P$ . The first term in (4.10) is of the saturation type with respect to  $\mathcal{A}_d$ , with  $c_d$  the rate of saturation, and  $s_d \mathbf{N}_P \otimes \mathbf{N}_P$  the saturation value, respectively, of  $\mathcal{A}_d$ . Likewise,  $c_l$  is the saturation rate, and  $s_l (\mathcal{I}_{\text{dev}} - \mathbf{N}_P \otimes \mathbf{N}_P)$  the saturation value, of  $\mathcal{A}_l$ . The initial value  $\mathcal{A}_0$  of  $\mathcal{A}$  is determined by any Hill initial flow orthotropy due to any texture from rolling. In contrast to some of the models discussed in the introduction, e.g., Teodosiu and Hu (1998), Wang et al. (2008), or Dafalias et al. (2003); Feigenbaum and Dafalias (2007), note that there is no direct coupling between kinematic and distortional hardening in the current model.

The current material model was implemented in the commercial FE codes ABAQUS and LS-Dyna via the user material interfaces provided. Besides the two elasticity parameters  $\kappa$ ,  $\mu$  and the 6 parameters (e.g., in the sense of Hill:  $F$ ,  $G$ ,  $H$ ,  $L$ ,  $M$ ,  $N$ ) for the initial flow orthotropy, this model contains 9 hardening parameters  $\sigma_{Y0}$ ,  $c_r$ ,  $s_r$ ,  $c_x$ ,  $s_x$ ,  $c_d$ ,  $s_d$ ,  $c_l$ ,  $s_l$  to be identified using the tests to be described next.

### 4.3 Material testing

Numerical simulation of elastic-plastic metal forming processes is impossible without the knowledge of the material behavior. In order to characterize the material behavior of the metal the most widely used experimental tests are uniaxial tension-compression and simple reverse shear tests. In addition to the commonly used tests, a pure bending test is also conducted in order to characterize the material.

#### 4.3.1 Material

The material under investigation is ferritic steel LH800 which is characterized by a good cold formability before and a high stiffness after hardening. The main feature of this material is

the ability of air hardening having a carbon content of approximately 0.1%. Another property of this steel is the good suitability for thermal joining making it an interesting sheet material for automotive industry. The average Young's Modulus  $E$  over the three directions  $0^\circ$ ,  $45^\circ$  and  $90^\circ$  with respect to the rolling direction is determined to 200 450 MPa with Poisson's ratio  $\nu = 0.3$ . The chemical composition of steel LH800 is presented in Table 1. This sheet steel is characterized by an initial texture consisting of fine-grained ferrite, grain size of approximately  $8 \mu\text{m}$  in diameter, see Figure 4.1 (Tekkaya et al. (2008)).

|        |       |       |       |       |       |        |        |       |       |
|--------|-------|-------|-------|-------|-------|--------|--------|-------|-------|
| C      | Mn    | Si    | P     | S     | N     | Al     | Cu     | Cr    | Ni    |
| 0.088  | 1.957 | 0.276 | 0.019 | 0.001 | 0.008 | 0.035  | 0.066  | 0.774 | 0.047 |
| B      | Mo    | As    | Sn    | Ti    | V     | Nb     | Ca     |       |       |
| 0.0043 | 0.17  | 0.003 | 0.011 | 0.031 | 0.064 | 0.0046 | 0.0006 |       |       |

Table 4.1: Chemical composition of steel LH800. All values are given as weight percentage.

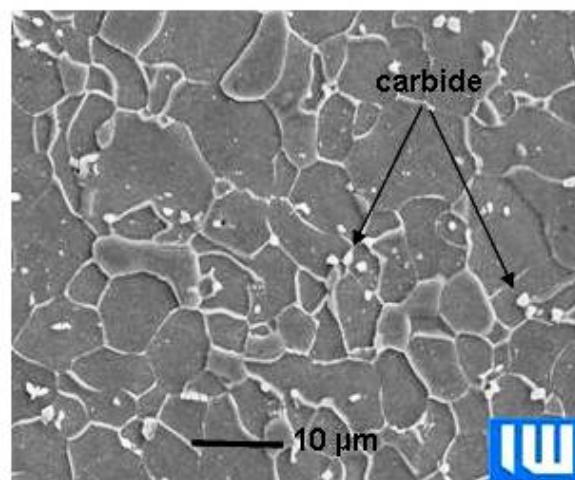


Figure 4.1: Scanning electron micro graph showing microstructure of LH800 in the as received condition (Experiment IW Hannover).

#### 4.3.2 Simple shear test

For the experimental work a biaxial testing device developed at the University of Twente was used to subject specimen shown in Fig. 4.2 to states of planar deformation. Using this device, one can carry out single- or multi-stage loading programs consisting of monotonic (e.g., forward simple-shear), reverse (e.g., forward-reverse simple-shear), and / or orthogonal (e.g., tension-shear), changes of loading direction. In particular, the latter can be carried out with or without unloading of the specimen upon change of loading direction.

#### Test setup

A vertical and a horizontal actuator can be used to deform the specimen. If only the vertical actuator is activated, the specimen is deformed in plane strain tension. If only the horizontal

actuator is used, the specimen is deformed in simple shear as can be seen in Fig. 4.2. Consequently, if the direction of movement of the horizontal actuator is reversed, reverse shear tests can be carried out. Mixed plane strain tension/simple shear loading is possible if both actuators are active simultaneously. In addition, arbitrary sequences of attainable states of deformation are also possible. The deformation field is obtained by optical measurement of an array of painted dots in the center of the deformation zone of the specimen. Since the deformation field in the deformation zone is homogeneous for the level of straining investigated in this work, the relative motion of the dots determines the deformation field. The horizontal and vertical force are recorded such that, together with the known geometry, the Cauchy stresses  $T_{11}$  and  $T_{12}$  can be computed. The plane-strain tension and simple shear tests represent the boundaries of the range of stress states achievable in the specimen with the help of the biaxial testing device. By applying different combinations of simple shear and plane-strain tension, different stress states on the yield surface are achieved. The exact position of the yield state in principal stress space, however, is unknown since the transverse stress cannot be measured. Further details concerning the experimental setup can be found in Noman et al. (2010); van Riel (2009); van Riel and van den Boogaard (2007). The strain rate for all experiments was set to  $10^{-3}$  1/s.

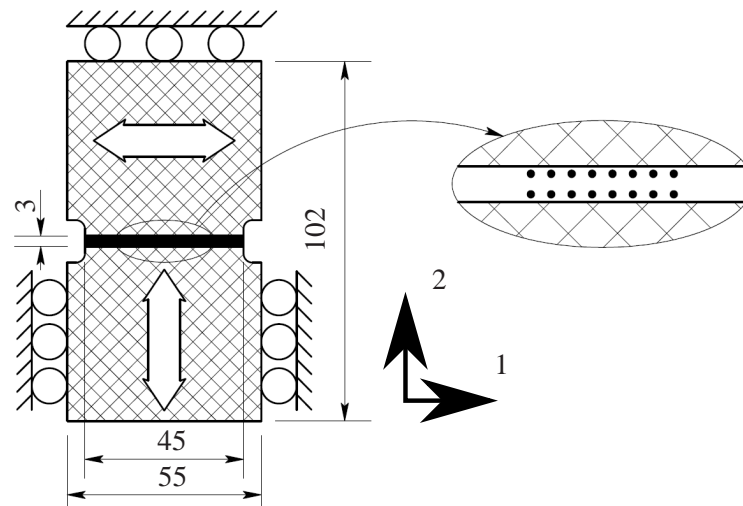


Figure 4.2: Biaxial test setup. Geometry of the tension-shear specimen and the measurement region of height 3.0mm and width 45.0 mm. The checkered region indicates the actual specimen and the black area marks the actual deformation zone. The tension direction is direction 2 and the shear direction is direction 1.

### Test results

The thickness of the sheet metal specimens used in all the tests was 0.7 mm. All tests were performed with the tension direction oriented in the rolling direction. Figure 4.3 shows the results of 2 reverse simple-shear tests. The elastic-inelastic transition for this material upon load reversal is very diffuse. The Bauschinger effect (a decrease in the flow stress after load reversal) is clearly present. It would appear that the amount of pre-shear does not influence the magnitude of the Bauschinger effect significantly. On the other hand, the test with the larger pre-shear is clearly closer to the hardening saturation level. Hardening stagnation after load

reversal is clearly visible in both cases, but less pronounced at lower pre-shear.

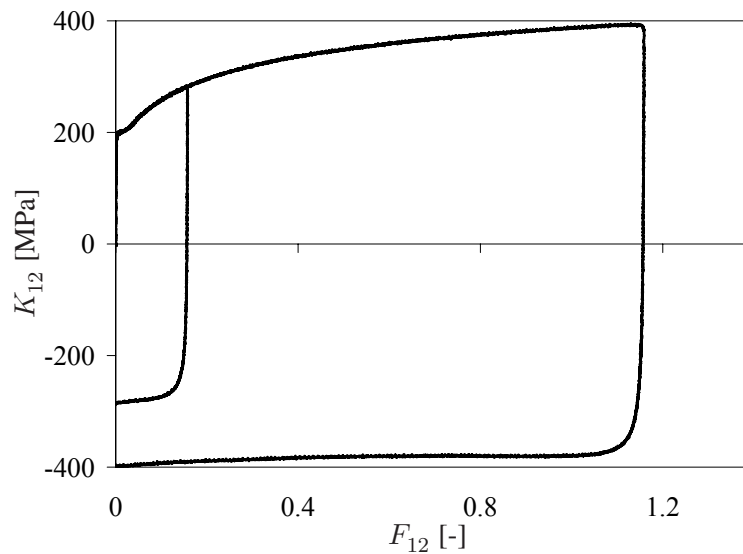


Figure 4.3: Reverse shear test results for LH800 for two different levels of pre-shear. All stress results are shown in absolute value form.  $K_{12}$  represents the relevant component of the Kirchhoff stress and  $F_{12}$  represents the relevant component of the deformation gradient.

Consider now, the results from the orthogonal tests. As stated, these consist of plane-strain tension followed by simple shear loading. The transition from tension to simple shear differs in degree of sharpness from tension to shear, Figure 4.4 is showing the 5 different continuous loading paths (numbered 1 to 5) and Figure 4.5 presents the result obtained for these paths.

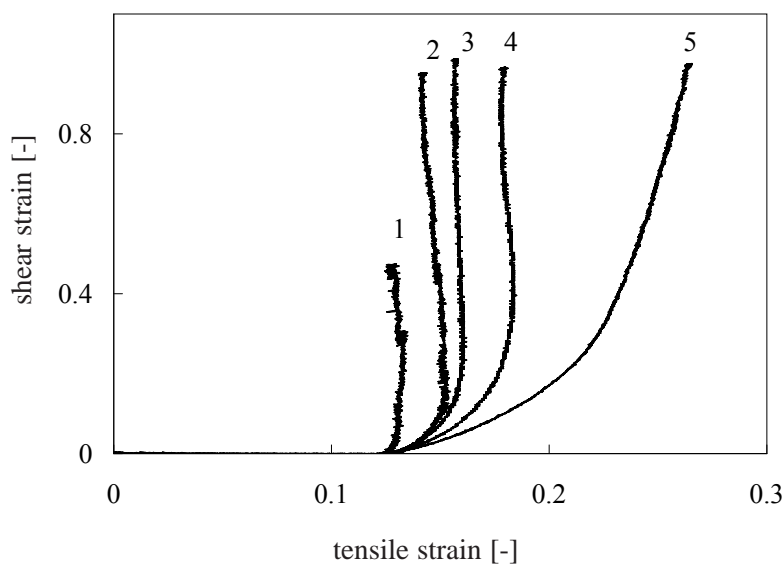


Figure 4.4: Experimental strain paths in LH800 resulting from continuous change of loading direction from tension to shear.



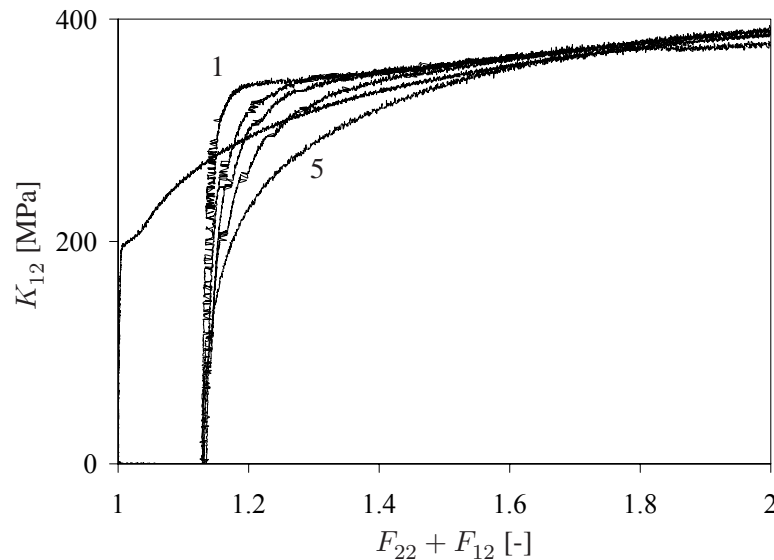


Figure 4.5: Stress response of LH800 for monotonic forward simple shear (curve starting at  $F_{22} + F_{12} = 1$ ) and for the 5 different orthogonal tension-shear paths shown in Figure 4.4.

Consistent with existing interpretations of such data in the literature, the presence or absence of cross hardening in such orthogonal tests is judged solely by comparison with the monotonic simple shear results. In particular, any overshoot of the yield stress above the monotonic level upon transition from tension to shear is an indicator of such hardening. Using this “definition”, curves 1, 2 and 3 in Figure 4.4 clearly exhibit cross hardening as can be seen in Figure 4.5, curve 4 might exhibit a little, and curve 5 clearly none at all. Further details concerning the presence of cross hardening in the Steel LH800 can be found in Noman et al. (2010).

#### 4.3.3 Uniaxial tension and tension-compression test

Tensile tests have been performed according to DIN EN 10002 in order to quantitatively describe the behavior of the air-hardening steel LH800 under uniaxial tension. The testing specimen have been cut from sheets of 1.5 mm thickness having angles of  $0^\circ$ ,  $45^\circ$  and  $90^\circ$  with respect to the rolling direction. In order to increase the precision of the resulting stress-strain diagram, five tests are conducted in each direction. The tensile tests have been performed on a universal testing machine Zwick Z250 at  $20^\circ\text{C}$  and a strain rate of  $0.005\text{ s}^{-1}$  (Tekkaya et al. (2008)). Figure 4.6 shows the results of tensile tests averaged across the three different specimen directions. The stress-strain curve analysis shows a negligible divergence of the results for the three selected directions. This implies that the initial flow anisotropy is negligible.

Besides the uniaxial tension tests, uniaxial tension-compression tests have also been performed. The strain reversal during the tension-compression test activates the kinematic hardening resulting in a decrease in the flow stress (the so called Bauschinger effect) upon unloading and reloading in compression. This tension-compression test has been performed on an existing tension compression module at IW Hannover. A flat specimen in the test is been used, unlike the commonly used cylindrical specimen, due to the fact that the material is delivered in thin sheets and that the material should be characterized in the as received form. The strain-stress

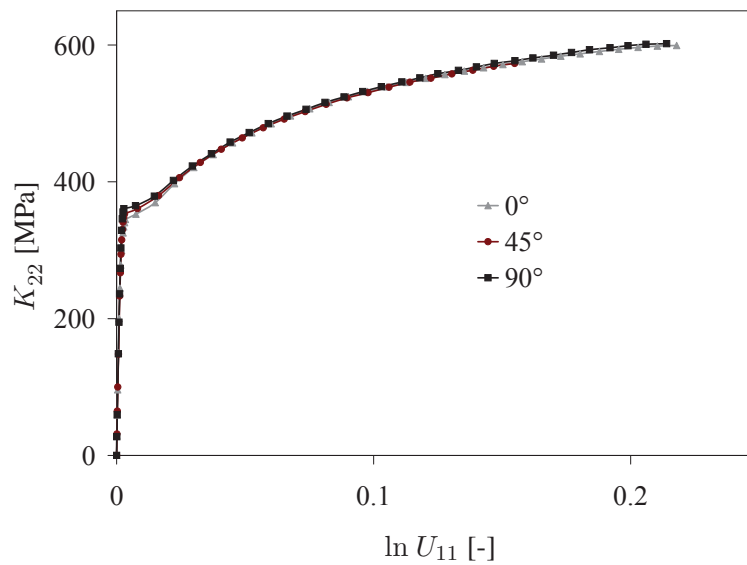


Figure 4.6: Tensile test results conducted at  $0^\circ$ ,  $45^\circ$  and  $90^\circ$  with respect to the rolling direction.  $K_{22}$  represents relevant components of Kirchoff stress and  $\ln U_{11}$  represents relevant component of logarithmic strain

response obtained as the result of the tension-compression test is presented in Figure 4.7.

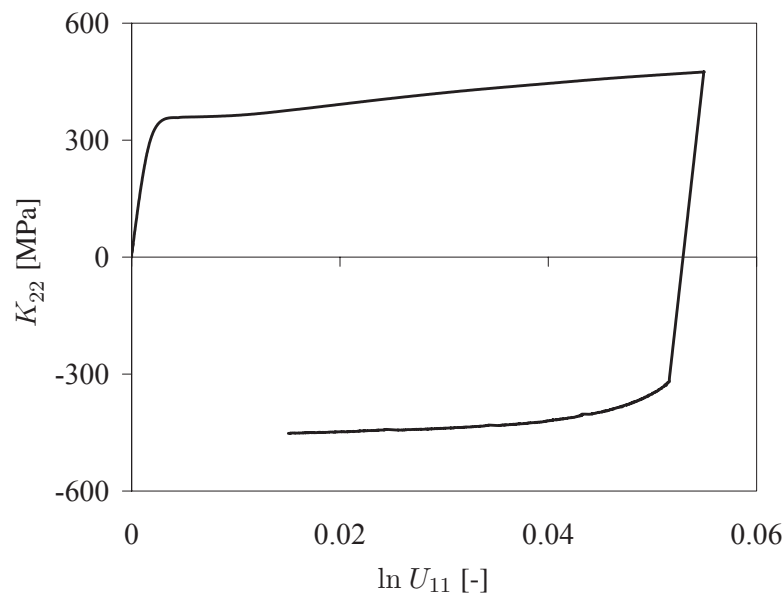


Figure 4.7: Tension-compression test result for LH800.

#### 4.3.4 Pure bending test

The pure bending test, conducted at Eindhoven University of Technology, enables the researchers to study the reversed loading, orthogonal strain path changes and elastic springback effects by applying a pure bending moment on a rectangular plate. The advantages of the pure bending

test are the absence of contact force, material slip and friction. But the pure bending test is inhomogeneous, unlike the tension-compression and the reverse shear tests.

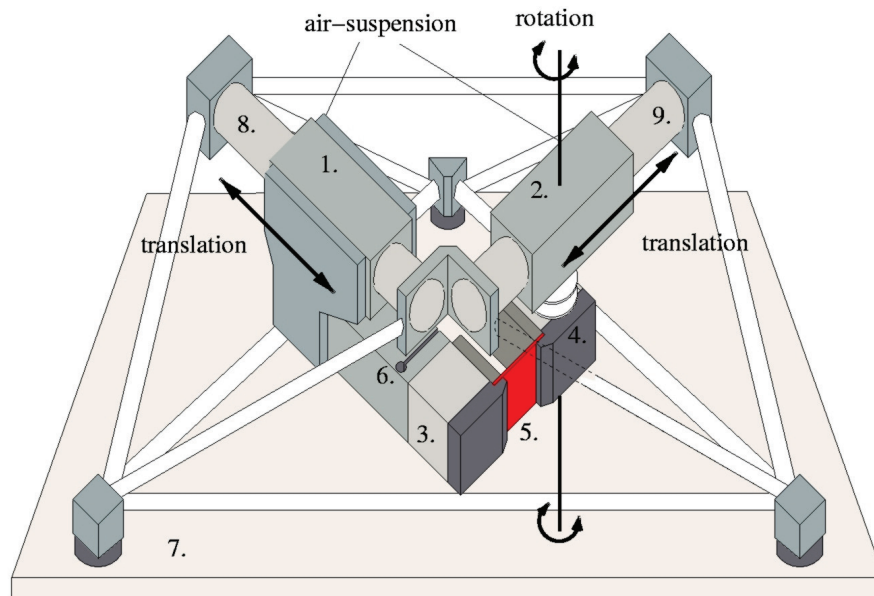


Figure 4.8: Pure bending device with air suspended clamps (Boers et al. (2010))

Figure 4.8 shows the bending device present at the Eindhoven University of Technology. The specimen (5) is clamped between the hydraulically actuated clamps (3 and 4) that are mounted orthogonally on two air suspended linear guides (1 and 2). Between the linear guide (2) and the clamp (4) is an electric motor that controls the rotation of the clamp, whereas the other clamp measures the applied bending moment by using an elastic joint (6) in combination with a set of strain gauges. Because the linear guides are positioned at a relative angle of 90 degrees, no lateral force can be transferred from one clamp to the other. The bending moment can be measured with an accuracy of 0.02 Nm. The whole set-up is positioned on a solid frame (7) and measures approximately  $1 \times 1 \times 0.5 \text{ m}^3$ .

Figure 4.9 illustrates the procedure of pure bending test. First a straight specimen, having dimensions of  $60 \times 100 \times 1.55 \text{ mm}^3$ , is clamped into the device and afterwards the specimen is bent up to an angle of  $180^\circ$  and then unbent. This process can be repeated several times. When the clamp stops at zero degrees the specimen is under stress and bent. In principle one should stop at the position when the bending moment is zero. Therefore the specimen is bent further in negative direction, the negative angle is chosen in such a way that the specimen springs back to zero degrees. If the clamp now rotates to the  $0^\circ$  position, the bending moment is zero and the sample can be taken out straight and can be used for further investigations. Now either reversed loading is applied by repeating the previous procedure or orthogonal loading can be applied. For this, the sample side parts have to be removed from the center part, as they did not deform during the first bending. From the prestrained sample, two samples are prepared of which one is used for a reversed pure bending test and the other for an orthogonal pure bending test. The effective sample dimension are  $30 \times 50 \times 1.55 \text{ mm}^3$  for each Bauschinger and orthogonal pure

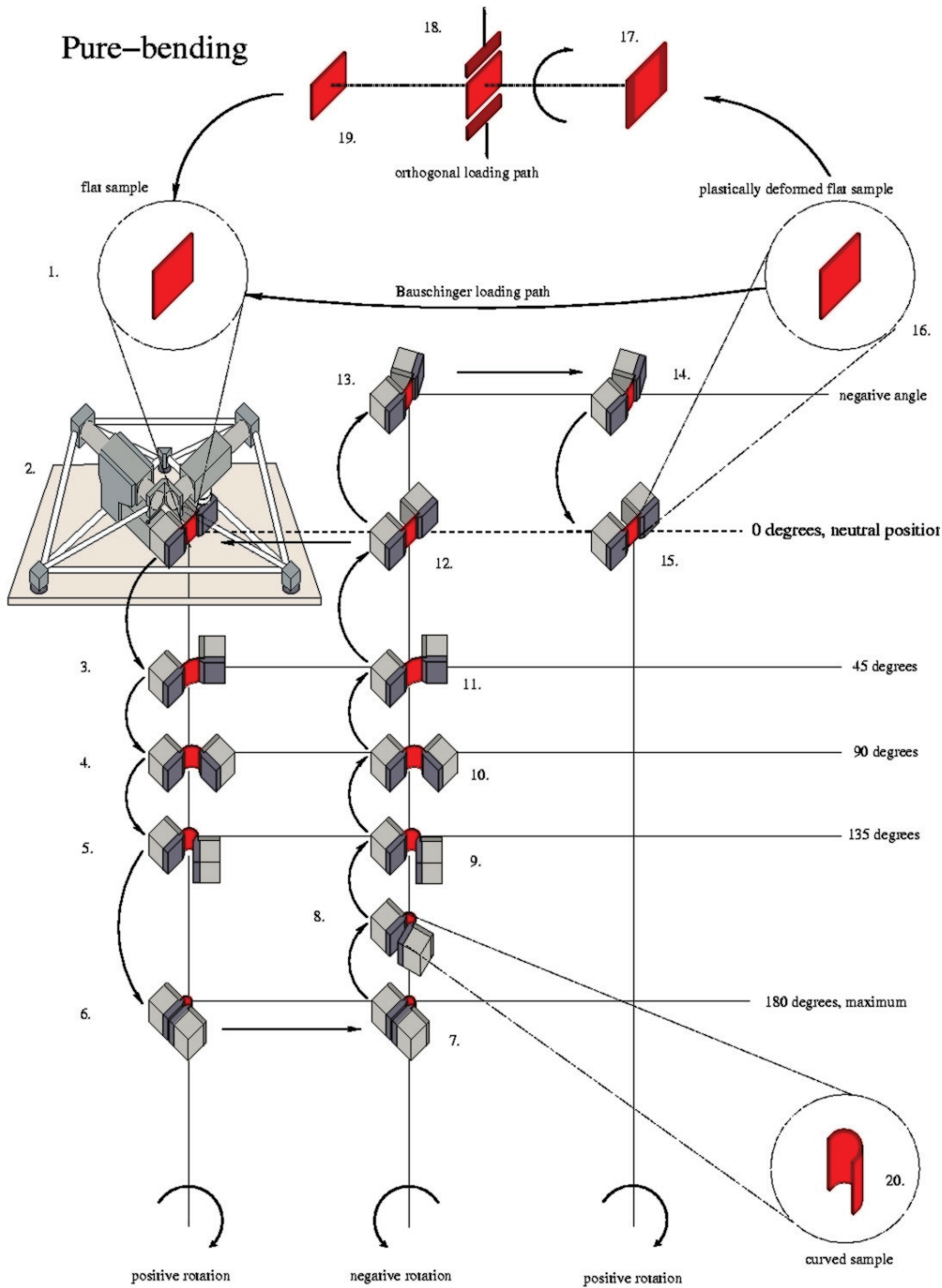


Figure 4.9: Schematic representation of pure bending experiment. (Boers et al. (2010))

bending test.

Figure 4.10 (right) presents the result of the experiments, where the samples were bent three times from  $0^\circ$  to  $180^\circ$ . The excellent agreement between the three individual experiments emphasizes the reproducibility. During the experiment the stress across the cross-section varies and that leads to the the fact that one side of the specimen is compressed, while the opposite side of the specimen is elongated. The presence of both compressive and tensile stresses at any time enables repeated reversed bending tests without necking. From the prestrained specimen, two

samples are then prepared of which one is used for a reversed pure bending test, and the other for orthogonal pure bending test. In Figure 4.10 (left), the results of the reversed (Bauschinger) test and orthogonal test is presented.

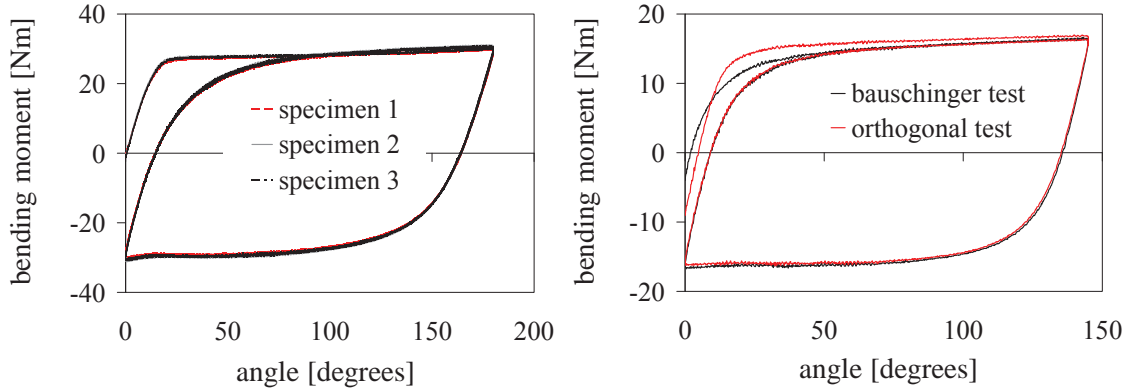


Figure 4.10: Pure bending test results. Left: Pure bending test results for 3 cycles of bending. Right: Bauschinger and Orthogonal test Results of prestrained sample.

## 4.4 Model identification

To demonstrate the capability of the presented model to describe the complex hardening behavior of LH800 during non-proportional loading just discussed, we now turn to its identification. The material parameter determination is carried out using the program LS-OPT in conjunction with LS-DYNA. The optimization technique used relies on response surface methodology (RSM) (Stander et al. (2008)), a mathematical method for constructing smooth approximations of functions in a design space. The approximations are based on results calculated at numerous points in the multi-dimensional design space. In our example, the material parameters are the design variables, and the model together with the data determine the objective function of the corresponding optimization problem.

All fits to follow are based on the fixed values of  $\kappa = 167.05$  GPa and  $\mu = 77.09$  GPa for the elastic properties of LH800, all at room temperature. Tensile tests performed on LH800 at  $0^\circ$ ,  $45^\circ$ ,  $90^\circ$  with respect to the rolling direction yielded no distinct initial orthotropy and so Hill parameter values of  $F = G = H = 0.5$  and  $L = M = N = 1.5$  are used. Strictly speaking, only  $N$ ,  $F$ ,  $G$  and  $H$  can be determined by in-plane tensile tests, while  $L$  and  $M$ , corresponding to through-thickness shear, are assumed to be equal to  $N$ .

### 4.4.1 Simple shear test

The simple shear test is homogeneous so one element simulation is sufficient. The fit procedure for the hardening model begins by using monotonic simple-shear test data to identify the Voce isotropic hardening model alone, i.e., assuming no kinematic and cross hardening. The results of this fit are shown in Table 4.2 (left). The quality of the fit can be judged via the comparison of the fitted model with the data in Figure 4.11.

|               | Value  | Units |
|---------------|--------|-------|
| $\sigma_{Y0}$ | 330.79 | MPa   |
| $s_r$         | 341.50 | MPa   |
| $c_r$         | 5.82   |       |

|               | Value   | Units |
|---------------|---------|-------|
| $\sigma_{Y0}$ | 330.79  | MPa   |
| $s_r$         | 245.684 | MPa   |
| $c_r$         | 4.295   |       |
| $s_x$         | 97.464  | MPa   |
| $c_x$         | 33.642  |       |

Table 4.2: Identified hardening model parameter values for LH800. Left: isotropic hardening parameter values determined from monotonic simple-shear test data alone. Right: isotropic-kinematic hardening parameters determined from monotonic and reverse simple-shear test data.

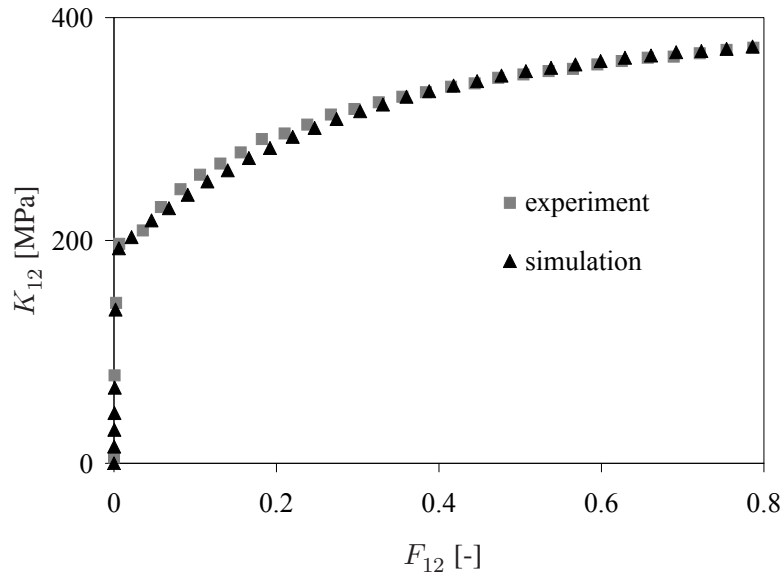


Figure 4.11: Comparison of the experimental monotonic simple-shear data with the corresponding identified model prediction.  $K_{12}$  represents the relevant shear component of the Kirchhoff stress and  $F_{12}$  represents the relevant component of the deformation gradient.

The isotropic hardening parameters so determined are then used as starting values to identify the isotropic-kinematic hardening model parameters using both monotonic and reverse simple-shear test data. The results of this are shown in Table 4.2 (right). The quality of the model identification can be judged via comparison with the fit data as shown for the current combined case in Figure 4.12. As can be seen in Figures 4.11 and 4.12, we use the experimentally-determined components of the deformation gradient  $\mathbf{F}$  to parameterize the experimental data for the model identification procedure. This is in contrast to the standard practice of using the accumulated equivalent inelastic deformation  $\alpha_P$  for this purpose, which is a model quantity and therefore not experimentally-determined. Note that these parameterizations are not equivalent. This can also be seen from the fact that one obtains different model parameter values than those in Table 4.2 when using  $\alpha_P$  in this way. For example, in the combined hardening case, one obtains  $c_r = 2.96$ ,  $s_r = 219.37$ ,  $c_x = 15.19$ ,  $s_x = 139.63$  instead of the values shown in Table

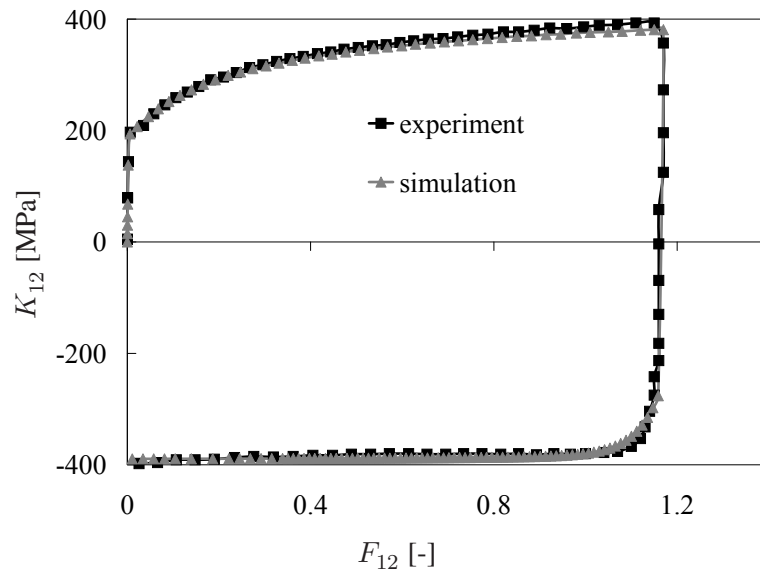


Figure 4.12: Comparison of the experimental reverse simple-shear data with the corresponding identified model prediction.

4.2, as well as a poorer fit.

Before we proceed to the identification of the complete hardening model, it is instructive to compare the predictions of the identified standard combined (i.e., isotropic-kinematic) hardening model for orthogonal tension-shear loading with the corresponding test data as represented by path 1 in Figure 4.4. This is done in Figure 4.13. Not surprisingly, the model predicts

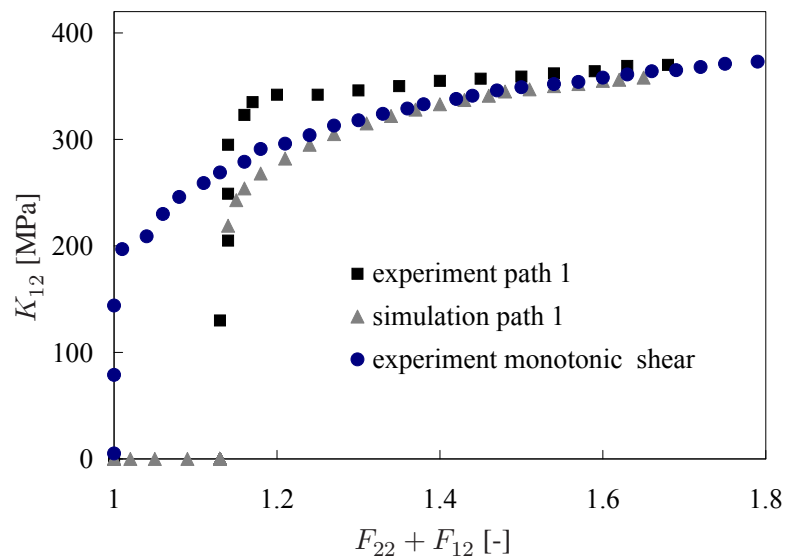


Figure 4.13: Comparison of the predictions of the identified standard combined (i.e., isotropic-kinematic) hardening model for forward simple shear and orthogonal tension-shear with corresponding experimental results from path 1 in Figure 4.4.

no cross hardening. Optically, one might be tempted to identify the prediction of the identi-

fied combined isotropic-kinematic model with case 4 or 5 in Figure 4.4. Since these represent different paths in either strain or stress space, however, they are not directly comparable.

|       | Value   | Units |
|-------|---------|-------|
| $s_r$ | 254.519 | MPa   |
| $c_r$ | 4.481   |       |
| $s_x$ | 90.896  | MPa   |
| $c_x$ | 32.695  |       |
| $s_d$ | 0.0     |       |
| $c_d$ | 19.712  |       |
| $s_l$ | -0.863  |       |
| $c_l$ | 5.0     |       |

Table 4.3: Identified hardening model parameter values for LH800 for isotropic-kinematic-cross hardening model parameter values determined from monotonic shear, cyclic shear, and orthogonal tension-shear, test data.

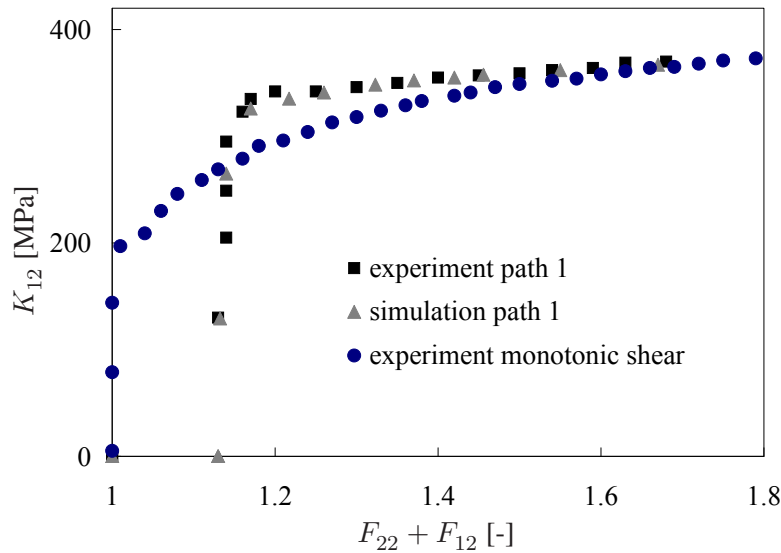


Figure 4.14: Comparison of identified isotropic-kinematic-cross hardening model behavior with experimental data for monotonic simple-shear and orthogonal tension-shear test data corresponding to strain path 1 in Figure 4.4.

Consider lastly the identification of the isotropic-kinematic-cross (i.e., complete) hardening model. Again, this is done with the help of the identified parameter values for the isotropic-kinematic case as starting values. In this way, the complete model is fit to monotonic shear, cyclic shear, and orthogonal tension-shear, test data. In particular, the test data of path 1 in Figure 4.4 is added to the previous monotonic shear and cyclic shear data sets. As with  $c_r$  and  $c_x$ , the saturation rates  $c_d$  and  $c_l$  associated with cross hardening are constrained to be greater than zero in the fit. On the other hand, as with  $s_r$  and  $s_x$ ,  $s_d$  and  $s_l$  may be positive or negative. Since the values for  $s_d$  determined in this way were on the order of  $10^{-3}$ , this parameter was set to zero in the final fits, resulting in the parameter values for the complete model shown in Table



4.3. A comparison of the corresponding experimental data and model fit is shown in Figure 4.14.

#### 4.4.2 Uniaxial tension-compression test

The identification procedure adopted here is the same as for the simple shear tests. Since the uniaxial tension and tension-compression tests are homogeneous, therefore one element simulation is used. The identification procedure begins by using uniaxial tension test data to identify the Voce isotropic hardening model alone, the results of the fit are shown in table 4.4 (left). The quality of the fit can be judged via the comparison of fitted model with the data in Figure 4.15. The isotropic hardening parameters just identified are used as starting value to identify the combined isotropic-kinematic hardening model using both uniaxial tension and uniaxial tension-compression test data. The comparison of experiment and simulation for this identification is presented in Figure 4.16. The results are shown in Table 4.4 (right). Since no orthogonal test data is available for this type of test, we restricted ourselves to the identification of combined isotropic-kinematic hardening model.

|               | Value   | Units |
|---------------|---------|-------|
| $\sigma_{Y0}$ | 335.745 | MPa   |
| $s_r$         | 281.034 | MPa   |
| $c_r$         | 13.069  |       |

|               | Value   | Units |
|---------------|---------|-------|
| $\sigma_{Y0}$ | 335.745 | MPa   |
| $s_r$         | 238.62  | MPa   |
| $c_r$         | 8.445   |       |
| $s_x$         | 77.747  | MPa   |
| $c_x$         | 12.155  |       |

Table 4.4: Identified hardening model parameter values for LH800. Left: isotropic hardening parameter values determined from uniaxial tension test data alone. Right: isotropic-kinematic hardening parameters determined from uniaxial tension and uniaxial tension compression test data.

#### 4.4.3 Pure bending test

Unlike the afore mentioned reverse shear and tension-compression tests, the pure bending test is inhomogeneous. Therefore, here, for the identification the specimen has to be modeled. This was done using 3D solid/brick elements. The mesh size was chosen by conducting a mesh convergence analysis. Figure 4.17 demonstrates the sensitivity of number of through thickness elements used over the bending moment during the pure bending test. Figure 4.17 (left) shows the bending moment versus bending angle results for variable number of through thickness elements and Figure 4.17 (right) shows the bending moment at the end of 1st cycle versus number of thickness elements. The converged solution is obtained for 9 elements in thickness direction.

The identification procedure begins by using bending test data to identify the Voce isotropic hardening model alone, the results of the fit are shown in table 4.5 (left). The quality of the fit can be judged via the comparison of fitted model with the data in Figure 4.18. The identification of parameters for the combined isotropic-kinematic hardening is conducted using the three

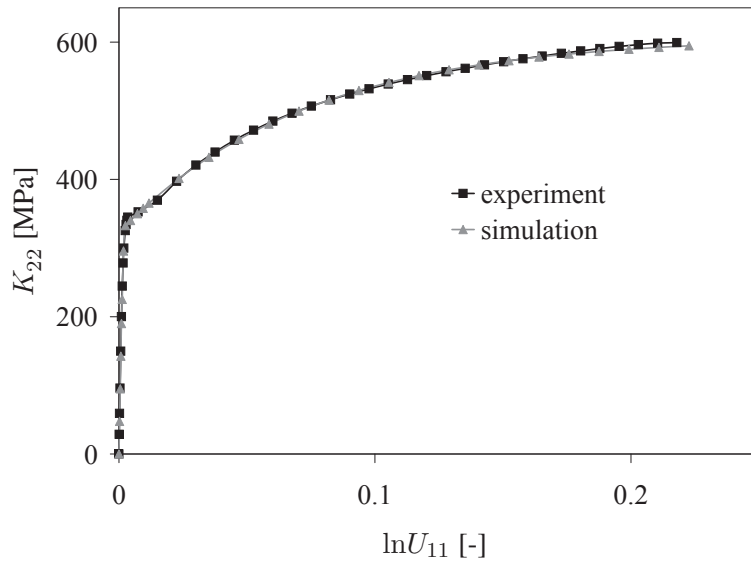


Figure 4.15: Comparison of the experimental uniaxial tension data with the corresponding identified model prediction.

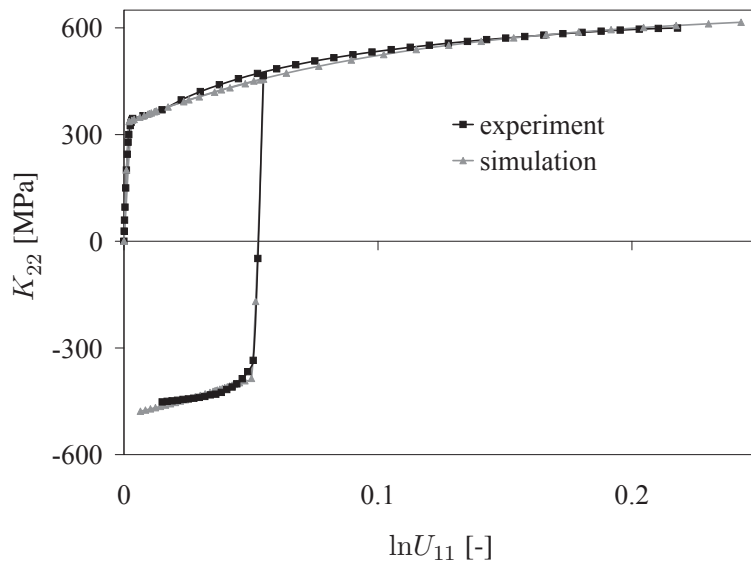


Figure 4.16: Comparison of the experimental uniaxial tension compression data with the corresponding identified model prediction.

cycles of pure bending test. The results of the identification are shown in Table-4.5 (right). The quality of the fit can be judged with comparison to the experimental data and is presented in Figure 4.19.

The value of the evolution rate  $c_x$  of kinematic hardening is significantly higher here ( $c_x = 324.735$ ) than for the previous tests, i.e. reverse simple shear ( $c_x = 32.695$ ) and uniaxial tension-compression tests ( $c_x = 12.155$ ). This could be due to the fact that the gradual change of the bending moment versus bending angle curve (Figure 4.10) after re-yielding compared to the

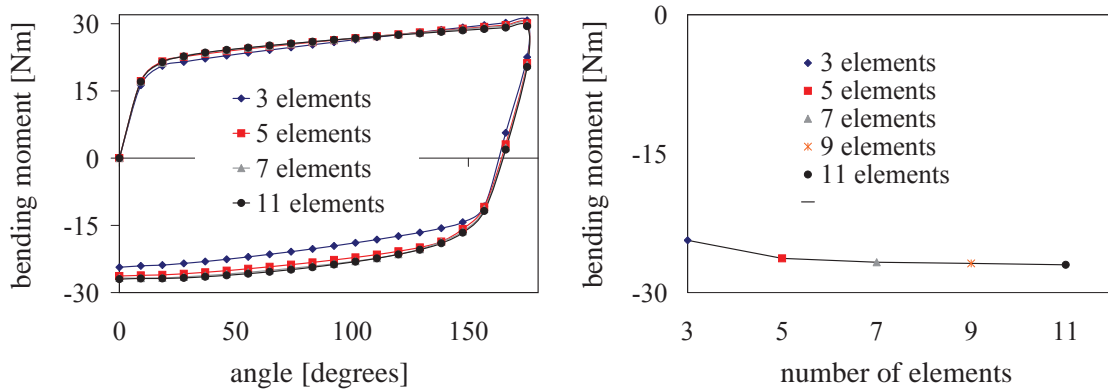


Figure 4.17: Result of mesh convergence analysis for thickness direction. Left: for one cycle of bending test. Right: bending moment at the end of first cycle.

|               | Value  | Units |
|---------------|--------|-------|
| $\sigma_{Y0}$ | 355.1  | MPa   |
| $s_r$         | 160.02 | MPa   |
| $c_r$         | 22.088 |       |

|               | Value   | Units |
|---------------|---------|-------|
| $\sigma_{Y0}$ | 328.863 | MPa   |
| $s_r$         | 140.281 | MPa   |
| $c_r$         | 1.578   |       |
| $s_x$         | 95.368  | MPa   |
| $c_x$         | 324.735 |       |

Table 4.5: Identified hardening model parameter values for LH800 determined from pure bending test data. Left: isotropic hardening parameter values determined. Right: isotropic-kinematic hardening parameters.

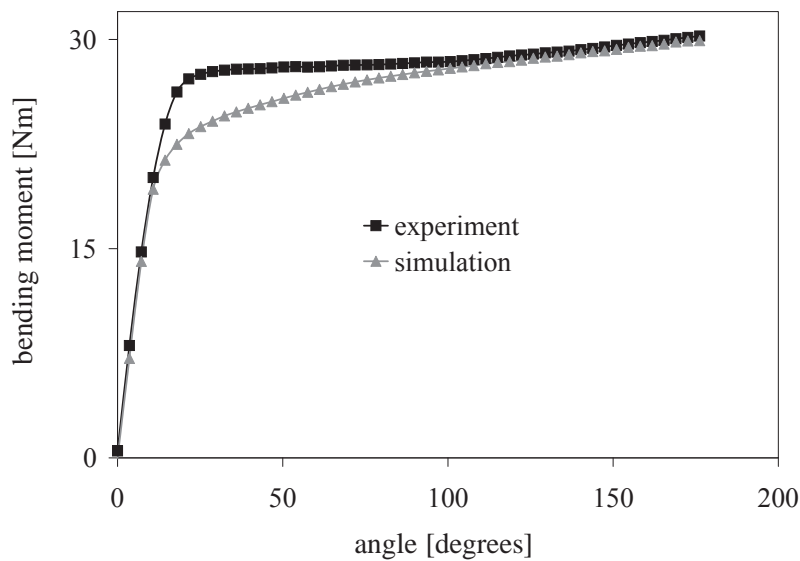


Figure 4.18: Comparison of the experimental bending test data with the isotropic hardening model prediction.

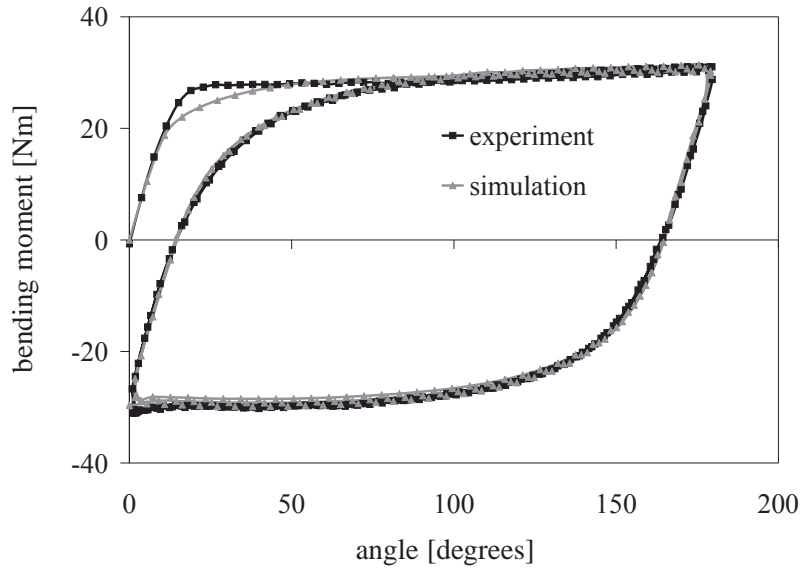


Figure 4.19: Comparison of the experimental bending test data with the isotropic-kinematic hardening model prediction.

relatively sharp change of the stress versus strain curve (Figure 4.7) after reyielding is yielded with higher value of  $c_x$  and relatively lower value of  $s_x$ . In addition, the saturation value  $s_r$  for isotropic hardening is about 100 MPa smaller than in the uniaxial tension-compression and reverse simple shear case. This could be attributed to the fact of a considerably smaller amplitude of applied strain. Thus, smaller total levels of stress are achieved in the pure bending test compared to the other tests.

As already mentioned, the prestrained specimen are then cut down into the two small samples. One of those is used for another reversed pure bending test, and the second is used for the orthogonal pure bending test. We now carry out a small validation test for the identified combined isotropic-kinematic hardening model parameters by predicting the reverse bending test data obtained from the small specimen. The comparison of the simulation with the experiment shows a good agreement, as shown in Figure 4.20 (left).

We also compare the predictions of the identified standard combined isotropic-kinematic hardening model for the orthogonal loading with the corresponding test data which is represented as orthogonal test in Figure 4.4 (right). The comparison of the simulation with the experiment is presented in Figure 4.20 (right). Note that in the case shown in Figure 4.20 (right) the sample is removed from the clamps after cyclic bending and then rotated 90deg. After the rotation cyclic bending is applied. This represents a change in loading path which is neither a reversal nor a “pure” orthogonal change. Orthogonal loading path here is understood as a change in loading path where two subsequent directions of plastic flow  $N_{P1}$  and  $N_{P2}$  are orthogonal. The effect of cross hardening in this test is relatively small due to this and due to the fact that the amplitude of pre-straining is relatively small. Consequently, the combined isotropic-kinematic hardening model which is not capable of modeling cross-hardening shows good agreement with the experiment. From another point of view, at this level of pre-strain, oriented dislocation microstructures responsible for cross hardening have not yet developed. This is also true for other

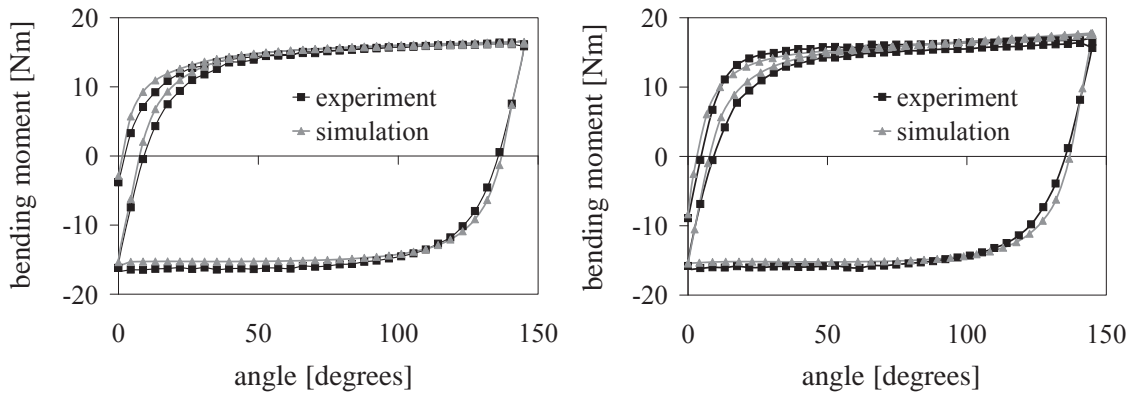


Figure 4.20: Comparison of the predictions of the identified standard combined (i.e., isotropic-kinematic) hardening model. Left: for reverse bending test. Right: for orthogonal bending test.

steels. In the case of IF steel DC06 and SUS 304, no noticeable cross hardening occurs after pre-straining up to approximately  $10^{-2}$  and  $10^{-3}$  respectively (Ishikawa, 1997; Noman et al., 2010). So one can say that the orthogonal bending test may generally be used to identify the cross hardening parameters as done by Boers et al. (2010), but for the case of steel LH800 the cross hardening is not activated for the given amount of pre-strain.

## 4.5 Comparison of responses of tests with the responses of simulations

In this section a comparison is performed between the experimental and the simulated responses to investigate the influence of the test data used for the identification on the material model parameters. To perform such a comparison, each test is simulated using the identified combined isotropic-kinematic hardening parameters based on the other two tests, and the simulated responses are then compared with the experimental response.

### 4.5.1 Uniaxial tension-compression test

The uniaxial tension-compression test is simulated with the combined isotropic-kinematic hardening parameters identified from the reverse shear test and the pure bending test. Figure 4.21 shows the comparison between the experiment and the finite element simulations. For the simulation based on the parameters identified from the reverse simple shear test, the agreement is good in tension phase. To the contrary, the agreement in the compression phase is not so good. For the simulation based on the parameters identified from the pure bending test, the agreement is not good as it starts to saturate at a smaller strain. The agreement gets better for the compression part. The improved agreement in the compression phase also points out that the pure bending test is kinematic hardening dominated and that there is not enough inelastic deformation/strain hardening to saturate to the saturation parameters  $s_r$  of the Voce isotropic hardening rule, see equation 7. In addition the saturation value  $s_r$  is smaller as stated before.

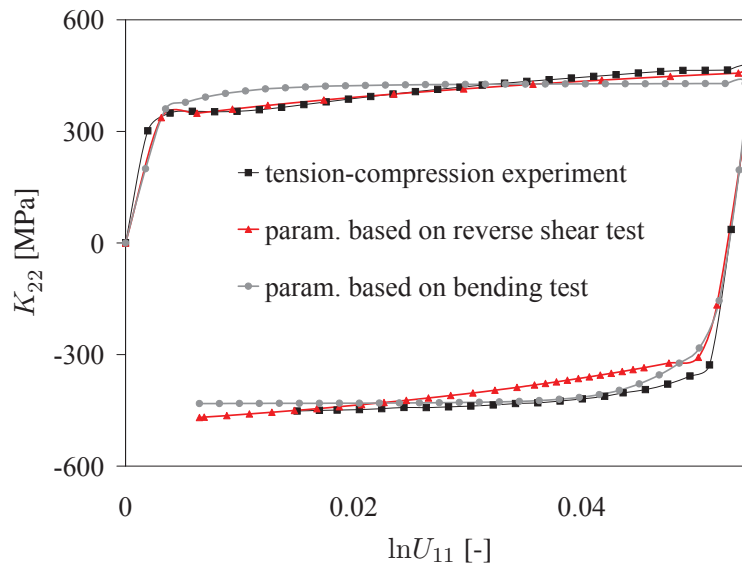


Figure 4.21: Comparison of the experimental and simulation stress-strain response. The experiment is uniaxial tension-compression and simulations are performed using the parameters identified from the reverse shear test and the pure bending test respectively.

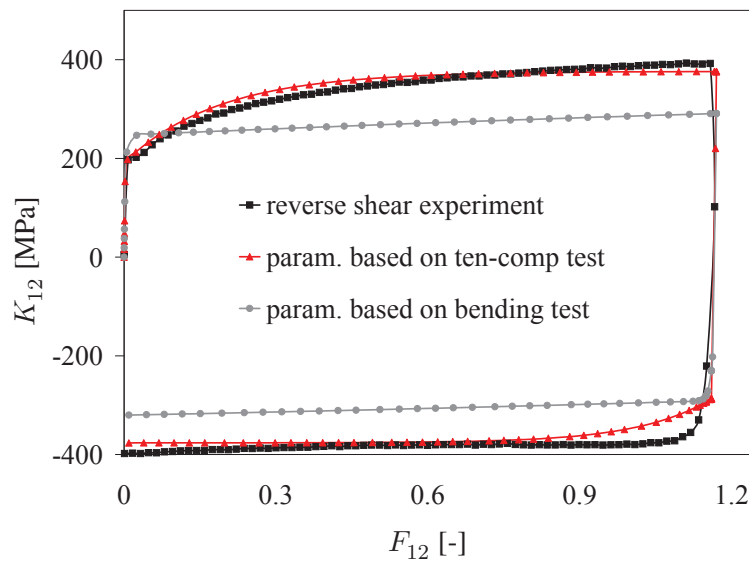


Figure 4.22: Comparison of the experimental and simulation stress-strain response. The experiment is the reverse shear test and simulations are performed using the parameters identified from the uniaxial tension-compression test and the pure bending test respectively.

#### 4.5.2 Reverse shear test

The reverse shear test is simulated with the combined isotropic-kinematic hardening parameters identified from the uniaxial tension-compression test and the pure bending test. Figure 4.22 shows the comparison between the experiment and the finite element simulations. For the simulation based on the parameters identified from the tension-compression test, the agreement

with the shear experiment is very good in the forward shear phase. The behavior observed after re-yielding is not accurately captured by this set of data. However for large levels of reverse straining the agreement gets better as the hardening in the material saturates. For the simulation of the reverse shear experiment based on the parameters identified from the pure bending test, only the level of stress at yielding and re-yielding is captured accurately. There is no increase of the stress after initial yielding and re-yielding as in the experiment meaning that the general agreement is very poor. This could be understood by recalling the low value of  $s_r$ , the saturation value of isotropic hardening and also low value of  $c_r$ , the rate of isotropic hardening yielded by the identification based on the pure bending test data.

#### 4.5.3 Pure bending test

The pure bending test is simulated with the combined isotropic-kinematic hardening parameters identified from the uniaxial tension-compression test and the reverse shear test. Figure 4.23 shows the comparison between the experiment and the finite element simulations for the first cycle of bending-unbending. The agreement between the simulations and the experiment is good in both cases, however differences can be observed at the beginning of the hardening in the loading phase and for the reyielding after load reversal.

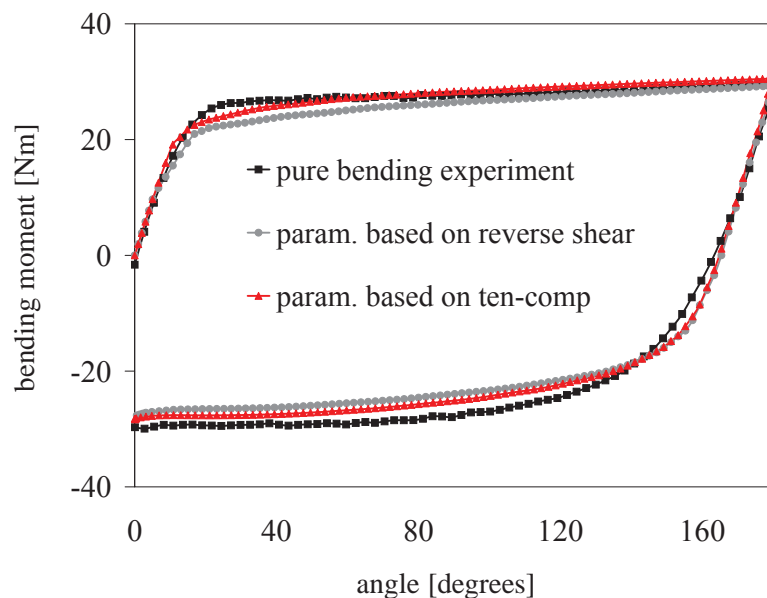


Figure 4.23: Comparison of the experimental and simulation bending moment versus bending angle response. The experiment is the pure bending test and simulations are performed using the parameters identified from the uniaxial tension-compression test and the reverse shear test respectively.

## 4.6 Application to springback prediction (during draw-bending test)

The draw-bending test is exemplary for a number of sheet forming operations, yet has the advantage of simplicity. Such a test is mostly used in springback prediction studies. This test is simulated here in 5 steps by analogy with the experimental procedure. In the first step, the

sheet metal strip is pre-bent to 90 degrees using the bending tool. Secondly, the bending tool is removed. Thirdly, the strip is clamped into the machine at both ends and pulled tightly over a rubber roller from both ends, subjecting it to tension. The actual test begins with the strip being pulled from right to left over the roller under tension, such that it experiences bending-unbending. Since the roller moves with the strip, there is little or no friction between them. In the last step, the strip is unclamped and the resulting springback process is simulated. During the draw-bending test, the bending-unbending represents the loading path of load-reversal type in which isotropic and kinematic hardening are the main hardening mechanisms. The finite element model used is based on conventional shell elements. For efficiency, the symmetry of the strip (Figure 4.24) has been exploited in the simulation. The minimal friction taking place between the roller and strip has been modeled in ABAQUS via the definition of a “Contact Property” of “Friction” type.

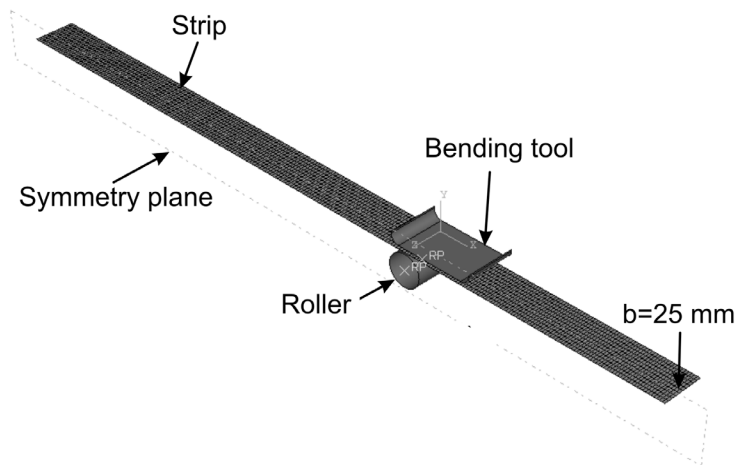


Figure 4.24: Finite element model for draw-bending test

As already mentioned, three sets of combined isotropic-kinematic hardening parameters are available obtained from the experiments, namely uniaxial tension-compression test, reverse shear test and reverse pure bending test. A simulation is performed for each set of parameter using ABAQUS. The simulation is performed using the combined isotropic-kinematic hardening parameters, since isotropic hardening alone over-predicts the springback, as pointed out by Svendsen et al. (2006); Wang et al. (2005). A comparison of the experimental and simulation results for springback of the strip using roller of radii of 10 and 15 mm is shown in Figures 4.25 and Figure 4.26.

As can be seen, the agreement is very good between the predicted springback of the simulation using the parameters based on the tension-compression test and the experiment. The simulation based on the parameters identified from the reverse shear test data under predicts the amount of springback a little. The amount of springback predicted by the simulation, based on the the parameters identified from the pure bending test, is much smaller than in the experiment. This confirms the argument presented in Section 6 that due to small level of the amplitude in straining and thus a small total level of strain isotropic hardening is under represented by the



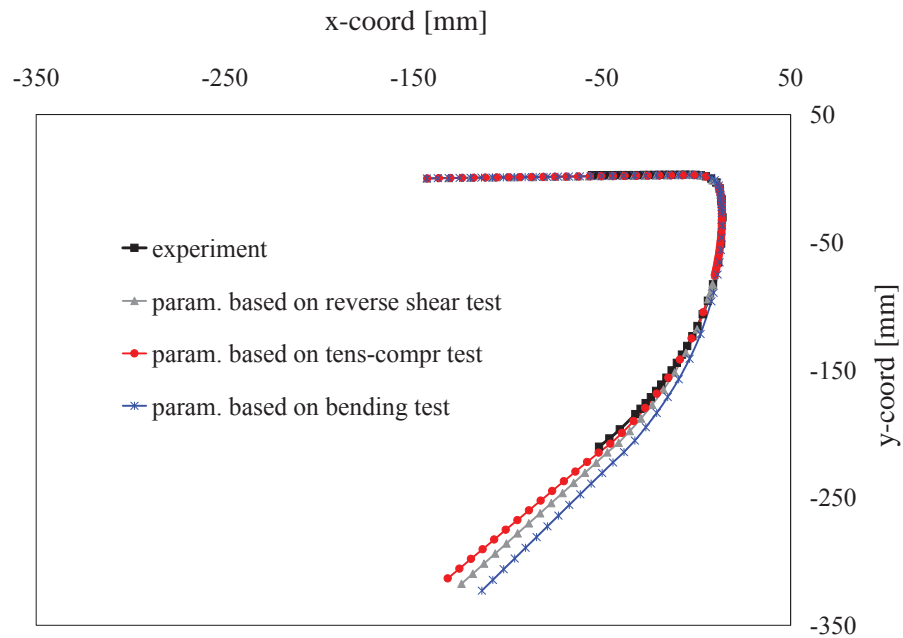


Figure 4.25: Comparison of experimental and simulation results for roller radius 10 mm.

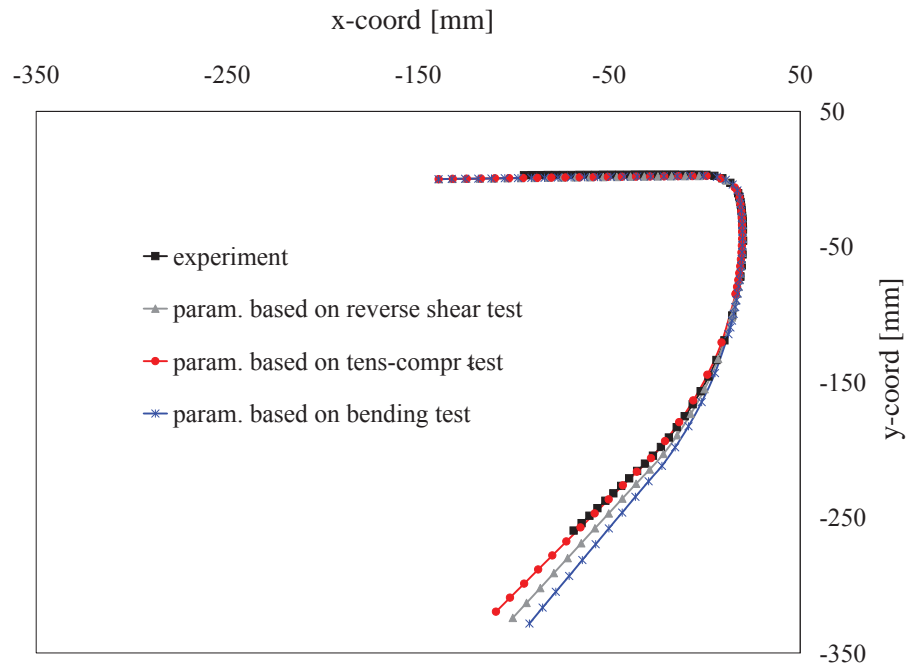


Figure 4.26: Comparison of experimental and simulation results for roller radius 15 mm.

pure bending based data. This in turn leads in general to the prediction of lower level of stress. With constant elastic parameters, this results in a smaller amount of predicted springback for this type of data. To demonstrate the importance of complete isotropic-kinematic-cross hardening model, we now compare the experimental results for springback with the corresponding simulation results based on the combined isotropic-kinematic hardening model (parameters are iden-

tified using the simple reverse shear test) and the complete isotropic-kinematic-cross hardening model (parameters are identified using the simple reverse shear and orthogonal test). Figure 4.27 shows the comparison of the simulation and experimental results for the roller radius of 10 mm. The agreement is even better in the case of the complete isotropic-kinematic-cross hardening model than of the combined isotropic-kinematic hardening model. The complete isotropic-kinematic-cross hardening model is computationally expensive and takes approximately nine hours, compared to the combined isotropic-kinematic hardening model that takes one and half hours for the complete simulation. This emphasizes the fact that, indeed, the complete isotropic-kinematic-cross hardening model minutely increases the accuracy of the springback prediction but that the computation time is six times higher.

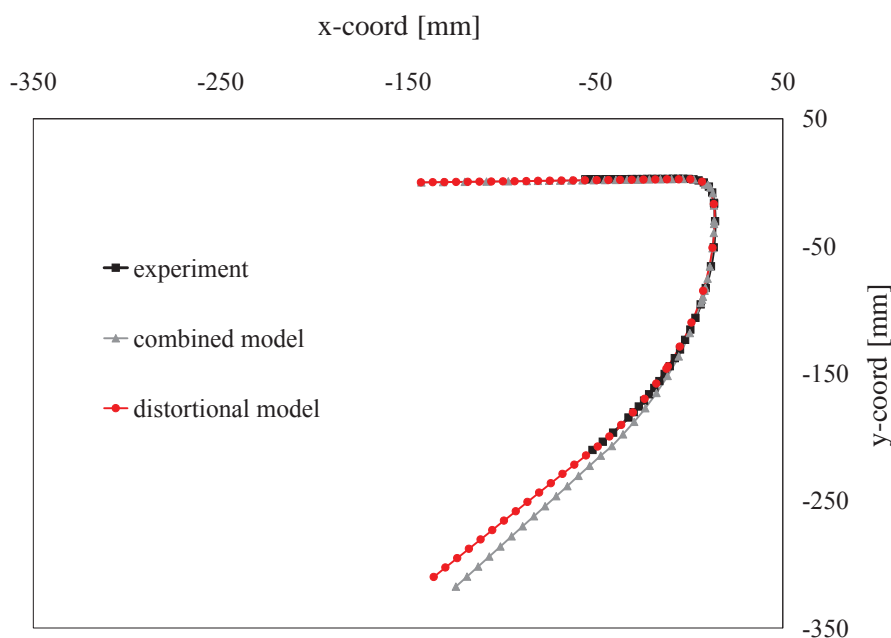


Figure 4.27: Comparison of experimental and simulation results using the combined and the distortional hardening model for roller radius 10 mm.

## 4.7 Summary and Conclusions

Uniaxial tension-compression, simple reverse shear and pure bending tests have been performed on the sheet steel LH800. The material was characterized as initially isotropic due to a lack of strong texture. The hardening behavior has been described by the recently presented material model that is able to capture not only a shift of the yield surface and its proportional expansion as in the case of conventional combined hardening, but is also able to account for an evolving yield surface shape and so distortional hardening. Three sets of material parameters were identified with uniaxial tension-compression test, pure bending test and simple reverse shear test together with orthogonal tension-shear test. Numerical simulation of each test has been performed using the identified parameters from the other two tests. Using these simulation responses, a comparison is performed between the experimental and the simulation responses to

investigate the influence of the test data used for the identification on the material model parameters. The comparison shows that the simulation responses based on the parameters identified from the reverse shear test and the uniaxial tension compression test agree well with the experimental responses of the experiment not used for identification, i.e. the reverse shear and pure bending test for the tension-compression based data and the tension-compression and pure bending test for the reverse shear based data. However, for the simulation responses of the shear test and the tension-compression test using the parameters identified from the pure bending test, a divergence is observed by comparing them with the experimental test responses. After conducting the comparison study, a more realistic metal forming process, i.e. draw-bending test, was simulated that is used widely in springback studies. The prediction shows a good agreement when the combined isotropic-kinematic hardening model parameters obtained from the uniaxial tension-compression test are used. A slight difference is noticed when the combined isotropic-kinematic hardening model parameters obtained from the simple reverse shear test are used. Prediction of the springback is poor when the parameters obtained from the bending test are taken. It can therefore be concluded that the uniaxial tension-compression test and the reverse shear test have advantages over the pure bending test, as the level of strains generated in these tests are higher and the parameters identified from these tests may predict the responses of the experiments that involve large levels of strains better. In addition, the hardening behavior of the material under investigation, ferritic steel LH800, is represented more accurately by the sets of parameters identified from the tension-compression or reverse shear tests. This leads to the fact that the amount of springback predicted by simulations using such data is also most accurate. This is due to the effect that the level of stress predicted by a model directly influenced the amount of springback for constant elastic behavior. Furthermore, the complete isotropic-kinematic-cross hardening model predicts the amount of springback more accurately as compared to the combined isotropic-kinematic hardening model, but over the cost of more computation time which is six times higher than the computation time required for the simulation using the combined isotropic-kinematic hardening model.



## Chapter 5

# Numerical and physical factors affecting the springback simulation for sheet metal forming

**Abstract**– Springback is a phenomenon which is vital in the structural component's accuracy. It usually produces deviation from the desired shape and raises problems in the assembly of different parts. Hence, it becomes necessary to simulate the forming process and predict springback numerically beforehand to meet the requirements. In general, the numerical simulation of the metal forming process and springback prediction is influenced by two different kinds of parameters: physical and numerical. The purpose of the current work is the investigation of a number of these parameters, both physical and numerical, on the metal forming process and springback prediction. The study has been carried out using the commercial finite element codes ABAQUS/Standard and LS-DYNA. In particular, the influence of numerical parameters such as the finite element formulation, mesh size and integration scheme and the effect of physical parameters, e.g. back force, tool radius, friction coefficient and material model are examined.

### 5.1 Introduction

Springback is defined as the undesired change in shape of the part upon removal of the forming load at the end of forming process. It usually produces deviation from the desired shape and raises the problems in assembly of different parts, thus extra effort is required to compensate this undesired change in shape. Despite this, accurate prediction of springback is a growing problem with the use of high strength and low modulus materials. Hence it becomes necessary to predict springback beforehand to meet manufacturer requirements to use lighter and stronger materials.

The prediction of springback was initially carried out using analytical approaches. Several mathematical models have also been proposed to describe and predict springback for simple geometries, (e.g. by Wenner (1983), Baba and Tozawa (1964), Chan (1999), Levy (1984), Queener and Angelis (1968), Shaffer and House (1955), Li et al. (2002), Ueda et al. (1981) and Yuen (2000)). With the increase in computational power and development of numerical methods, the finite element method becomes an efficient tool and obvious choice to simulate the metal forming processes and predicting springback. Many researchers used FEM (e.g Lee and Yang (1998), Kleiner et al. (2005), Chen et al. (2005), Wagoner and Li (2005)) to simulate the forming processes and to predict the springback. The availability of commercial codes for the simulation of forming processes (e.g., LS-DYNA, ABAQUS, PAM-STAMP, AutoForm, DYNAform, Stampack, etc.) has greatly facilitated the numerical simulation of springback. Several experimental geometries have been studied that could easily describe the springback

phenomenon, e.g., cylindrical tool bending (e.g., Martin and Tsang (1966)), V-die bending (e.g., Asnafi (2000), Z. Hu and Teodosiu (1992), Tan et al. (1992)), U-channel forming (e.g., Huang and Leu (1995)) and flanging (e.g., Davies and Liu (1984)).

In general, the numerical simulation of the metal forming process and springback prediction is influenced by two different kinds of parameters: physical and numerical. The physical group of parameters includes both material properties, such as isotropic and kinematic hardening, Bauschinger effect, distortional hardening, elastic and plastic anisotropy (Carden et al. (2002), Laurent et al. (2009), Geng and Wagoner (2002), Oliveira et al. (2007) and Li et al. (2002), Eggertsen and Mattiasson (2009, 2010), and Wang et al. (2006) ) and process characteristics sensitiveness, such as sheet thickness, friction coefficient, blank holder force, tool geometry (e.g. radius), temperature and unloading procedure (Li et al. (2002) and Wang et al. (2005)). The numerical parameters influencing springback are the type of element, order and integration scheme of the finite element, as well as the shape, size and the finite element mesh refinement ( Li et al. (2002), Xu et al. (2004), Meinders et al. (2008)). The purpose of the current work is the investigation of a number of these parameters, both physical and numerical, on the basis of the combined hardening model which has been implemented in the commercial finite element codes ABAQUS/Standard and LS-DYNA and comparison of the results of both FE codes. To this end, a relatively “simple” forming process, draw-bending test, is considered. The draw-bending test (e.g., Carden et al. (2002), Kleiner et al. (2005), Li et al. (2002) and Wang (2004)) mimics closely the typical stamping deformation of the sheet metal, during which it is drawn, stretched, bent and unbent over a die radius entering a typical die cavity. In particular, bending and unbending represent a loading path change of the load-reversal type in which isotropic and kinematic hardening are the principle hardening mechanisms.

The paper begins (Section 5.2) with a brief review of the material model used in the present work. In order to focus on numerical and physical parameters (e.g., contact and friction), attention is restricted in this model for simplicity to isotropic von-Mises yielding as well as to isotropic and kinematic (i.e., classical combined) hardening. After a brief review of the issues of element formulation (Section 5.4) as well as the contact and friction algorithm (Section 5.5), attention is focused on the investigation of the dependence of the solution on the number of elements, the element formulation, the number of integration points, as well as on contact and friction modeling (Section 5.6). Some additional physical aspects of the simulation (e.g., effect of back force) are also investigated (Section 5.7). The work ends with a brief summary and conclusions (Section 5.8).

## 5.2 Material Model

The most widely used hardening model to simulate the metal forming processes and predicting springback is the standard combined hardening model. Such models are intended to represent the hardening behavior particularly during cyclic loading or during a strain-path reversal. For more complex loading histories, additional hardening mechanisms resulting in directional hardening effects generally need to be taken into account (Noman et al. (2010), Teodosiu and Hu (1998) and Wang et al. (2008)). Since we are focusing here, however, on numerical issues, attention is restricted for simplicity to combined hardening.

The formulation of the current model is carried out in the framework of the standard inelastic multiplicative decomposition  $\mathbf{F} = \mathbf{F}_E \mathbf{F}_P$  of the deformation gradient  $\mathbf{F}$  (Simo and Hughes (e.g., 1998)). Such a decomposition arises naturally, e.g., in the context of the modeling of  $\mathbf{F}_P$  as a change of local reference configuration Svendsen (2001). In this context, one obtains in particular the result

$$\mathbf{R}_E^T \mathbf{L}_E \mathbf{R}_E = \mathbf{R}_E^T \mathbf{L} \mathbf{R}_E - \mathbf{U}_E \mathbf{L}_P \mathbf{U}_E^{-1} = \mathbf{R}_E^T \dot{\mathbf{R}}_E + \dot{\mathbf{U}}_E \mathbf{U}_E^{-1} \quad (5.1)$$

via the right polar decomposition  $\mathbf{F}_E = \mathbf{R}_E \mathbf{U}_E$  of  $\mathbf{F}_E$  for the back-rotated form of  $\mathbf{L}_E := \dot{\mathbf{F}}_E \mathbf{F}_E^{-1}$  in terms of  $\mathbf{L} := \dot{\mathbf{F}} \mathbf{F}^{-1}$  and  $\mathbf{L}_P := \dot{\mathbf{F}}_P \mathbf{F}_P^{-1}$ . For the current case of polycrystalline metals and small elastic strain, we have

$$\begin{aligned} \mathbf{U}_E &\approx \mathbf{I} + \ln \mathbf{U}_E, \\ \dot{\mathbf{U}}_E \mathbf{U}_E^{-1} &\approx \overline{\ln \mathbf{U}_E}. \end{aligned} \quad (5.2)$$

Substituting these into (5.1), and taking the symmetric and skew-symmetric parts of the result, one obtains the evolution relations

$$\begin{aligned} \overline{\ln \mathbf{U}_E} &= \mathbf{R}_E^T \mathbf{D} \mathbf{R}_E - \mathbf{D}_P, \\ \dot{\mathbf{R}}_E &= \mathbf{W} \mathbf{R}_E - \mathbf{R}_E \mathbf{W}_P, \end{aligned} \quad (5.3)$$

for  $\ln \mathbf{U}_E$  and  $\mathbf{R}_E$ , respectively, in the incremental context.  $\mathbf{D} := \text{sym}(\mathbf{L})$  is the continuum rate of deformation,  $\mathbf{D}_P := \text{sym}(\mathbf{L}_P)$  its inelastic counterpart,  $\mathbf{W} := \text{skw}(\mathbf{L})$  the continuum spin, and  $\mathbf{W}_P := \text{skw}(\mathbf{L}_P)$  the plastic spin. Restricting the current formulation to the case of sheet metal forming, it is reasonable to assume that the texture in these materials achieved during rolling remains largely unchanged during forming processes like tension, compression, simple shear, cyclic simple shear, and combinations of these. In this case,  $\mathbf{W}_P$  is negligible, and the evolution of  $\mathbf{R}_E$  depends only on  $\mathbf{W}$ , in which case it reduces to a purely kinematic quantity (i.e., the Jaumann rotation). In addition, focusing in this work on the material behavior of sheet metal during forming below the forming limit, we assume for simplicity that damage or any other process resulting in inelastic volume changes are negligible. In this case, plastic incompressibility  $\det(\mathbf{F}_P) = 1$  pertains, implying  $\text{tr}(\mathbf{D}_P) = 0$  and  $\mathbf{D}'_P = \mathbf{D}_P$  in the incremental context.

Since the elastic range and elastic strain are small, any texture effects from rolling leading to an anisotropic elastic behavior are assumed negligible. In this case, the isotropic form

$$\mathbf{M} = \kappa \text{tr}(\mathbf{E}_E) \mathbf{I} + 2\mu \mathbf{E}'_E \quad (5.4)$$

is assumed for the Mandel stress  $\mathbf{M}$  in terms of the elastic strain  $\mathbf{E}_E := \ln \mathbf{U}_E$ , bulk modulus  $\kappa$ , shear modulus  $\mu$ , and deviatoric part  $\mathbf{E}'_E$  of  $\mathbf{E}_E$ . Lastly, again in the framework of small elastic strain,  $\mathbf{M}$  and  $\mathbf{R}_E$  determine the Kirchhoff stress  $\mathbf{K}$  via

$$\mathbf{K} = \mathbf{R}_E \mathbf{M} \mathbf{R}_E^T. \quad (5.5)$$

Consequently, in contrast to  $\mathbf{K}' = \mathbf{R}_E \mathbf{M}' \mathbf{R}_E^T$ ,  $\text{tr}(\mathbf{K}) = \text{tr}(\mathbf{M})$  of  $\mathbf{K}$  is independent of  $\mathbf{R}_E$ .

In this framework, then, the material behavior of polycrystalline sheet metal during forming processes below the forming limit is predominantly determined by a changing dislocation microstructure and attendant evolving anisotropic yield behavior. Besides a shift of the yield surface and its proportional expansion as in the case of conventional combined hardening, the current model also accounts for an evolving yield surface shape and so distortional hardening. In the current notation, the model is written simply in the form

$$\phi = \sqrt{(\mathbf{M} - \mathbf{X}) \cdot \mathcal{A}(\mathbf{M} - \mathbf{X})} - \sigma_{Y0} - r \quad (5.6)$$

in terms of the initial yield stress  $\sigma_{Y0}$ .  $\mathcal{A}$  is the fourth order anisotropy tensor, here set to the fourth order identity. For the class of materials under consideration, the saturation (i.e., Voce) form

$$\dot{r} = c_r (s_r - r) \dot{\alpha}_P \quad (5.7)$$

for the evolution of  $r$  is appropriate, driven by that of the equivalent inelastic deformation  $\alpha_P$ . Here,  $c_r$  represents the rate, and  $s_r$  the value, for saturation associated with  $r$ . Since  $\sigma_{Y0}$  is the initial yield stress (i.e., for  $\alpha_P = 0$ ), the initial value  $r_0$  of  $r$  is zero. In the current rate-independent context,  $\alpha_P$  is determined as usual by the consistency condition. Analogous to isotropic hardening, kinematic hardening is modeled via the saturation (i.e., Armstrong-Frederick) form

$$\dot{\mathbf{X}} = c_x (s_x \mathbf{N}_P - \mathbf{X}) \dot{\alpha}_P \quad (5.8)$$

for the evolution of  $\mathbf{X}$  depending on corresponding (constant) saturation rate  $c_x$ , (constant) saturation magnitude  $s_x$ , as well as the (variable) direction  $\mathbf{N}_P := \mathbf{D}_P / |\mathbf{D}_P|$  of the rate of inelastic deformation

$$\mathbf{D}_P = \dot{\alpha}_P \partial_{\mathbf{M} - \mathbf{X}} \phi, \quad (5.9)$$

which is modeled here in associated form. The initial value of  $\mathbf{X}$  is assumed to be zero.

The current material model was implemented in the commercial FE codes ABAQUS and LS-Dyna via the user material interfaces provided. Besides the two elasticity parameters  $\kappa$ ,  $\mu$ , this model contains 5 hardening parameters  $\sigma_{Y0}$ ,  $c_r$ ,  $s_r$ ,  $c_x$  and  $s_x$  to be identified.

### 5.3 Draw-Bending Test

In real sheet metal forming operations, the bending and unbending of the sheet metal occurs under superposed tension as the blank slides over the tool surface, under the influence of the tool/punch force. In the draw-bending test, a sheet metal strip is bent, drawn and then straightened over a die radius comparable to that of a typical die cavity. Besides simulating these, the draw-bending test still offers the necessary simplification of simplifying the boundary conditions and eliminates friction effects, allowing for a focus over the effect of the loading conditions on the material behavior, residual stress development and springback.

The test itself is carried out with the help of a servo-hydraulic mechanical test machine and a bending frame as shown in Figure 5.1. Here, two hydraulic actuators oriented orthogonal to each other control the forming of the strip. In particular, the right actuator provides a constant restraining force (i.e., the back force), while the left one moves at a constant speed. The tension force is measured by sensors attached to each actuator. At the beginning of the test, the specimen



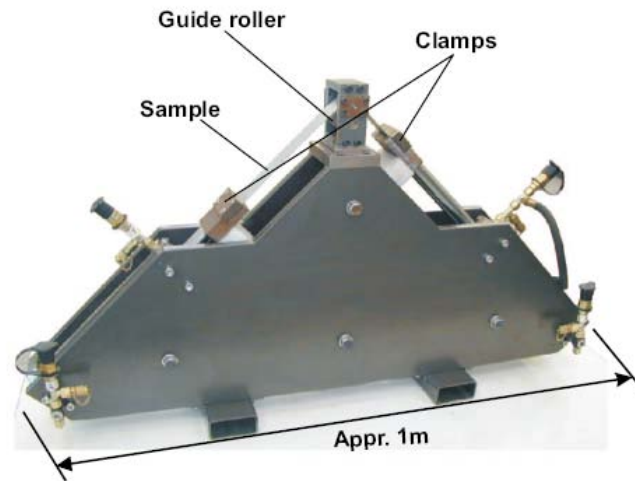


Figure 5.1: Draw-bending test machine and experimental setup, from Kleiner et al. (2005).

is first pre-bent in a right angle with a triangular punch rounded off at the corner. Then it is clamped into the machine. A tension force of 2.4 kN is applied at the left end of the strip holding the right end fixed. The strip is then drawn over the fixed roller with negligible friction under constant tension. The drawing speed was 4.5 mm/s. In this case, the sheet metal strip undergoes bending and unbending under constant tension, resulting in a load reversal in the material in the sense of bending and unbending. After the forming operation is completed, the lower grip is opened to allow the specimen to springback freely.

The complete draw-bending test is simulated here in 5 steps by analogy with the experimental procedure. As just discussed, in the experiment, the strip is first pre-bent from the initial straight form into a right angle by means of a triangular punch rounded off at the corner. This pre-bending process is idealized in the simulation by pre-bending the strip directly around the guide roller with the bending tool, resulting in the initial configuration. In the current simulation, the roller and bending tool are idealized as analytical rigid surfaces. As in the tests, the strip is 448 mm long, 50 mm wide and with a thickness of 1.6 mm. In addition, the roller, and so the bending radius is 10 mm. Due to the symmetry of the specimen, only half of the structure needs to be included in the simulation. In the second step, the bending tool is removed. Now the tension is applied at the right end of the strip in the third step. The strip is then drawn by applying a velocity at the left end under the influence of the tensile force which is applied constantly at the right end. After having been drawn, the strip is unloaded to observe its springback. In what follows we refer to bending, applying tension and then drawing steps as forming stage. Releasing the strip afterwards to get the final form is referred as springback stage.

## 5.4 Element formulations

### 5.4.1 Shell element formulations

Shell elements are used to model structures in which one dimension, the thickness, is significantly smaller than the other dimensions. In ABAQUS two types of shell elements are available: conventional shell elements and continuum shell elements. Conventional shell elements discretize a body by defining the geometry at a reference surface, in such a way that each node has displacement and rotational degrees of freedom. In the conventional shell, the thickness is defined through the section property definition. In contrast, continuum shell elements discretize an entire three-dimensional body. The thickness is determined from the element nodal geometry. Continuum shell elements have only displacement degrees of freedom. From a modeling point of view continuum shell elements look like three-dimensional continuum solids, but their kinematic and constitutive behavior is similar to conventional shell elements. Both element types allow for a variable number of integration points through the thickness.

For the metal forming simulations of interest here, large-deformation continuum and conventional shells are relevant. In the latter case, the shell element S4 (4-node doubly curved general purpose shell) is most frequently used. Each node has three displacement and three rotation degrees of freedom. Bilinear interpolation is used. A transverse shear strain field is used in the formulation and it is calculated at the element center. Besides this, S4R is a reduced integration element with stabilization control against hourglassing. The membrane behavior of this element is based on the uniform strain formulation for a 4-node quadrilateral plane-stress element. Beyond such elements, stress/displacement continuum shell elements in ABAQUS are also used in three-dimensional sheet forming analysis. These elements have displacement degrees of freedom only and are based on linear interpolation. It is known that continuum shell elements such as SC6R and SC8R (6 and 8-node in-plane general-purpose continuum shell with reduced integration, respectively) are more accurate in contact modeling than conventional shells, since they employ two-sided contact taking into account changes in thickness no matter how thick the elements are compared to other element dimensions. However, although continuum shells provide robust and accurate solutions to most shell applications, these elements may show slow convergence for very thin shell applications. In such cases conventional thin shell elements should be used, as we will see later on.

In LS-DYNA different formulations are available for the shell elements. The most frequently used shell element is the so called Belytschko-Lin-Tsay element. It was first implemented in LS-DYNA as a computationally more efficient element than its precursor. The Belytschko-Lin-Tsay element is based on a combined co-rotational and velocity strain formulation. The co-rotational portion of the formulation avoids the complexities of nonlinear mechanics by embedding a coordinate system in the element. The Belytschko-Lin-Tsay element uses a reduced integration scheme, in order to reduce the hourglass modes hourglass control is introduced. The fully integrated shell element with assumed strain interpolants used to alleviate locking and enhance in-plane bending behavior. It uses a local element coordinate system that rotates with the material to account for rigid body motion and automatically satisfies frame invariance of the constitutive relations. The local element coordinate system is similar to the one used for the Belytschko-Tsay element, where the the first two basis vectors are tangent to the shell midsur-

face at the center of the element, and the third basis vector is in the normal direction of this surface and initially coincident with the fiber vectors [3].

#### 5.4.2 Solid element formulations

Solid (continuum) elements are the standard volume elements of ABAQUS. With these nearly all volumetric structures can be modeled and calculated. The number of elements and therefore the number of nodes is much larger than in comparable 2D models. Solid structures usually lead to large meshes when modeled with solid elements and therefore need large computational time and memory. In regions of large stress gradients the mesh density must be large. Therefore one should use shell or beam elements whenever possible. Solid elements are provided with first-order (linear C3D8) and second-order (quadratic C3D20) interpolation. Metal forming applications involve bending with large deformations, the strain variation through the thickness must be at least linear, and constant strain (first-order, C3D8) elements do a poor job of representing this variation. Fully integrated first-order solid elements (C3D8) also suffer from “shear locking” in thin sheets. They cannot provide the pure bending solution because they must shear at the numerical integration points to respond with an appropriate kinematic behavior corresponding to the bending. This shearing then locks the element—the response is far too stiff. For the isoparametric elements reduced integration provides a cure for these problems, but at the cost of allowing spurious singular modes (“hourglassing”). The use of second order elements (C3D20) is a more reliable alternative, because the second-order interpolation naturally contains the linear strain field. The cost of high computation time could be compensated by using the reduced integration second-order solid elements (C3D20R). For example, a fully integrated, second-order, 20-node three-dimensional element requires integration at 27 points, while the reduced integration version of the same element only uses 8 points and, therefore, costs less than 30% of the fully integrated version. In contrast, when reduced integration is used in the first-order elements (the 4-node quadrilateral and the 8-node brick), hourglassing can often make the elements unusable unless it is controlled. In ABAQUS the artificial stiffness method and the artificial damping method given in Flanagan and Belytschko (1981) are used to control the hourglass modes in these elements.

In LS-DYNA, 8-node brick element is available with full and reduced integration. To reduce the computation time of simulation mostly reduced integration is preferable over the full integration solid element. As already mentioned that fully integrated 8-node solid element also suffer from “shear locking”. To preclude locking, reduced integration is a solution but at the cost of allowing spurious singular modes (“hourglassing”). Unlike ABAQUS, LS-DYNA provides different hourglass control methods to reduce the hourglass modes. Type 6 hourglass control invokes an assumed-strain co-rotational formulation for type 1 solid (8-node) elements and under-integrated 2D solids.

## 5.5 Contact and friction modeling

Modeling of contact between at least two bodies is an essential feature of many metal forming simulations. Appropriate modeling of the contact conditions is vital to the success of such simulations. In typical forming applications, the tools like dies deform very little and are modeled

as rigid bodies. In the current work, the attention will be focused on the interface between a deformable body and a rigid body.

### 5.5.1 Contact modeling in ABAQUS

In metal forming processes, contact occurs between a deformable body (blank) and one or more rigid bodies (forming tools). For defining the contact between the blank and forming tool, ABAQUS provides two methods for modeling the contact interactions: Surface based contact simulations and contact elements based simulations. In the former case, a pure “master-slave” relationship is enforced. The surface of the blank is considered as the “slave”, and the surface of the forming tool is considered as the “master”. For the surface based contact simulations, ABAQUS/Standard offers two contact discretization options: a traditional “node-to-surface” discretization and a true “surface-to-surface” discretization. In surface-to-surface discretization, contact conditions are enforced in an average sense over the slave surface, rather than at discrete points. Such as at slave nodes, as in the case of node-to-surface discretization. To enforce contact between the contacting surfaces, for metal forming simulation they are slave (strip) surface and master (tool) surface, there are three contact constraint enforcement methods available in ABAQUS/Standard: i) The direct method attempts to strictly enforce a given pressure-overclosure behavior per constraint, without approximation or use of augmentation iterations. ii) The penalty method is a stiff approximation of hard contact. iii) The augmented Lagrange method uses the same kind of stiff approximation as the penalty method, but also uses augmentation iterations to improve the accuracy of the approximation.

The constraint enforcement method depends in part on our choice of pressure-overclosure relationship. In order to understand the contact algorithm used in this work, consider now first the kinematics of the interacting surfaces. As shown in ABAQUS Theory Manual, let  $A$  be a point on the deforming mesh, with current coordinates  $\mathbf{x}_A$ . Let  $C$  be the rigid body reference node that defines the position of the rigid body with current coordinates  $\mathbf{x}_C$ . Let  $A'$  be the closest point on the surface of the rigid body to  $A$  at which the normal to the surface of the rigid body passes through  $A$ . Define  $\mathbf{r}$  as the vector from  $C$  to  $A'$ . The configuration described by these quantities is shown in Figure 5.2. Here,  $h$  is the distance from  $A'$  to  $A$  along direction  $-\mathbf{n}$ : the “overclosure” of the surfaces. From the definitions introduced above, we have

$$h\mathbf{n} = -\mathbf{x}_a + \mathbf{x}_c + \mathbf{r} \quad (5.10)$$

Then if  $h < -c$ , there is no contact between the surfaces at  $A$ , and no further surface interaction calculations need be done at this point. Here  $c$  is the clearance below which contact occurs. We define a “hard” surface for the case of  $c = 0$ . The standard contact relationship using the “hard” surface is defined as “hard contact”, which is the most frequently used contact in ABAQUS/Standard. The hard contact allows no penetration of the slave nodes into the master surface, thus, leading to “real” contact.

The conventional shell and solid element formulation in ABAQUS works with both “hard” contact and “softened” contact. Generally, when a “softened” contact relationship is used, the contact pressure is a function of the clearance between the surfaces. The pressure-overclosure relationship can be prescribed by using different forms, e.g., an exponential form (Figure 5.3),

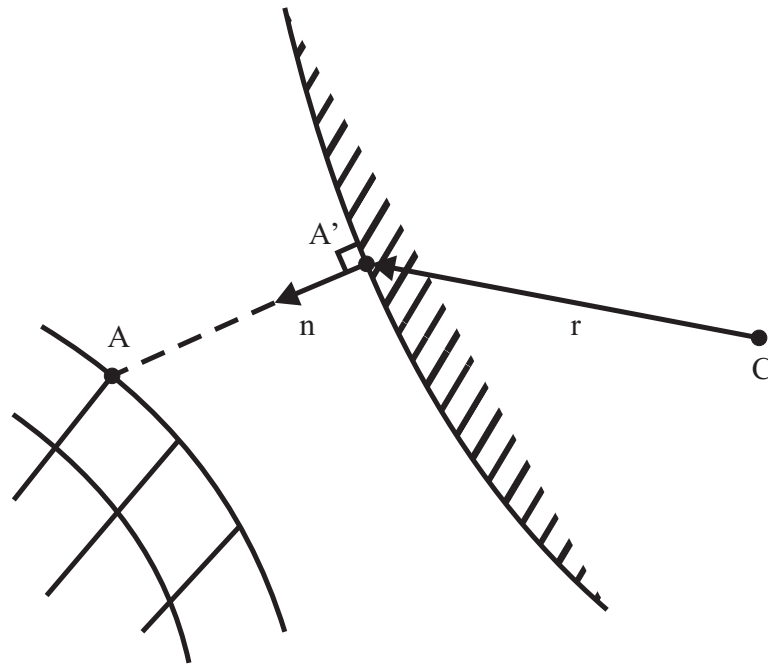


Figure 5.2: Rigid boundary surface geometry (ABAQUS 6.9.1 Theory Manual 5.1.3).

which is used here.

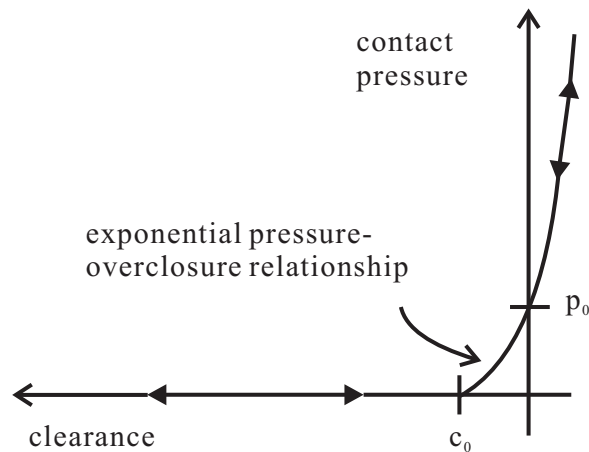


Figure 5.3: "Softened" pressure-overclosure relationship defined with the exponential relation (ABAQUS 6.9.1 Analysis's User's Manual ).

With this (softened) contact pressure-overclosure relationship, the surfaces begin to transmit contact pressure once the clearance between them, as measured in the contact (normal) direction, reduces to  $c_0$ . The contact pressure transmitted between the surfaces then increases exponentially as the clearance continues to diminish.

The friction between the die and the workpiece plays a significant role in metal forming simulations. We distinguish between cohesive and adhesive friction. In cohesive friction the sliding

stresses depend on the yield stress of the workpiece, and the sliding actually occurs in a small boundary layer in the workpiece. This is typical in (but not limited to) bulk forming processes. In adhesive friction, the sliding stresses are proportional to the contact stress. In this case, sliding occurs between the die and the workpiece, which is typical in (but not limited to) sheet forming processes. Adhesive friction is modeled in ABAQUS with a classical Coulomb friction model. The friction coefficient and contact pressure are both important here. In the current investigations, isotropic adhesive friction is assumed. As we will see later, the corresponding (isotropic) friction coefficient has a significant influence on sheet forming and springback.

### 5.5.2 Contact modeling in LS-DYNA

In LS-DYNA, a contact is defined by identifying (via parts, part sets, segment sets, and/or node sets) what locations are to be checked for potential penetration of a “slave” node through a “master” segment. To enable flexibility for the user in modeling contact, LS-DYNA presents a number of contact types and a number of parameters that control various aspects of the contact treatment. In metal forming simulations, since the master side is referred as rigid body, only slave nodes are needed to check for penetration into the master surface. In this situation LS-DYNA offers one-way contact type. The one-way term is used to indicate that only the user-specified slave nodes are checked for penetration of the master segments. A situation where one-way contact may be appropriate for deformable bodies is where a relatively fine mesh (slave) encounters a relatively smooth, coarse mesh (master).

For metal forming simulations, special one-way forming contacts are recommended with the workpiece defined on the slave side:

```
*CONTACT_FORMING_ONE_WAY_SURFACE_TO_SURFACE
```

Orientation is automatic with forming contacts. The treatment of contact between the slave (blank) and master (rigid) surfaces are by default done by using the penalty method. In the penalty-based contact, when a penetration is found a force proportional to the penetration depth is applied to resist, and ultimately eliminate, the penetration. Other methods are also available in LS-DYNA for contact interaction handling, namely, the kinematic constraint method and distributed parameter method. For the penalty method three implementations are available. These are: (i) standard penalty formulation: this is the default method and uses the size of the contact segment and its material properties to determine the contact spring stiffness. As this method depends on the material constants and the size of the segments, it works effectively when the material stiffness parameters between the contacting surfaces are of the same order-of-magnitude. (ii) Soft constrained penalty formulation: this method calculates the stiffness of the linear contact springs based on the nodal masses that come into contact and the global time step size. The resulting contact stiffness is independent of the material constants and is well suited for treating contact between bodies of dissimilar materials. The stiffness is found by taking the nodal mass divided by the square of the time step size with a scale factor to ensure stability. Generally, for the case of metals contacting metals the resulting penalty stiffness for standard penalty formulation or soft constrained penalty formulation is similar. (iii) Segment based penalty formulation: the logic of this method is slave segment-master segment approach instead of traditional slave node-to-master segment approach. This contact has proven very useful for airbag self contact during inflation and complex contact conditions. The Coulomb

friction formulation is used in LS-DYNA to model the friction effects between the interacting bodies.

## 5.6 Convergence behavior and numerical integration

Simulations are carried out for the draw-bending test using the commercial softwares ABAQUS Version 6.9.1 and LS-DYNA version 971 release 4. In order to obtain a converged solution of the boundary value problem and reduce the effects introduced by dynamic explicit calculations, the static implicit method was used for both forming and springback stages of the simulations. Due to the symmetry of the part, only half of the 3D structure was modeled. For simplicity, any effects of the mild initial flow anisotropy and the plastic spin are neglected here. For the purpose of investigation of numerical factors such as element number and integration points, firstly the 3D shell element S4R is used for the simulation. The remaining numerical studies are carried out using 3D solid elements. For simplicity, the bending tool and the roller are modeled as analytical rigid surfaces. The mechanical interaction between the contact surfaces is set to be frictional contact using the isotropic Coulomb model with friction coefficient 0.15. For the numerical investigations to follow, the combined hardening with Voce-type isotropic hardening is generally assumed. The corresponding parameter values used are those for the steel LH 800 as given in Table 5.1.

|               | Value   | Units |
|---------------|---------|-------|
| $\sigma_{Y0}$ | 335.745 | MPa   |
| $s_r$         | 238.62  | MPa   |
| $c_r$         | 8.445   |       |
| $s_x$         | 77.747  | MPa   |
| $c_x$         | 12.155  |       |

Table 5.1: Material model parameter values for LH 800.

### 5.6.1 Convergence behavior

We begin with a convergence study for the finite element discretization used in the context of the forming (bending and drawing together is referred as forming stage) and springback stages of the draw-bending simulations. To this end, we work with the amount of von Mises stress generated at the end of forming stage at the reference point (see Figure 5.4) and the amount of springback predicted. The reference point is chosen in such a way that it is in the most affected region, experiences the bending, the tension force and then drawing under the influence of tension force, and experiences deformation from the beginning to the end of forming stage.

### 5.6.2 Use of shell elements

For ABAQUS, the strip is discretized using the 3D shell element S4R with reduced integration. The results in Figure 5.5 (left) imply that 1790 elements (2.5 mm x 2.5 mm size of each element)

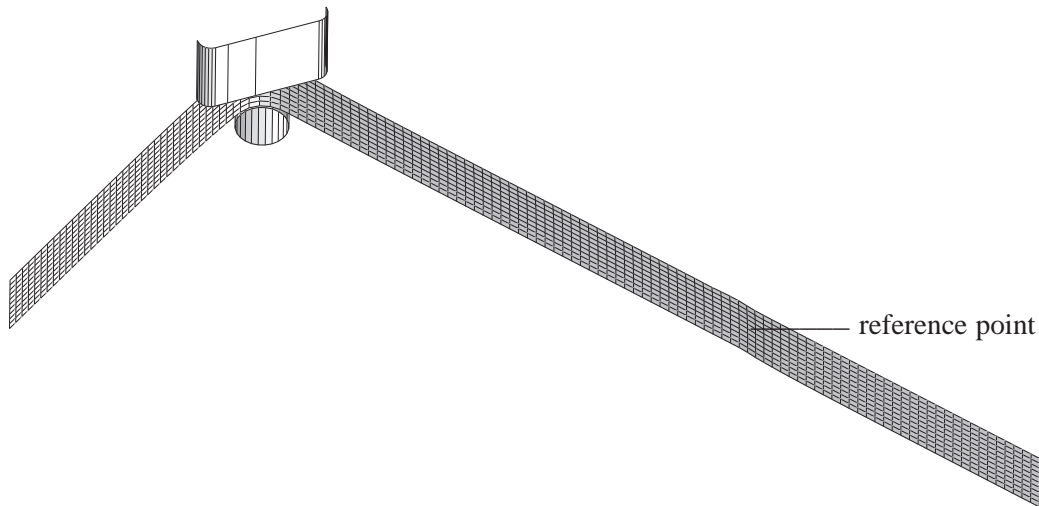


Figure 5.4: 3D FEM model for the draw-bending test and position of Reference Point.

are sufficient for a converged solution as judged by the amount of stress generated. Hence a convergent solution is obtained for this case with 179 such elements along the strip and 10 such elements across the strip. It is also of interest to investigate the effect of convergence in the context of predicted springback. Figure 5.5 (right) shows that the predicted springback is not much effected by the mesh refinement. Even the coarse mesh (700 elements having 4 mm x 4 mm ) gives suitably accurate springback prediction. However fine mesh (1790 elements having 2.5 mm x 2.5 mm ) gives more accurate springback prediction.

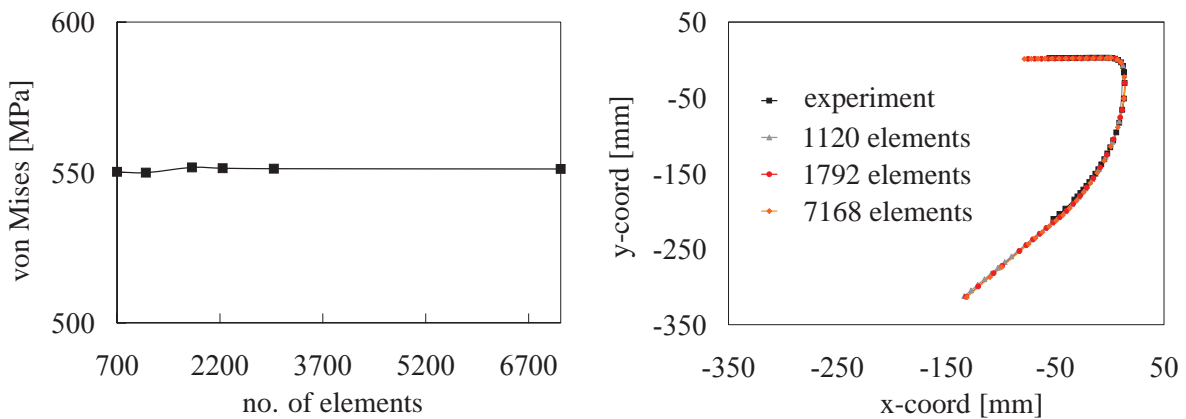


Figure 5.5: Influence of the number of shell elements (S4R) using ABAQUS. Left: On the von Mises stress generated at the end of forming stage. Right: On the springback predicted.

Figure 5.6 (left) shows the von Mises stress at the reference point at the end of forming stage using shell elements with a variable number of elements using LS-DYNA. LS-DYNA gives converged solution for 2240 elements (von Mises stress generated is 551.39 MPa) compared to 1790 elements using ABAQUS (von Mises stress generated is 550.3 MPa) for the same process conditions. As can be seen in Figure 5.6 (right) the accuracy of springback prediction is not



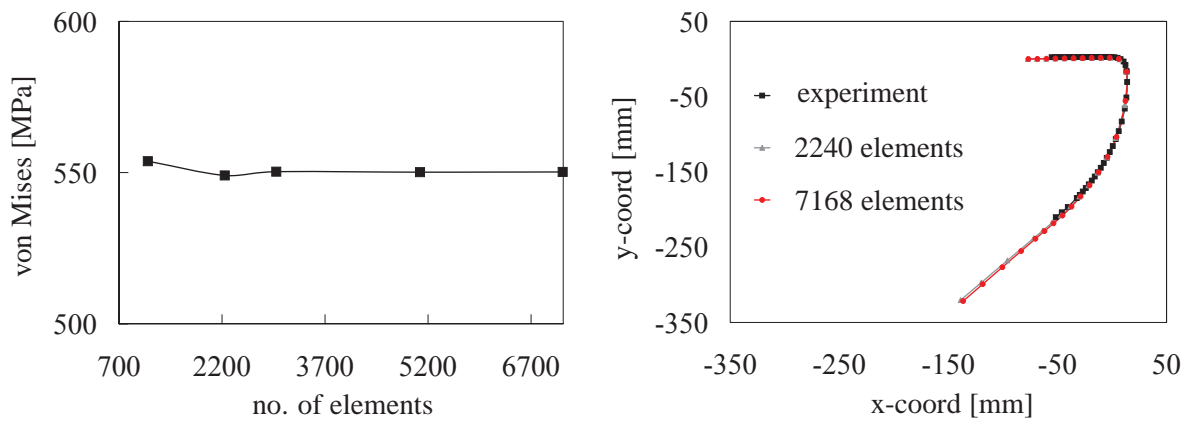


Figure 5.6: Influence of the number of shell elements using LS-DYNA. Left: On the von Mises stress generated at the end of forming stage. Right: On the springback predicted.

much affected by the level of mesh refinement and 2240 elements (2 mm x 2.5 mm ) is enough for the good agreement of springback prediction with the experiment.

### 5.6.3 Number of integration points in the thickness direction

The number of through thickness integration points is an important factor in determining the stress state and the amount of springback predicted in the simulation. The purpose of this section is to examine the influence of the number of through thickness integration points used in simulation on the accuracy of springback prediction and generated stress during the forming stage of the draw-bending simulation. The study is conducted using the Finite element software ABAQUS and LS-DYNA keeping the other parameters such as element size, material model and tension force constant.

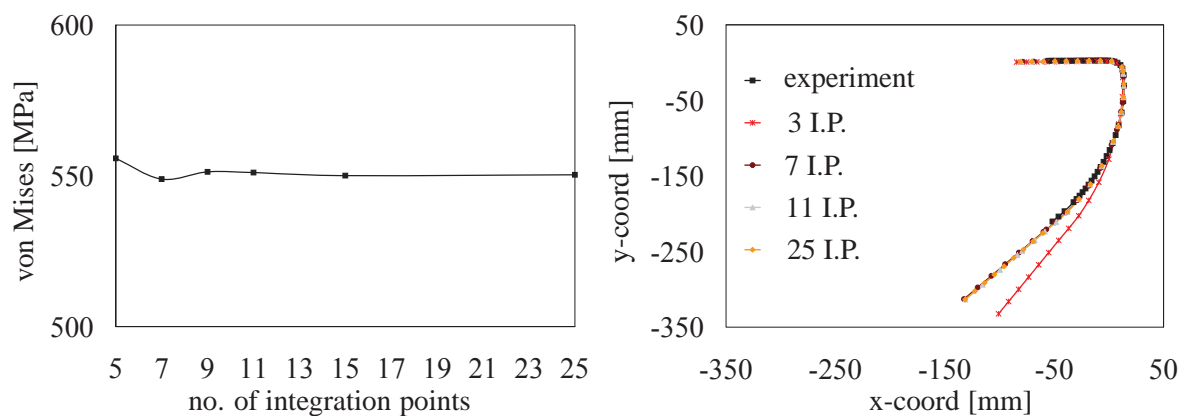


Figure 5.7: Influence of the number of through thickness integration points using ABAQUS. Left: On the von Mises stress generated at the end of forming stage. Right: On the springback predicted.

In the case of ABAQUS, Figure 5.7 (left) shows the von Mises stress at the reference point at the end of the forming stage using shell elements S4R with a variable number of integration

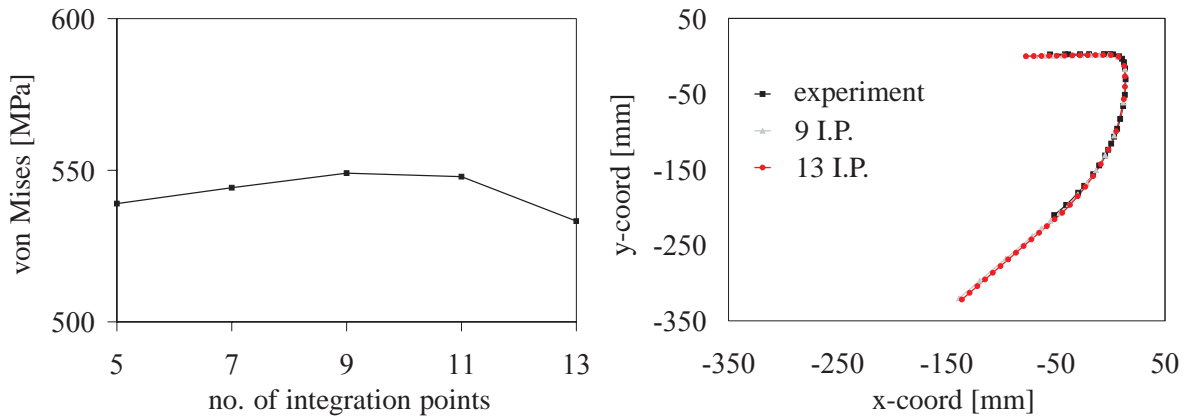


Figure 5.8: Influence of the number of through thickness integration points using LS-DYNA. Left: On the von Mises stress generated at the end of forming stage. Right: On the springback predicted.

points along the shell thickness. This result shown here demonstrated indeed the sensitivity of the von Mises stress to the number of integration points used over the thickness. The converged solution is obtained at 9 integration points and below 9 integration points the results were oscillating. Figure 5.7 (right) demonstrates the influence of integration points used over the predicted springback. It shows that 7 integration point gives the most accurate result. However, for the accuracy, 11 integration points would appear to be necessary for the solution convergence in the context of springback prediction.

Figure 5.8 (left) shows the von Mises stress at the reference point at the end of the forming stage using shell elements with a variable number of integration points along the shell thickness using LS-DYNA. Similar behavior is obtained here for LS-DYNA; 9 integration points are recommended for accuracy (Stander et al. (2007)) because the above 9 integration points trapezoidal scheme is used for numerical integration which requires many more integration points for converged solution as compared to default Gauss integration scheme. Figure 5.8 (right) demonstrates that the springback prediction is in better agreement with the experiment for 9 integration points and less for 13 integration points.

On the basis of results in Figure 5.7 and Figure 5.8, at least 11 integration points would appear to be necessary for ABAQUS and 9 integration points would be necessary for LS-DYNA for solution convergence in the context of springback prediction for the draw-bending test.

#### 5.6.4 Use of solid elements

Another possible source of error of the simulations is the use of shell instead of solid elements. For solid elements simulations we used 2.5 mm x 2.5 mm element size in the plane of the sheet which gave converged solution, and variable number of elements in thickness direction. For the case of ABAQUS, Figure 5.9 (left) shows von Mises stress at the reference point using linear solid element C3D8R with reduced integration. It is clear that convergence is achieved for the linear solid elements in the context of von Mises stress at the end of forming stage. However, it can be seen in Figure 5.9 (right), the error between the predicted and experimentally obtained

springback increases with increasing the number of elements in the thickness direction.

The use of second order elements is the reliable alternative for bending dominant problems. The computational cost is increased to a large extent, but the results are in better agreement with the experiment as can be seen in Figure 5.9 (right). Figure 5.9 (left) shows the comparison of the von Mises stress generated using the linear solid (C3D8R) elements with the von Mises stress generated using the quadratic solid elements (C3D20R) at the end of the forming stage. Figure 5.9 (right) demonstrates the comparison of the predicted springback obtained using the quadratic solid elements and by the linear solid elements. The second order quadratic elements (C3D20R) are more accurate in predicting the springback for the draw-bending test simulations.

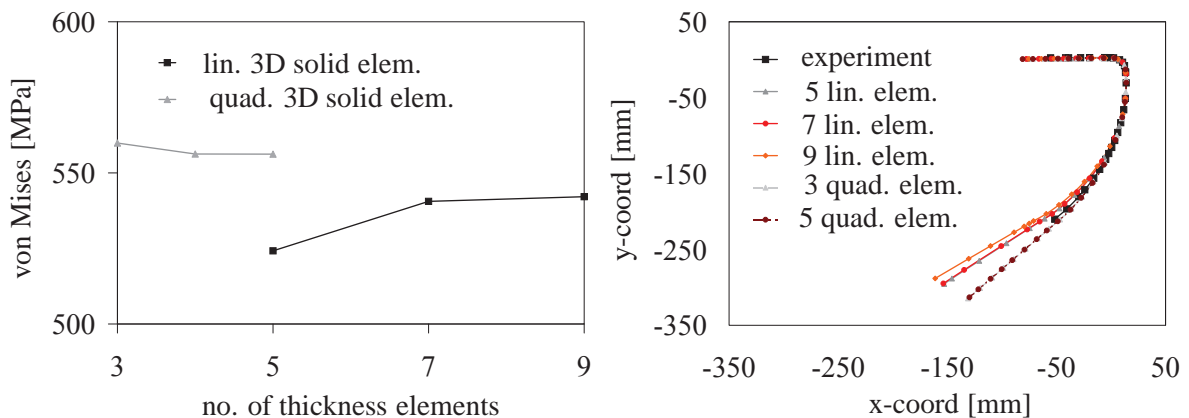


Figure 5.9: Influence of the number of through thickness solid elements using ABAQUS. Left: On the von Mises stress generated at the end of forming stage. Right: On the springback predicted.

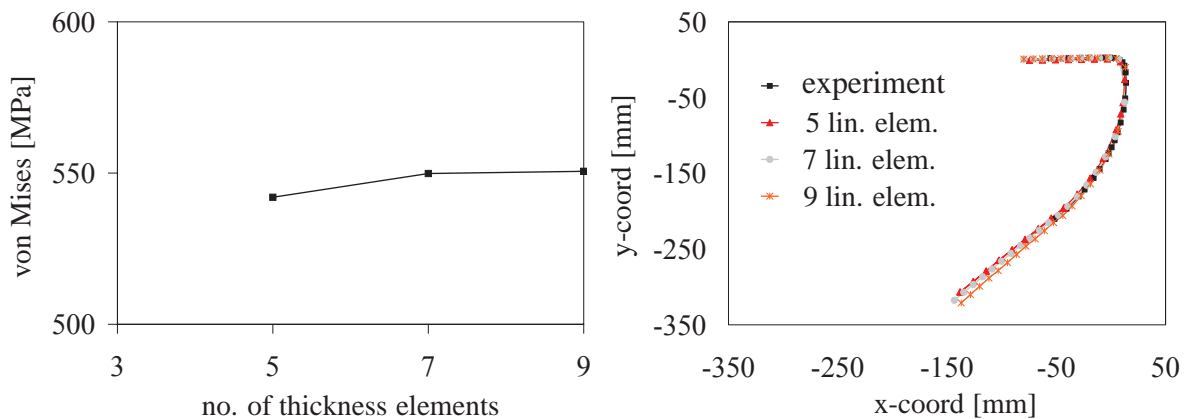


Figure 5.10: Influence of the number of through thickness solid elements using LS-DYNA. Left: On the von Mises stress generated at the end of forming stage. Right: On the springback predicted.

For the case of LS-DYNA, solid elements used in the simulation are 8-node brick elements. By default, solid elements use reduced integration plus viscous hourglass control for faster element formulation. One point integration is advantageous due to savings on computer time

and robustness in cases of large deformations. Figure 5.10 (left) shows the von Mises stress at the end of forming stage for the different number of solid elements in thickness direction. Figure 5.10 (right) shows the comparison of the springback predicted for different number of elements through thickness with the experiment.

On the basis of the results presented in Figure 5.9 and Figure 5.10, it can be concluded that for ABAQUS the quadratic solid elements (C3D20R) with reduced integration predicted springback better than the linear solid elements (C3D8R) in comparison with the experiment. However for LS-DYNA linear solid 8 node elements with reduced integration and viscous hourglass control give good agreement in terms of springback prediction in comparison with the experiment.

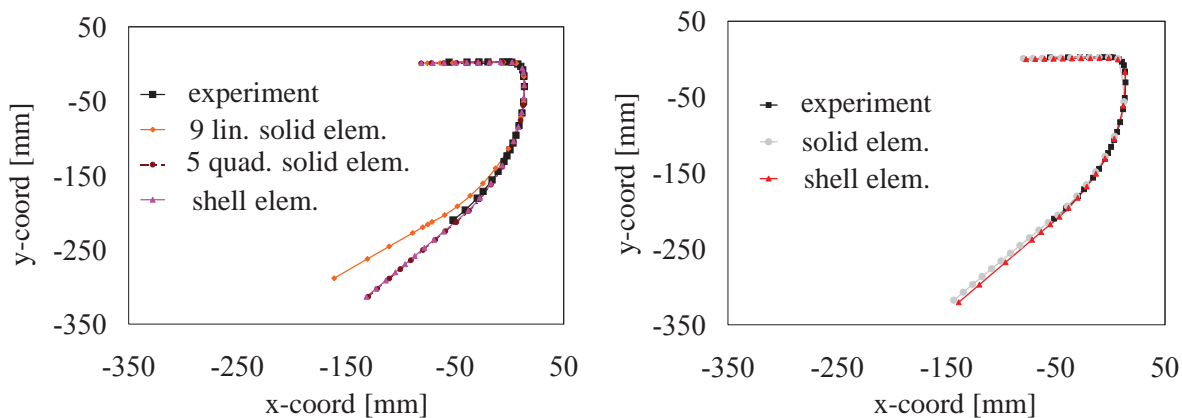


Figure 5.11: Influence of the element formulation over the predicted springback. Left: Using ABAQUS. Right: Using LS-DYNA.

We now compare the influence of element formulation over the predicted springback in comparison with the experiment. Figure 5.11 compares the experimentally measured springback with the simulation results using shell and solid elements for both softwares ABAQUS and LS-DYNA. For ABAQUS, compared to the predicted springback using shell elements and linear solid elements (C3D8R), the predicted springback using the quadratic solid elements (C3D20R) is in better agreement with the experiment (see Figure 5.11 (left)). For LS-DYNA, the 8 node linear solid elements give better agreement with the experiment than the shell elements, as shown in Figure 5.11 (right).

## 5.7 Structural and process conditions

As shown in the previous section, several numerical aspects of the simulation can have a considerable effect on the prediction of springback. Beyond this, of course, the structural and process conditions play a role in the amount of springback obtained. In what follows, we consider in this regard the back force (the tension applied to the strip), frictional effects, and geometric factors such as the tool radius.

### 5.7.1 Effect of Back Force

To study the effect of back force (the tension applied to the strip) applied to the strip over the springback produced, different simulations are carried out using different amount of back force. Figure 5.12 (left) shows von Mises stress at the reference point at the end of the forming stage using shell elements S4R with different amount of back force. These results shown here demonstrate that less von Mises stress for the high back force and this trend continues except in the beginning of the curve at small back force of 2.5 kN before which von Mises stress increases. Due to the higher von Mises stresses for 2.5 kN back force, the springback predicted is higher than the springback predicted for 4 kN back force. Although, from the results in Figure 5.12 (right), it is clear that with increasing amount of back force, and other process and numerical parameters kept unchanged, the springback decreases.

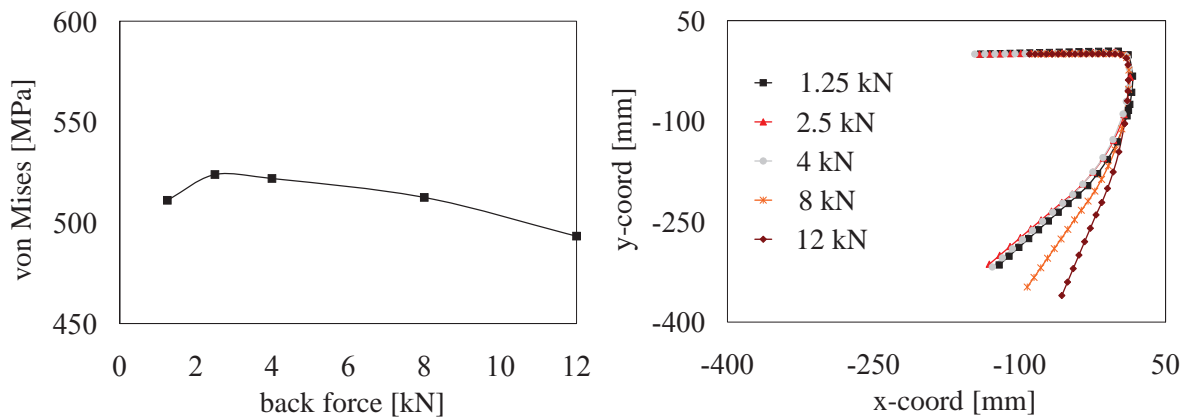


Figure 5.12: Influence of the back force. Left: On the von Mises stress generated at the end of forming stage. Right: On the springback predicted.

### 5.7.2 Effect of Roller Radius

For the draw-bending test, the bending radius has significant impact on the springback keeping the other process and simulation parameters constant. Figure 5.13 (left) shows that with the decreasing roller radius the von Mises stress increases at the end of forming stage. This increase of stress gives rise to more residual stresses hence more springback is produced. This reduction of springback with the increase of roller radius is shown in Figure 5.13 (right).

### 5.7.3 Effect of Friction

The effect of friction between the roller and the strip and between the strip and bending tool is now analyzed. We first started with the case of no-friction between the parts. The coefficient of friction increased gradually from zero to 0.15, 0.2 and 0.4. Figure 5.14 (left) shows the coefficient of friction has no effect on the stress generated during the forming stage. This in turn leads to the same springback prediction for all different friction coefficients. These results are shown in Figure 5.14 (right). Hence, the friction has negligible or no effect over the springback predicted for the draw-bending test. Although, the conclusion departs from the results presented

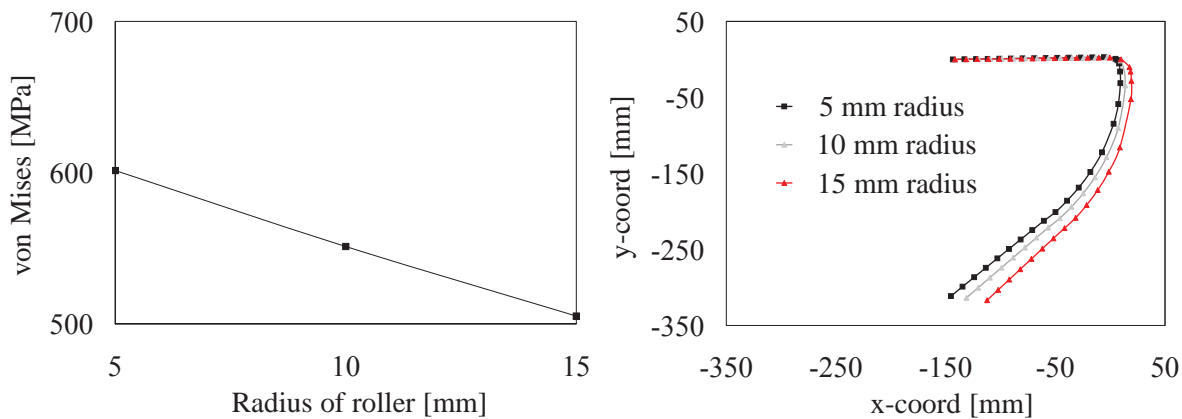


Figure 5.13: Influence of the roller radius. Left: On the von Mises stress generated at the end of forming stage. Right: On the springback predicted.

in literature (e.g. Wang et al. (2005)), most likely due to the fact that in most experiments the sheet tension can not be controlled independently of friction, as in the draw-bending experiment.

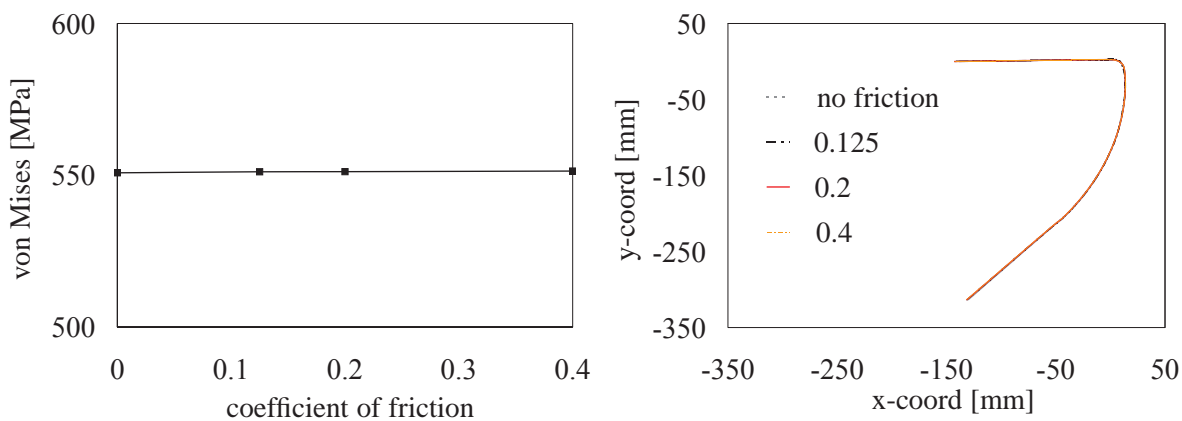


Figure 5.14: Influence of the friction. Left: On the von Mises stress generated at the end of forming stage. Right: On the springback predicted.

#### 5.7.4 Effect of material model

The choice of material model used for the simulation of metal forming and springback stages is perhaps the most important factor that affects the results and springback prediction. The material model describes the initial yield surface and the evolution of the initial yield surface which may change its size, position and even shape due to plastic deformation. A uniform increase of the yield surface can be modeled with isotropic hardening. In this case, the center of the surface is fixed and its shape remains unaltered. A shift of the yield surface with no change in shape and size can be modeled using kinematic hardening. To investigate the effect of material model, we assumed the initial yield surface shows no distinct plastic orthotropy and is thus defined by using an isotropic von Mises yield surface. Investigation for three different types of models ( isotropic hardening model (Voce isotropic hardening law), the kinematic harden-

ing model (Armstrong-Frederick kinematic hardening law) and combined standard isotropic-kinematic hardening model (Voce isotropic hardening law and Armstrong-Frederick kinematic hardening law)) are carried out. The values of the hardening model parameters used are shown in Table 5.2. Figure 5.15 shows the comparison of the results with the experiment. The isotropic hardening model overestimates the springback and kinematic hardening model underestimates the springback. Hence, the standard combined hardening model estimates the springback much better than the isotropic and kinematic hardening model alone.

|               | Value   | Units |               | Value   | Units |               | Value   | Units |
|---------------|---------|-------|---------------|---------|-------|---------------|---------|-------|
| $\sigma_{Y0}$ | 335.745 | MPa   | $\sigma_{Y0}$ | 335.745 | MPa   | $\sigma_{Y0}$ | 335.745 | MPa   |
| $s_r$         | 281.034 | MPa   | $s_x$         | 281.034 | MPa   | $s_r$         | 238.62  | MPa   |
| $c_r$         | 13.069  |       | $c_x$         | 33.1    |       | $c_r$         | 8.445   |       |
|               |         |       |               |         |       | $s_x$         | 77.747  | MPa   |
|               |         |       |               |         |       | $c_x$         | 12.155  |       |

Table 5.2: Identified hardening model parameter values for LH800. Left: isotropic hardening model parameter. Middle: kinematic hardening model parameter. Right: combined isotropic-kinematic hardening model parameters.

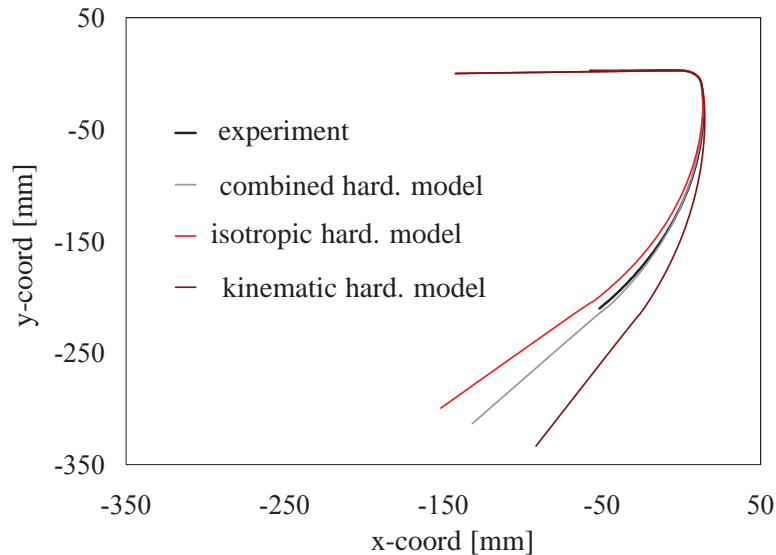


Figure 5.15: Influence of the material model used.

### 5.7.5 Effect of Elastic and Inelastic material model over springback

Two choices of material models were investigated for the springback stage: Firstly, the use of the same material model in the simulation of springback which was used in the simulation of the forming stage. Secondly, the use of elastic material model in the springback followed by the simulation of forming stage in which combined hardening model is used. As can be seen in

Figure 5.16, the inelastic material model used in the simulation of springback stage predicts a better result than the elastic material model.

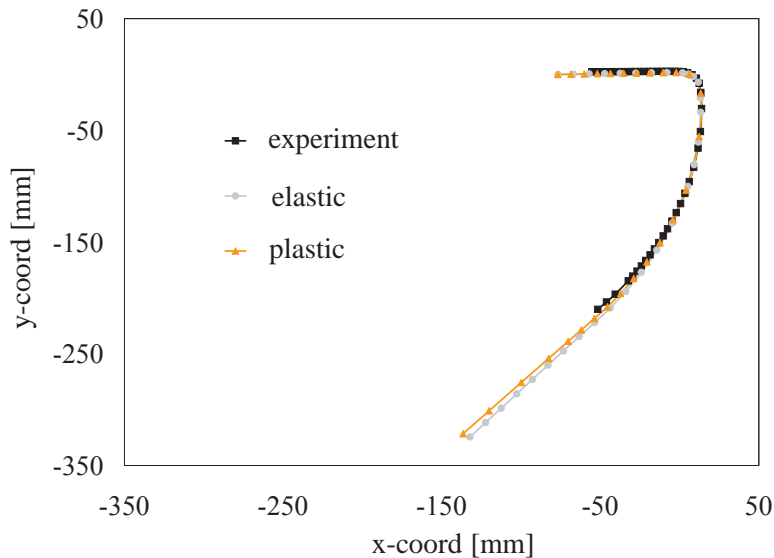


Figure 5.16: Influence of the elastic unloading scheme on the springback prediction results of draw-bending.

## 5.8 Conclusions

In this chapter, a numerical study of the springback effect using the draw-bending test on steel LH 800 was presented. Two FEA codes, ABAQUS and LS-DYNA, were used under similar physical and numerical conditions to simulate the draw-bending test. The test corresponds closely to the drawing of sheet metal over a die radius into a die cavity during a typical metal forming operation. The dependence of simulated springback on both numerical parameters and physical ones has been investigated, and, where data was available, the results have been compared with experiments. For the draw-bending test, the shell element formulation implemented in ABAQUS and LS-DYNA shows the same trend for the mesh convergence analysis during the forming stage, the converged solution is obtained for ABAQUS when the sheet strip is discretized by  $179 \times 10$  elements (2.5 mm x 2.5 mm) along and across the length of the strip. For LS-DYNA  $224 \times 10$  elements (2.0 mm x 2.5 mm each element size) along and across the length of the strip yield the converged solution. The predicted springback is not much affected by the mesh refinement for both softwares.

The current investigation shows that forming results are also sensitive to the number of integration points used in the simulation. LS-DYNA gives accurate results for 9 integration points. However, for ABAQUS, the results converged for 11 integration points for both forming and springback prediction.

For the solid 3D element formulation, ABAQUS shows good convergence for the number of thickness elements when using linear solid elements with reduced integration (C3D8R). However, the predicted springback is not converged and gives more springback for increasing thick-



ness elements. The solution of this problem lies in using quadratic elements with reduced integration (C3D20R). The springback predicted by the quadratic elements with reduced integration (C3D20R) is in better agreement with the experiment than with the linear solid element (C3D8R). For LS-DYNA the linear 8 node brick elements give a more accurate prediction of springback compared to ABAQUS which requires 20 node solid elements. For LS-DYNA, the springback prediction using solid elements is in good agreement with the experiment as compared to the shell elements. However, for ABAQUS the springback prediction by the non linear solid elements are in better agreement with the experiment than the linear solid elements and shell elements.

For the draw-bending test, the increase of the back force (sheet tension) drastically reduces the springback. Friction between the tool and the blank usually affects the springback, as reported by the literature. In the draw-bending test, the friction has little or no effect on the springback. This perhaps could be due to the fact that the sheet tension (back force) can be controlled independently of the friction, and that increasing friction does not change the back force in the draw-bending experiment. A large radius reduces the springback for the draw-bending test keeping the other process conditions as fixed. Most of the inaccuracies in the results can be attributed to the material model used. In particular the inclusion of the Bauschinger effect in the hardening material model significantly alters the result, and good agreement is reached with the experiment as compared to the isotropic hardening model alone, which usually over-predicts the springback. The choice of elastic and elastic-plastic unloading scheme has little effect on the springback. The elastic-plastic springback gives better agreement with the experiment.



# Appendix A

## Experimental characterization and model identification of steel DC06

This appendix presents the experimental data and identification results of the material models presented in Chapter 1 and chapter 2 for the steel DC06.

### A.1 Material Testing

The experiments in this work have been carried out using a biaxial testing device capable of loading a sheet metal specimen in both simple shear and in plane strain tension. The device can carry out the single- or multi-stage loading programs consisting of monotonic (e.g., forward simple-shear), reverse (e.g., forward-reverse simple-shear), and / or orthogonal (e.g., tension-shear) changes of loading direction. For the current work, tests were performed on specimens of the steel DC06. The thickness of the sheet metal specimens used in all the tests was 0.7 mm. For details concerning the experimental setup and procedure, the reader referred to chapter 1 and to Noman et al. (2010).

#### A.1.1 Test results

The tests performed on the specimen of the steel DC06 consist of reverse simple shear test with different amounts of prestrains and orthogonal tension shear. The interstitial free steel DC06 characterized with the pronounced Bauschinger effect, i.e. the early re-yielding after the load reversal, a difference of 50 MPa is observed for the largest amount of preshear. The stagnation of work hardening is found to increase with preshear as can be seen in Figure A.1.

Consider now the orthogonal tension-shear test consists of plane strain tension followed by the simple shear loading. The transition from tension to simple shear is either discontinuous via intermediate unloading (path 1), or two continuous strain path changes differing in the sharpness of the transition from tension to shear loading (path 2 and path 3, respectively). The data so obtained is shown in Figures A.2 to A.4. Figure A.2 shows the experimental strain paths in DC06.

Consistent with existing interpretations of such data in the literature, the presence or absence of cross hardening in such orthogonal tests is judged solely by comparison with the monotonic simple shear results. In particular, any overshoot of the yield stress above the monotonic level upon transition from tension to shear is an indicator of such hardening. Using this “definition,” paths 1 and 2 in Figure A.2 clearly exhibit cross hardening, path 3 with the smoothest transition from tension to shear (as can be seen in Figure A.4) might exhibit a little.

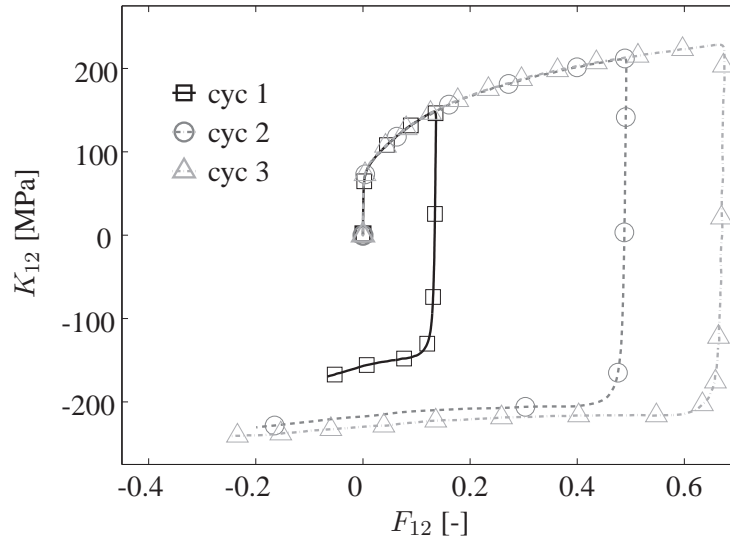


Figure A.1: Reverse simple shear tests for the steel DC06 for different levels of preshear.  $K_{12}$  represents the relevant component of the Kirchhoff stress and  $F_{12}$  represents the relevant component of the deformation gradient.

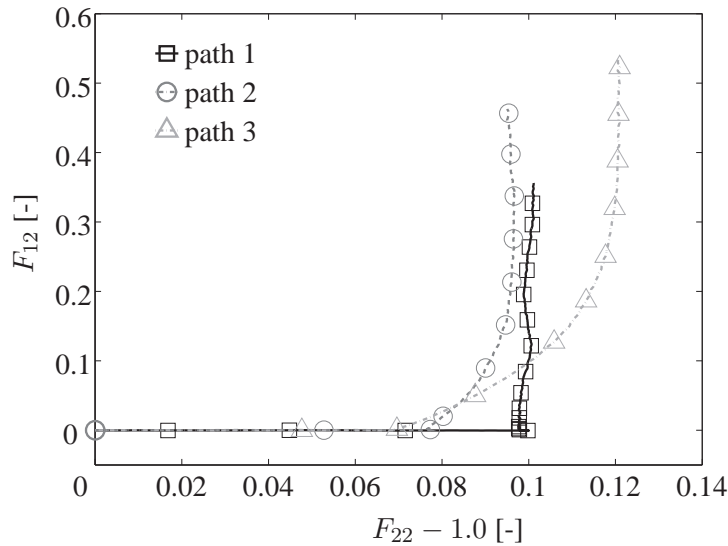


Figure A.2: Experimental strain paths in DC06 resulting from change of loading direction from tension to shear.

## A.2 Parameter Identification

The experimental results presented in the last section show, steel DC06 exhibits pronounced Bauschinger effect, hardening stagnation after load reversal and cross hardening after orthogonal loading path change. The focus is now to identify the material parameters of the material models presented in chapter 1 and chapter 2 using the presented experiments. The material parameter determination is carried out using the program LS-OPT in conjunction with LS-DYNA. Given the homogeneous nature of the tests, one-element calculations suffice. The optimization technique used relies on response surface methodology (RSM) (Stander et al., 2008).

All fits to follow are based on the fixed values of  $\kappa = 151$  GPa and  $\mu = 69.6$  GPa for the

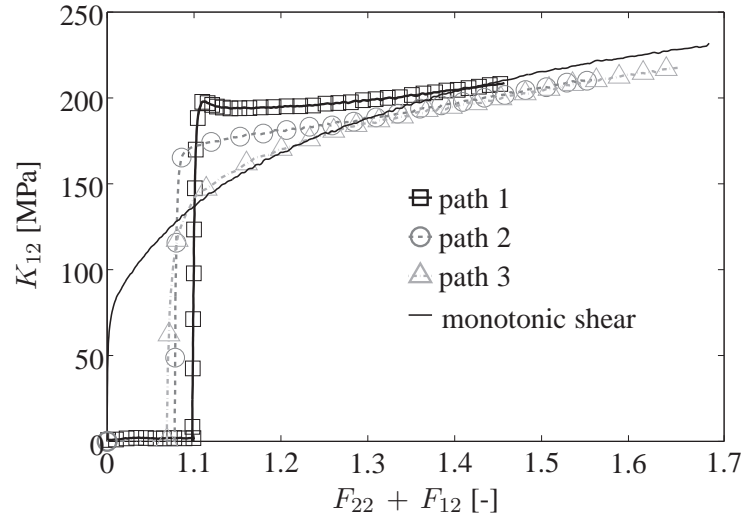


Figure A.3: Shear stress response monotonic forward simple shear and for the three different strain-paths of orthogonal tension-shear test shown in Figure A.2.

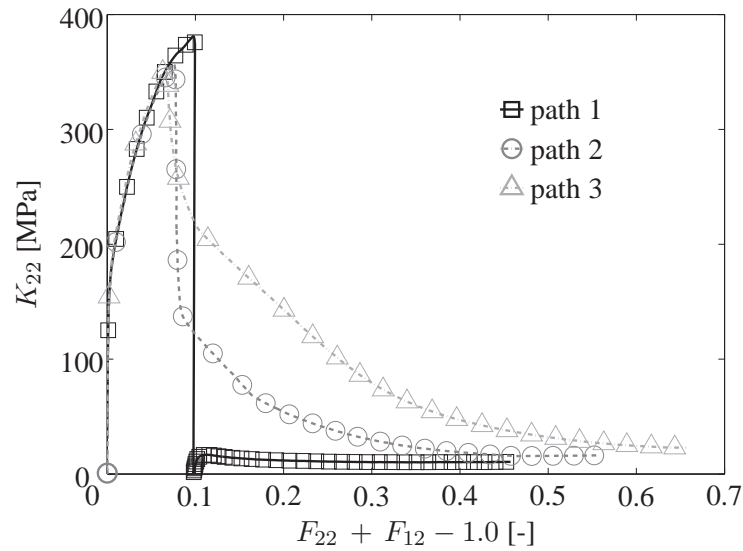


Figure A.4: Discontinuous and continuous orthogonal loading-path changes from tension to shear in DC06.

elastic properties, as well as that  $\sigma_{Y0} = 132.19$  MPa for the initial yield stress, of DC06, all at room temperature. Tensile tests performed on DC06 at  $0^\circ$ ,  $45^\circ$ ,  $90^\circ$  with respect to the rolling direction yielded distinct initial orthotropy and so Hill parameter values of  $F = 0.259$ ,  $G = 0.302$ ,  $H = 0.698$ ,  $L = M = 1.5$ , and  $N = 1.36$ . Strictly speaking, only  $N$ ,  $F$ ,  $G$  and  $H$  can be determined by in-plane tensile tests. Isotropy is also in essence tacitly assumed for the case of through-thickness shear.

### A.2.1 Identification of the yield surface model

The material model presented in the first chapter, accounts besides a shift of the yield surface and its proportional expansion as in the case of conventional combined hardening, also accounts for an evolving yield surface shape and so distortional hardening. As discussed in chapter one,

the model captures the directional hardening by an evolving yield surface. Therefore, it is referred to here as “yield surface model”. In contrast to other models presented in literature, e.g. presented by Teodosiu and Hu (1995, 1998); Wang et al. (2008), the current model does not introduce coupling between the fourth order directional hardening tensor and the evolution of back stress or a coupling of the isotropic hardening with the directional hardening tensor. For a detailed description of the model see chapter 2. The fit procedure for the yield surface model is described in detail in chapter 1. A brief summary will be given here. The fit procedure begins by using monotonic simple-shear test data to identify the Voce isotropic hardening model alone, i.e., assuming no kinematic or cross hardening.

The isotropic hardening parameters so determined are then used as starting values and upper bound to identify the isotropic-kinematic hardening model parameters using both monotonic and cyclic simple-shear test data.

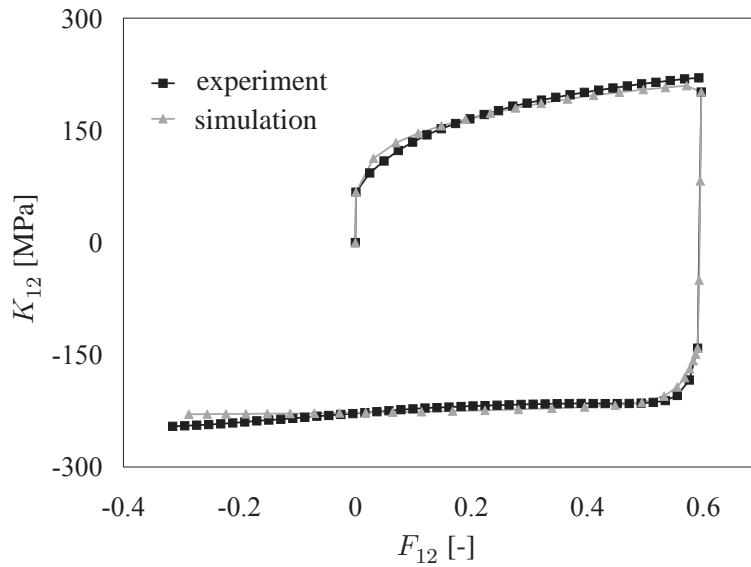


Figure A.5: Comparison of the experimental cyclic simple-shear data with the corresponding identified combined isotropic-kinematic model prediction.

|       | Value  | Units |
|-------|--------|-------|
| $s_r$ | 192    | MPa   |
| $c_r$ | 6.64   |       |
| $s_x$ | 56.0   | MPa   |
| $c_x$ | 33.1   |       |
| $s_d$ | 0.0    |       |
| $c_d$ | 23.9   |       |
| $s_l$ | -0.447 |       |
| $c_l$ | 87.3   |       |

Table A.1: Identified yield surface model parameter values for DC06 for isotropic-kinematic-cross hardening model parameter values determined from monotonic shear, cyclic shear, and orthogonal tension-shear, test data.

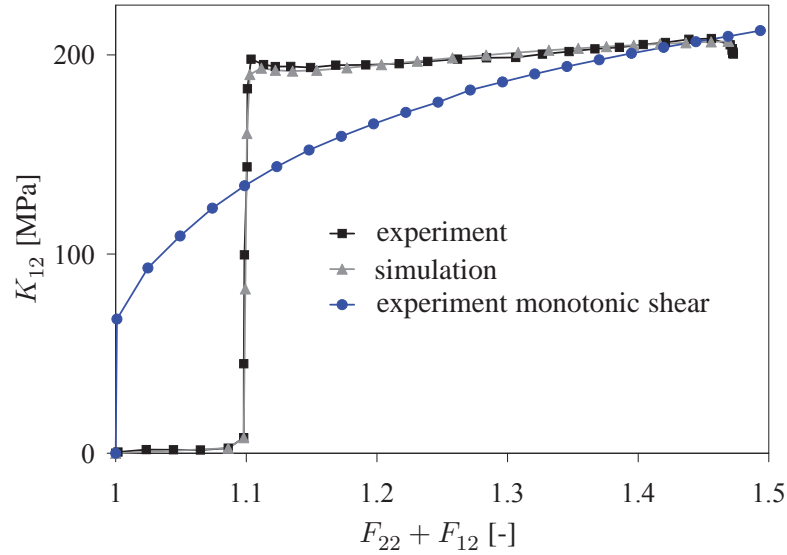


Figure A.6: Comparison of identified isotropic-kinematic-cross hardening model behavior with experimental data for monotonic simple-shear and orthogonal tension-shear test data corresponding to strain path 1 in Figure A.2.

Finally the identification of the isotropic-kinematic-cross (i.e., complete) yield surface model is performed. This is done with the help of the identified parameter values for the isotropic-kinematic case as starting values. In this way, the complete model is fit to monotonic shear, cyclic shear, and orthogonal tension-shear, test data. In particular, the test data of path 1 in Figure A.2 is added to the previous monotonic shear and cyclic shear data sets. As with  $c_r$  and  $c_x$ , the saturation rates  $c_d$  and  $c_l$  associated with cross hardening are constrained to be greater than zero in the fit. On the other hand, as with  $s_r$  and  $s_x$ ,  $s_d$  and  $s_l$  may be positive or negative. Since the values for  $s_d$  determined in this way were on the order of  $10^{-3}$ , this parameter was set to zero in the final fits, resulting in the parameter values for the complete model shown in Table A.1. A comparison of the corresponding experimental data and model fit is shown in Figure A.5 and Figure A.6.

### A.2.2 Identification of the full yield stress model

The yield stress model discussed in the second chapter accounts for cross-hardening, the Bauschinger effect and hardening stagnation. Since the internal variables describing the hardening behavior are coupled in the full yield stress model and there exist 22 material parameters, the identification procedure is tedious and more complicated than for the yield stress model presented in chapter 1. The strategy here is also to identify successively different subsets of the complete set of material parameters with specific test data. In a final global run, all parameters can be varied in order to minimize a global cost function containing experimental data from all considered tests. Haddadi et al. (2006) presented a detailed analysis of the identification procedure using the software SiDoLo for various materials for the Teodosiu model. The great advantage of the identification of this material DC06 is that material parameters for DC06 from a different manufacturer were available e.g. Boers et al. (2010); Haddadi et al. (2006). Differing

from the procedure suggested in Haddadi et al. (2006) no special weight is given to specific regions of the stress-strain curves in order to improve the quality of the fit. Even though the author acknowledges that the effects of the variation in certain parameters are localized, in the current work the only weights introduced to the cost function account for the fact that different tests represent different levels of deformation. Here the constant weight of a single test is dependent of  $F_{\text{Tot}} = \int_0^T |\dot{\mathbf{F}}| dt$ .

| Parameter     | value  | units |
|---------------|--------|-------|
| $\kappa$      | 151000 | MPa   |
| $\mu$         | 69600  | MPa   |
| $\sigma_{Y0}$ | 132.19 | MPa   |
| $x_0$         | 8.1    | MPa   |
| $s_r$         | 20.8   | MPa   |
| $s_s$         | 221    | MPa   |
| $s_l$         | 0.0    | MPa   |

| Parameter | value |
|-----------|-------|
| $c_p$     | 4.0   |
| $c_x$     | 499   |
| $c_d$     | 8.36  |
| $c_l$     | 4.07  |
| $c_r$     | 20.1  |

| Parameter | value |
|-----------|-------|
| $m$       | 1.58  |
| $f$       | 0.2   |
| $n_l$     | 0.0   |
| $n_p$     | 90.0  |

Table A.2: Identified parameters of the full yield stress model for DC06.

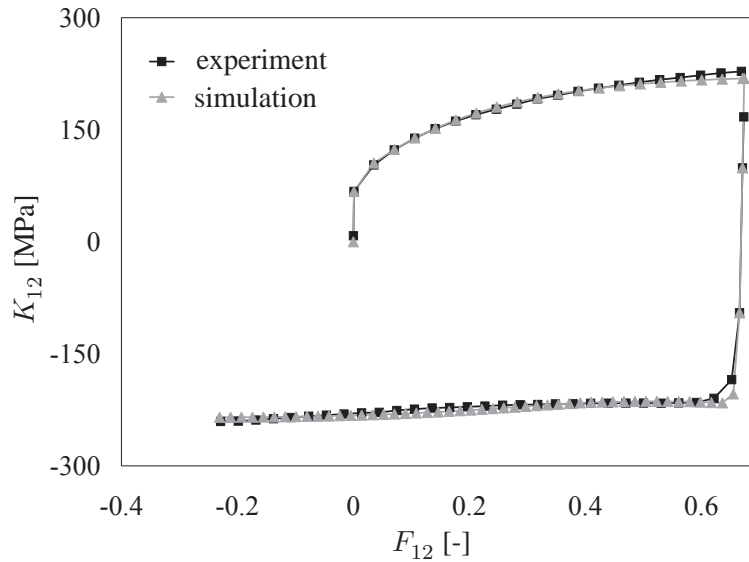


Figure A.7: Comparison of the experimental cyclic simple-shear data with the corresponding identified full yield stress model prediction.

The parameters  $s_r$ ,  $c_r$ ,  $s_s$ ,  $c_d$ ,  $n_p$ ,  $c_p$ ,  $f$ ,  $x_0$  and  $c_x$  are determined from monotonic and cyclic shear tests. Keeping these identified parameters constant, the parameters  $c_l$ ,  $n_l$ ,  $s_l$  and  $m$  are then determined from the tension-shear test data of strain path 1 presented in Figure A.2. In the final run using the monotonic and cyclic shear test and tension-shear test data of strain path 1 presented in Figure A.2 a variation of all parameters is performed. In this way the complete yield stress based model is identified. The parameters for the complete model can be seen in Table A.2. A comparison of the corresponding experimental cyclic shear data and tension-shear data of strain path 1 presented in Figure A.2 with numerical fit is shown in Figure A.7 and Figure A.8.



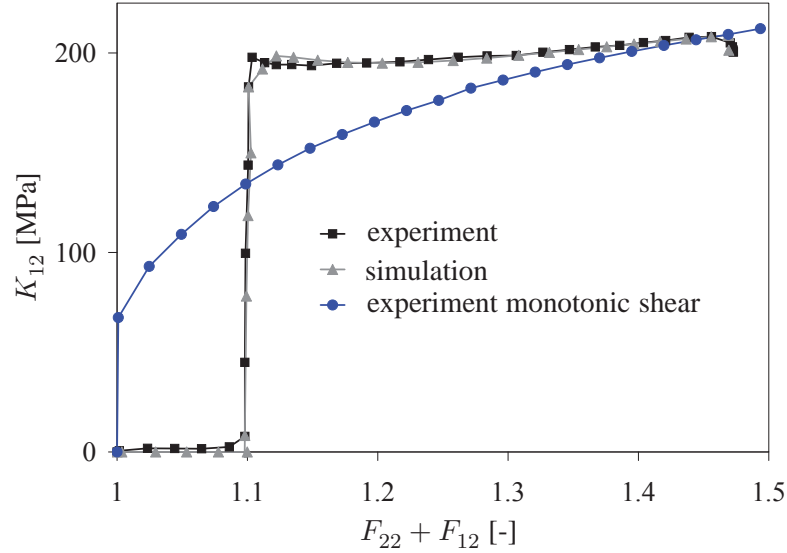


Figure A.8: Comparison of the experimental tension-shear data for strain path 1 in Figure A.2 with the corresponding identified full yield stress model prediction.

### A.2.3 Identification of the simplified yield stress model

The simplified yield stress model discussed in detail chapter 2, decouples the kinematic hardening and directional hardening. This simplification reduces the number of parameters to be determined to 17. Adopting a similar procedure, as presented in the last sub-section, successively different subsets of the complete set of material parameters are identified with specific test data. The parameters  $s_r$ ,  $c_r$ ,  $x_0$  and  $c_x$  are determined from monotonic and cyclic shear tests.

| Parameter     | value   | units |
|---------------|---------|-------|
| $\kappa$      | 151000  | MPa   |
| $\mu$         | 69600   | MPa   |
| $\sigma_{Y0}$ | 132.19  | MPa   |
| $x_0$         | 50.83   | MPa   |
| $s_r$         | 162.085 | MPa   |
| $s_s$         | 277.39  | MPa   |
| $s_l$         | 0.0     | MPa   |

| Parameter | value |
|-----------|-------|
| $c_x$     | 498.9 |
| $c_d$     | 0.185 |
| $c_l$     | 12.13 |
| $c_r$     | 10.07 |

Table A.3: Identified parameters of the simplified yield stress model for DC06.

Keeping these identified parameters constant, the parameters  $c_l$ ,  $s_s$ ,  $s_l$  and  $c_d$  are then determined from the tension-shear test data of strain path 1 presented in Figure 3.3. In the final global run using the monotonic and cyclic shear test as well as the tension-shear test data of strain path 1 presented in Figure A.2 a variation of all parameters is performed. The identified set parameters for the complete simplified yield stress model can be seen in Table A.3. A comparison of numerical fit with the corresponding experimental cyclic shear data and tension-shear data of strain path 1 presented in Figure A.2 is presented in Figure A.9 and Figure A.10.

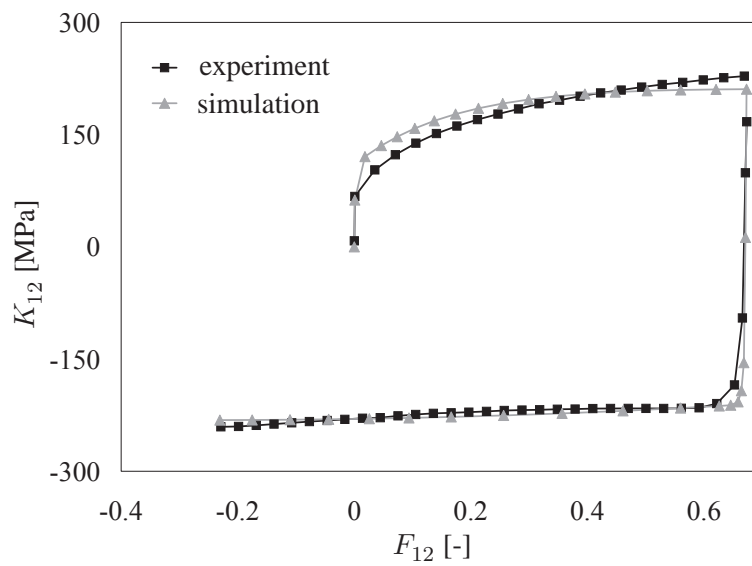


Figure A.9: Comparison of the experimental cyclic simple-shear data with the corresponding identified (simplified) yield stress model prediction.

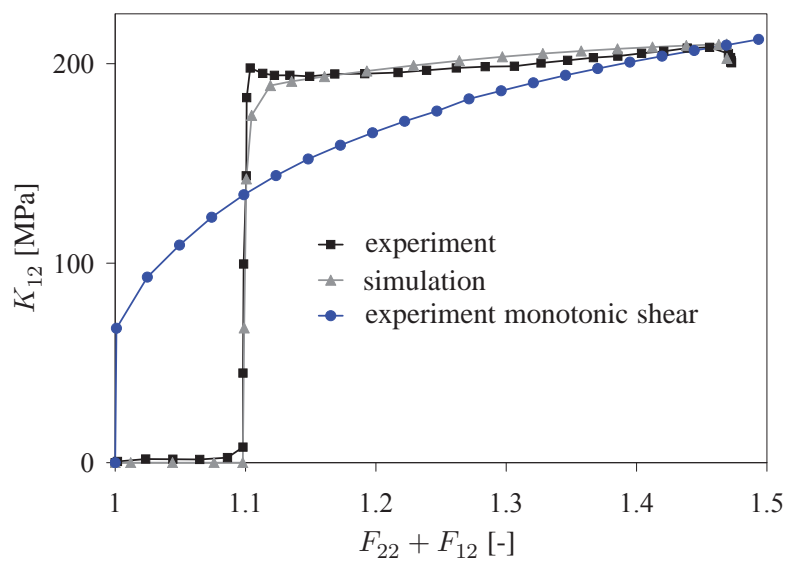


Figure A.10: Comparison of the experimental tension-shear data for strain path 1 in Figure A.2 with the corresponding identified (simplified) yield stress model prediction.

## References

- Aretz, H., A simple isotropic-distortional hardening model and its application in elastic-plastic analysis of localized necking in orthotropic sheet metals, *International Journal of Plasticity*, Volume 24, pp. 1457–1480, 2008.
- Asnafi, N., Springback and fracture in V-die bending of thick stainless steel sheets, *Materials and Design*, Volume 21, pp. 217–236, 2000.
- Baba, A., Tozawa, Y., Effect of tensile force in stretch-forming process on the springback, *Bulletin of JSME*, Volume 7, pp. 834–843, 1964.
- Baltov, A., Sawczuk, A., A rule of anisotropic hardening, *Acta Mechanica*, Volume I, pp. 81 – 92, 1965.
- Barlat, F., Brem, J., Yoon, J., Chung, K., Dick, R., Lege, D., Pourboghrat, F., Choi, S. H., Chu, E., Plane stress yield function for aluminum alloy sheets-part 1: theory, *International Journal of Plasticity*, Volume 19, pp. 1297–1319, 2003.
- Boers, S. H. A., Schreurs, P. J. G., Geers, M. G. D., Levkovitch, V., Wang, J., Svendsen, B., Experimental characterization and model identification of directional hardening effects in metals for complex strain path changes, *International Journal of Solids and Structures*, Volume 47, pp. 1361–1374, 2010.
- Boucher, M., Cordebois, J. P., Incremental evolution of induced anisotropy, *International Journal of Plasticity*, Volume 10, pp. 909–933, 1994.
- Bouvier, S., Alves, J., Oliveira, M., Menezes, L., Modelling of anisotropic work-hardening behaviour of metallic materials subjected to strain-path changes, *Computational Materials Science*, Volume 32, pp. 301–315, 2005.
- Bouvier, S., Gardey, B., Haddadi, H., Teodosiu, C., Characterization of the strain-induced plastic anisotropy of rolled sheets by using sequences of simple shear and uniaxial tensile tests, *Journal of Materials Processing Technology*, Volume 174, pp. 115–126, 2006.
- Bouvier, S., Teodosiu, C., Haddadi, H., Tabacaru, V., Anisotropic work-hardening behaviour of structural steels and aluminium alloys at large strains, *J. Phys. IV France*, Volume 105, pp. 215–222, 2003.
- Brunet, M., Morestin, F., Godereaux, S., Nonlinear kinematic hardening identification for anisotropic sheet metals with bending-unbending tests, *Journal of Engineering Materials and Technology*, Volume 123, pp. 378–383, 2001.
- Carbonnière, J., Thuillier, S., Sabourin, F., Brunet, M., Manach, P., Comparison of the work hardening of metallic sheets in bending-unbending and simple shear, *International Journal of Mechanical Sciences*, Volume 51, pp. 122 – 130, 2009.
- Carden, W. D., Geng, L. M., Matlock, D. K., Wagoner, R. H., Measurement of springback, *International Journal of Mechanical Sciences*, Volume 44, pp. 79 – 101, 2002.

- Chan, K. C., Theoretical analysis of springback in bending of integrated circuit leadframes, *International Journal of Materials Processing Technology*, Volume 91, pp. 111–115, 1999.
- Chen, X. M., Shi, M. F., Ren, R., Xia, Z. C., Springback prediction on split-ring test, *Proceedings of NUMISHEET*, 222–227, 2005.
- Dafalias, Y., Schick, D., Tsakmakis, C., A simple model for describing yield surface evolution, *Deformation and Failure in Metallic Materials (Lecture Notes in Applied and Computational Mechanics)*, Springer, Berlin, 2003.
- Davies, R. G., Liu, Y. C., Control of springback in flanging operation, *Journal of Applied Metal Working*, Volume 3, pp. 142–147, 1984.
- Eggertsen, P.-A., Mattiasson, K., On the modelling of the bending-unbending behavior for accurate springback predictions, *International Journal of Mechanical Sciences*, Volume 51, pp. 547 – 563, 2009.
- Eggertsen, P.-A., Mattiasson, K., On constitutive modeling for springback analysis, *International Journal of Mechanical Sciences*, Volume 52, pp. 804 – 818, 2010.
- Feigenbaum, H. P., Dafalias, Y. F., Directional distortional hardening in metal plasticity within thermodynamics, *International Journal of Solids and Structures*, Volume 44, pp. 7526–7542, 2007.
- Feigenbaum, H. P., Dafalias, Y. F., Simple model for directional distortional hardening in metal plasticity within thermodynamics, *Journal of Engineering Mechanics*, Volume 134, pp. 730–738, 2008.
- Flores, P., Duchêne, L., Bouffieux, C., Lelotte, T., Henrard, C., Pernin, N., Van Bael, A., He, S., Duflou, J., Habraken, A. M., Model identification and FE simulations: Effect of different yield loci and hardening laws in sheet forming, *International Journal of Plasticity*, Volume 23, pp. 420–449, 2007.
- Geng, L., Wagoner, R. H., Role of plastic anisotropy and its evolution on springback, *International Journal of Mechanical Sciences*, Volume 44, pp. 123 – 148, 2002.
- Ghosh, A. K., Backofen, W. A., Strain-hardening and instability in biaxially stretched sheets., *Metallurgical Transactions*, Volume 4, pp. 1113–1123, 1973.
- Haddadi, H., Bouvier, S., Banu, M., Maier, C., Teodosiu, C., Towards an accurate description of the anisotropic behavior of sheet metals under large plastic deformations: modelling, numerical analysis and identification, *International Journal of Plasticity*, Volume 22, pp. 2226–2271, 2006.
- Hill, R., *The Mathematical Theory of Plasticity*, Oxford Classic Texts in the Physical Sciences, Oxford University Press, 1950.
- Hiwatashi, S., Van Bael, A., Van Houtte, P., Teodosiu, C., Modelling of plastic anisotropy based on texture and dislocation structure, *Computational Materials Science*, Volume 9, pp. 274–284, 1997.
- Hiwatashi, S., Van Bael, A., Van Houtte, P., Teodosiu, C., Prediction of forming limit strains un-

- der strain-path changes: application of an anisotropic model based on texture and dislocation structure, *International Journal of Plasticity*, Volume 14, pp. 647–669, 1998.
- Hoc, T., Forest, S., Polycrystal modelling of IF-Ti steel under complex loading path, *International Journal of Plasticity*, Volume 17, pp. 65–85, 2001.
- Huang, Y. M., Leu, D. K., An elastoplastic finite element analysis of sheet metal U-bending process, *Journal of Materials Processing Technology*, Volume 48, pp. 151–157, 1995.
- Ishikawa, H., Subsequent yield surface probed from its current center, *International Journal of Plasticity*, Volume 13, pp. 533–549, 1997.
- Kleiner, M., Schikorra, M., Govindarajan, R., Brosius, A., Springback analysis of sheet metals regarding material hardening, in *Proceedings of the 11<sup>th</sup> International Conference on Sheet Metal*, 712–728, Erlangen, Germany, 2005.
- Laurent, H., Grze, R., Manach, P., Thuillier, S., Influence of constitutive model in springback prediction using the split-ring test, *International Journal of Mechanical Sciences*, Volume 51, pp. 233 – 245, 2009.
- Lee, E. H., Elastic-plastic deformation at finite strains, *Journal of Applied Mechanics*, Volume 36, p. 16, 1969.
- Lee, S. W., Yang, D. Y., An assessment of numerical parameters influencing springback in explicit finite element analysis of sheet metal forming process, *Journal of Materials Processing Technology*, Volume 80, pp. 60–67, 1998.
- Levy, B. S., Empirically derived equations for predicting springback in bending, *Journal of Applied Metalworking*, Volume 3, pp. 135–141, 1984.
- Li, K. P., Carden, W. P., Wagoner, R. H., Simulation of springback, *International Journal of Mechanical Sciences*, Volume 44, pp. 103 – 122, 2002.
- Li, S., Hoferlin, E., Van Bael, A., Van Houtte, P., Teodosiu, C., Finite element modeling of plastic anisotropy induced by texture and strain-path change, *International Journal of Plasticity*, Volume 19, pp. 647–674, 2003.
- Martin, G., Tsang, S., The plastic bending of beams considering die friction effects, *Journal of Engineering for Industry*, 237–250, 1966.
- Meinders, T., Burchitz, I., Bonte, M., Lingbeek, R., Numerical product design: Springback prediction, compensation and optimization, *International Journal of Machine Tools and Manufacture*, Volume 48, pp. 499 – 514, *advances in Sheet Metal Forming Applications*, 2008.
- Nesterova, E. V., Bacroix, B., Teodosiu, C., Experimental observation of microstructure evolution under strain-path changes in low-carbon IF steel, *Material Science and Engineering*, Volume A309-310, pp. 495–499, 2001.
- Noman, M., Clausmeyer, T., Barthel, C., Svendsen, B., Hutink, J., van Riel, M., Experimental characterization and modeling of the hardening behavior of the sheet steel LH800, *Materials Science and Engineering: A*, Volume 527, pp. 2515–2526, 2010.
- Oliveira, M., Alves, J., Chaparro, B., Menezes, L., Study on the influence of work-hardening

- modeling in springback prediction, *International Journal of Plasticity*, Volume 23, pp. 516 – 543, 2007.
- Peeters, B., Bacroix, B., Teodosiu, C., Van Houtte, P., Aernoudt, E., Work-hardening/softening behaviour of b.c.c. polycrystals during changing strain: Part II. TEM observations of dislocation sheets in an IF steel during two-stage strain paths and their representation in terms of dislocation densities, *Acta Materialia*, Volume 49, pp. 1621–1632, 2001a.
- Peeters, B., Kalidindi, S. R., Teodosiu, C., Van Houtte, P., Aernoudt, E., A theoretical investigation of the influence of dislocation sheets on evolution of yield surfaces in single-phase B.C.C. polycrystals, *Journal of the Mechanics and Physics of Solids*, Volume 50, pp. 783–807, 2002.
- Peeters, B., Seefeldt, M., Teodosiu, C., Kalidindi, S. R., Van Houtte, P., Aernoudt, E., Work-hardening/softening behaviour of b.c.c. polycrystals during changing strain paths: I. An integrated model based on substructure and texture evolution, and its prediction of the stress-strain behaviour of an IF steel during two-stage strain paths, *Acta Materialia*, Volume 49, pp. 1607–1619, 2001b.
- Phillips, A., Tang, J. L., Ricciuti, M., Some new observations on yield surfaces, *Acta Mechanica*, Volume 20, pp. 23–39, 1974.
- Queener, C. A., Angelis, R. J. D., Elastic springback and residual stresses in sheet metal formed by bending, *Transactions of ASME*, Volume 61, pp. 757–768, 1968.
- Rauch, E., Plastic anisotropy of sheet metals determined by simple shear tests, *Materials Science and Engineering A*, Volume 241, p. 179183, 1998.
- Rauch, E. F., Schmitt, J. H., Dislocation substructures in mild steel deformed in simple shear, *Material Science and Engineering*, Volume A113, pp. 441–448, 1989.
- Rauch, E. F., Thuillier, S., Rheological behaviour of mild steel under monotonic loading conditions and cross-loading, *Material Science and Engineering: A*, Volume 164, pp. 255–259, 1993.
- Schick, D., *Anisotropic Plasticity and Viscoplasticity*, Ph.D. thesis, TU Darmstadt, 2004.
- Shaffer, B. W., House, J. R. N., the elastic-plastic stress distribution within a wide curved bar subjected to pure bending, *ASME Journal of Applied Mechanics*, Volume 22, pp. 305–310, 1955.
- Simo, J. C., Hughes, T. J. R., *Computational Inelasticity*, Springer Verlag, 1998.
- Stander, N., Roux, W., Goel, T., Eggleston, T., Craig, K., *LS-DYNA Keyword Users Manual*, Livermore Software Technology Corporation (LSTC), 2007.
- Stander, N., Roux, W., Goel, T., Eggleston, T., Craig, K., *LS-OPT Users Manual*, Livermore Software Technology Corporation (LSTC), 2008.
- Svendsen, B., On the modelling of anisotropic elastic and inelastic material behaviour at large deformation, *International Journal of Solids and Structures*, Volume 38, pp. 9579–9599, 2001.

- Svendsen, B., Levkovitch, V., Wang, J., Reusch, F., Reese, S., Application of the concept of evolving structure tensors to the modeling of initial and induced anisotropy at large deformation, *Computers & Structures*, Volume 84, pp. 1077–1085, 2006.
- Tan, Z., Persson, B., Magnusson, C., An empiric model for controlling springback in V-die bending of sheet metals, *Journal of Materials Processing Technology*, Volume 34, pp. 449–455, 1992.
- Tekkaya, A. E., Brosius, A., Cwiekala, T., Bach, F.-W., Grydin, O., Schaper, M., Svendsen, B., Barthel, C., Zeiteffiziente Prozesskettenmodellierung und -berechnung in der Blechumformung und -verarbeitung, in *MEFORM 2008 - Simulation von Umformprozessen*, 262–274, Freiberg, Germany, 2008.
- Teodosiu, C., Hu, Z., Evolution of the intragranular microstructure at moderate and large strains: modelling and computational significance, in Shen, S.F., Dawson, P.R. (Eds.), *Simulation of Materials Processing: Theory, Methods and Applications*, 173–182, Balkema, Rotterdam, 1995.
- Teodosiu, C., Hu, Z., Microstructure in the continuum modelling of plastic anisotropy, in *Proceedings of 19<sup>th</sup> Risø International Symposium on Material's Science: Modelling of Structure and Mechanics of Materials from Microscale to Product*, 149–168, Risø National Laboratory, Roskilde, Denmark, 1998.
- Thuillier, S., Rauch, E. F., Development of microbands in mild steel during cross loading, *Acta Metallurgica et Materialia*, Volume 42, pp. 1973–1983, 1994.
- Ueda, M., Ueno, M., Kobayashi, M., A study of springback in the stretch bending of channels, *Journal of Mechanics and Working Technology*, Volume 5, pp. 163–179, 1981.
- van Riel, M., Strain path dependency in sheet metal - experiments and models., Ph.D. thesis, University of Twente, 2009.
- van Riel, M., van den Boogaard, A. H., Stress-strain responses for continuous orthogonal strain path changes with increasing sharpness, *Scripta Materialia*, Volume 57, pp. 381–384, 2007.
- Voyiadjis, G. Z., Foroozesh, M., Anisotropic Distortional Yield Model, *Journal of Applied Mechanics*, Volume 57, pp. 537–547, 1990.
- Wagoner, R. H., Li, M., Advances in springback, *Proceedings of NUMISHEET*, 209–214, 2005.
- Wang, J., Levkovitch, V., Reusch, F., Svendsen, B., Huétink, J., van Riel, M., On the modeling of hardening in metals during non-proportional loading, *International Journal of Plasticity*, Volume 24, pp. 1039–1070, 2008.
- Wang, J., Levkovitch, V., Svendsen, B., Modeling and simulation of directional hardening in metals during non-proportional loading, *Journal of Materials Processing Technology*, Volume 177, pp. 430–432, 2006.
- Wang, J., Levkovitch, V., Reusch, F., Svendsen, B., On the modeling and simulation of induced anisotropy in polycrystalline metals with application to springback, *Archive of Applied Mechanics*, Volume 74, pp. 890–899, 2005.

- Wang, J. F., Principles of the draw-bend springback test., Ph.D. thesis, The Ohio State University, Columbus, Ohio, USA, 2004.
- Wenner, M. L., On the work hardening and springback in plane strain draw forming, *Journal of Applied Metalworking*, Volume 2, pp. 277–287, 1983.
- Xu, W. L., Ma, C. H., Li, C. H., Feng, W. J., Sensitive factors in springback simulation for sheet metal forming, *Journal of Materials Processing Technology*, Volume 151, pp. 217 – 222, special Volume dedicated to Professor Z.R. Wang on the occasion of his 70th Birthday., 2004.
- Yeganeh, M., Incorporation of yield surface distortion in finite deformation constitutive modeling of rigid-plastic hardening materials based on the Hencky logarithmic strain, *International Journal of Plasticity*, Volume 23, pp. 2029–2057, 2007.
- Yoshida, F., Uemori, T., Fujiwara, K., Elastic-plastic behavior of steel sheets under in-plane cyclic tension-compression at large strain, *International Journal of Plasticity*, Volume 18, pp. 633–659, 2002.
- Yoshida, F., Urabe, M., Toropov, V., Identification of material parameters in constitutive model for sheet metals from cyclic bending tests, *International Journal of Mechanical Sciences*, Volume 40, pp. 237 – 249, 1998.
- Yuen, W., Springback in the stretch-bending of sheet metal with non-uniform deformation, *Journal of Materials Processing Technology*, Volume 22, pp. 1–20, 2000.
- Z. Hu, E. R., Teodosiu, C., Work-hardening behavior of mild steel under stress reversal at large strains, *International Journal of Plasticity*, Volume 8, pp. 839–856, 1992.



# Acknowledgements

The work presented in this thesis was carried out between 2008 and 2011 during my time as a research assistant at the Institute of Mechanics, TU Dortmund. Having come to the end, I would like to express my gratitude to all the people here who gave me tremendous support and help in the last three years.

First of all, I would like to express my heartfelt thanks to my academic advisor Professor Bob Svendsen for his continuous support and seasoned guidance. Without his guidance and work in the fields of material modeling and computational mechanics, this thesis could not have been achieved. Further, I would like to thank Professor A. Erman Tekkaya for his interest in my work and willingness to act as the reviewer of this thesis. Furthermore I thank Jun.-Prof. Björn Kiefer for willingness to act as examiner of this thesis. Also I am very grateful to Professor Andreas Menzel for taking the chairmanship of the examination committee.

Next I would like to express my gratitude to my fellow colleagues at the Institute of Mechanics. Especially, I would like to express my gratitude to Mr. Till Clausmeyer and Dr. Clemens Barthel for their great support, help and the many discussions we had on various scientific issues. Furthermore, I would like to thank Mr. Tobias Kayser and Mr. Matthias Weiss for their support in the area of computational hardware and software facilities. I also appreciate Mr. Maarten van Riel for sharing his knowledge concerning experiments using Twente biaxial tester and results. Special thanks would go to Mrs. Kerstin Walter for her years warm help for my research, business travelling issues. Thanks to Mrs. Christina McDonagh for her excellent language correction of the thesis.

Last but perhaps the most important is to thank my mother for her continuous pray and blessings to get me through tough times of my whole life. I would also like to thank my wife Bushra Urooj Noman for giving me so much moral support during our stay in Germany and also I would like to mention my daughter Hafsah to bring happiness in my life.

Dortmund, February 2011      Muhammad Noman



# Curriculum Vitae

## Personal

Name: Muhammad Noman  
Date of Birth: August 07, 1979  
Place of Birth: Karachi, Pakistan  
Nationality: Pakistani

## Education

2005-2007 Ruhr University Bochum, M.Sc. in computational engineering  
1998-2003 N.E.D. University of engineering and technology Karachi, Pakistan, Bachelor of engineering in mechanical engineering  
1995-1997 Higher secondary school, Board of intermediate education Karachi, Pakistan

## Profession

02/2008-02/2011 Research Assistant, TU Dortmund  
Institute of Mechanics (Prof. Dr. rer. nat. B. Svendsen)